The Henryk Niewodniczański
INSTITUTE OF NUCLEAR PHYSICS
Polish Academy of Sciences

Structure of Bi isotopes close to the ^{208}Pb doubly-magic core

Natalia Cieplicka

PhD thesis written under supervision of
prof. dr hab. Bogdan Fornal

May 26, 2014
Kraków

Contents

Introduction

The atomic nucleus, being a dense system of protons and neutrons, can be considered as a 'laboratory' in which three fundamental interactions strong, electromagnetic and weak, can be studied. Although much experimental data concerning the structure and characteristics of the atomic nucleus have been collected, a theoretical description which would explain all the observed phenomena is still incomplete. This is in part because the nucleon-nucleon interaction has very complex characteristics due to the fact that nucleons are not fundamental particles so they have an intrinsic structure (thus, the description of nuclear forces must take into account that nucleon-nucleon interactions are the result of interactions between the quarks). It is also because the nucleus, as a system of many strongly interacting nucleons obeying the Pauli exclusion principle, demonstrates a very high degree of complexity. Moreover, electromagnetic and weak interactions manifesting in the atomic nucleus are the source of additional complications in its description. As a consequence, progress in theory must go together with experimental investigations, which results in a strong connection between theory and experiment in nuclear physics. New theoretical concepts dictate which experiments would be the most effective in verification of a particular model. On the other hand, measurements can inspire theory to gain better parameter values from its models.

To describe the atomic nucleus as a system of more elementary constituents (nucleons), one needs to know the wave function being the solution of wave equation for such a system. Due to the difficulties mentioned above, one needs to use simplified models instead of the exact description. One of them is the shell model, which explains many experimental observations, such as magic numbers of nucleons: 2, 8, 20, 28, 50, 82, 126, the spin-parity values of the ground states of many nuclei, as well as the structure of excitations of nuclei in the region of magic nuclides. While the shell model with a classic set of orbitals works well near doubly-magic nuclei lying close to the stability valley, in the exotic regions of the nuclear chart; i.e., in the regions remote from stability, the situation is different – the structure of single-particle energy levels changes and new energy gaps may show up while the classical ones may disappear.

One way to trace all these changes, is to undertake systematic investigations of excited structures along a chain of neutron-rich isotopes to the description of which the shell model can be applied. In the present work, we have chosen as the objective of study the series of Bi isotopes near the doubly-closed nucleus ^{208}Pb. We have investigated the ^{205,206,210}Bi nuclei, which have one valence proton and from four neutron holes to one neutron particle with respect to the doubly-magic core ^{208}Pb. Since ^{208}Pb is considered to be one of the best doubly-closed cores due to remarkably wide energy gaps which separate proton shells at Z=82 and neutron shells at N=126, the structure of the ^{205,206,210}Bi nuclei is an excellent testing ground for modern shell-model calculations. In the present work, information about the high-spin yrast structures in the ^{205,206,210}Bi isotopes has been extended. In particular, the aim of the work is the identification of high spin states arising from valence particles/holes excitations and from core excitations in ^{205,206,210}Bi. Also, the spectroscopic data on the low-spin excitations in ^{210}Bi were acquired in a neutron-capture reaction.

The neutron rich nuclei are difficult to reach for spectroscopy studies, because they cannot be produced in fusion-evaporation reactions. The access to excited structures at high spin in those nuclides is possible thanks to a method which relies on using deep-inelastic collisions (DIC) of heavy ions – this method has been developed at IFJ PAN. The main object of interest in the presented thesis are high-spin structures in Bi isotopes. The experiments aimed at investigating those structures were performed at Argonne National Laboratory, where Bi nuclei were populated in deep-inelastic reactions with the use of ^{76}Ge and ^{208}Pb beams on ^{208}Pb target. During such reactions, the nuclei come to a close contact and much kinetic energy is dissipated giving rise to internal excitation energy. In the exit channel one has then two products excited to relatively high energy and spin. Since thick targets were used, the products were stopped inside the target and most of the γ rays that were measured with the use of the Gammasphere multidetector germanium array, appeared in the spectra as sharp lines – they were emitted from nuclei at rest. The second experiment, performed at the Institute Laue-Langevin in Grenoble, was devoted to the low-spin structure of the ^{210}Bi nucleus. In this case ^{210}Bi was produced in cold-neutron capture on ^{209}Bi. The spectroscopic measurements in the non-yrast low-energy region of ^{210}Bi could be performed.

In the first chapter, an introduction to the structure of the atomic nucleus is presented – it includes: the characteristics of nuclear forces and the foundations of the shell model as well as the calculation methods and computer codes used nowadays. The second chapter provides a short description of the region of interest – the region around doubly-magic ^{208}Pb – with emphasis on Bi isotopes. The third chapter presents description of the reactions leading to the nuclei of interest, the experiments which were performed, and the methods of analysis of the coincidence and angular distributions and correlations of γ-ray data. In the fourth chapter, the experimental results are discussed. The fifth chapter is devoted to comparisons of the experimental results with predictions based on shell-model calculations involving the presently available two-body shell-model interactions. The last part contains a summary.

CHAPTER 1

Shell model of atomic nucleus

1.1 Nuclear forces

The nucleons can form a complex system thanks to binding by nuclear forces, arising indirectly from the strong interaction between quarks – the strongest of the four known elementary interactions. The first assumption which one usually makes while describing this force is its two-body character, i.e., one assumes that to the first approximation the force between two given nucleons is independent from the existence of the third one. It is quite obvious that the best source of information about the nuclear forces are the studies of phenomena occurring in the simplest system: two nucleons. One should note however, that analysis of the structure and properties of many-nucleon systems can also provide a wealth of information about some aspects of nuclear interactions.

The experiments performed so far provided much material for deductions. The following empirical facts concerning the nuclear forces have been established:

- the forces binding the nucleons cannot be interpreted with the electromagnetic, weak or gravitational interactions,

- the nuclear interactions on distances ∼fm are attractive and larger than electromagnetic repulsion of protons, but for very small distances of nucleons (< 0.5 fm) they have a strongly repulsive core. This arises from the internal structure of the nucleon and prevents the nucleus from collapsing,

- the nuclear forces are short-range, they act on distances around ∼fm, which can be deduced from the fact of saturation of the strong interaction, i.e. the binding energy is proportional to the number of nucleons (binding energy per nucleon for the nuclei with atomic mass $A > 4$ is around 8 MeV), which means that a particular nucleon interacts with a limited number of other nucleons. If every nucleon interacted with all the others, the binding energy would be proportional to $A(A-1)$,

- the force which acts between two protons is equal to the force between two neutrons and between a proton and a neutron – this indicates the charge independence of the nuclear forces. It results in the equal (approximately) number of protons and neutrons in light nuclei but the majority of neutrons for heavier isotopes – this may be explained by necessity of compensation of rising electrostatic repulsion of protons.
- the nuclear forces depend also on the spin of the system, as well as on the orientation of nucleons spins relative to the vector of their position.

The basis for constructing the theory of nuclear interactions is that the nucleon-nucleon interaction can be described by a potential. To find a form of such potential one must take into account the elementary invariances, i.e.: translational, time reversal, rotational, and under Lorentz transformation. Moreover, the potential must be a scalar. To fulfill these conditions the general form of the potential takes the form:

$$\hat{V} = \hat{V}_C + V_T(r)\hat{S}_{12} + V_{LS}(r)\hat{\sigma}\cdot\hat{l} + V_{LL}(r)(\hat{\sigma}_1\cdot\hat{l})(\hat{\sigma}_2\cdot\hat{l}), \tag{1.1}$$

where: $\hat{V}_C$ is central, $V_T(r)\hat{S}_{12}$ – tensor, $V_{LS}(r)\hat{\sigma}\cdot\hat{l}$ – spin-orbit, and $V_{LL}(r)(\hat{\sigma}_1\cdot\hat{l})(\hat{\sigma}_2\cdot\hat{l})$ – square spin-orbit part. The final parameters are derived in phenomenological approach, i.e., by searching for the proper parametrization, which would reproduce well the known experimental facts. One of the first potential of this type was Hamada-Johnston [2] potential. The other used potentials are Paris [3] and CD-Bonn [4], derived partly from the field theory as well as Argonne AV18 [5], where phenomenological corrections were added to better describe the experimental data. Recently also the extraction of nucleon-nucleon interactions using quantum chromodynamics theory is under way [6, 7].

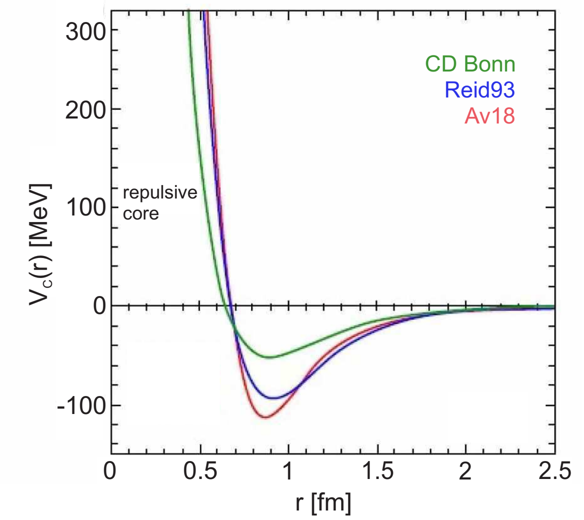

Figure 1.1. The examples of presently used nucleon-nucleon potentials [1].

Even though one can describe the interactions between two free nucleons quite well this does not lead to completely solving the problem of nuclear forces in the nucleus, due to the existence of other nucleons. These other nucleons do not modify the nuclear interactions themselves but they may cause other effects, like setting limits in the phase space because of the Pauli principle. Also, the energy may be dissipated on more than two bodies during the collisions, and, because of the finite size of nucleus, the forces acting on nucleons near the surface are different from the forces acting inside. It is the impossible to directly perform the calculations of interactions between every pair of nucleons for many-nucleon systems – in order to describe such system one must use idealized approximations; i.e., different models.

1.2 Shell model

One of the main discoveries leading to the hypothesis of the shell structure of the nucleus was the observation of magic numbers of nucleons. The nuclei having magic number of protons or neutrons are characterized by, e.g., high separation energy of the nucleon and high energy of the first excited state. These attributes manifest themselves periodically, and, in analogy to the periodic properties of atoms, suggest the shell structure of the nucleus.

The primary assumption of the nuclear shell model is that the movement of nucleons can be to a good approximation treated as the movement of independent particles in a potential that represents the average interaction with the other nucleons. It is so because the Pauli exclusion prevents the inner nucleons from interacting – all the states into which they can scatter are already occupied. Only nucleons close to the surface can interact with each other.

The nuclear shell model is based on the comparison of a nucleus, being a closed system of fermions, to the structure of the atom: nucleons – similarly to the electrons around the nucleus – occupy the specific nuclear orbits. Some orbitals are grouped and such a group is called a shell. The energy spacing between two shells is then called a shell gap. The occurrence of the magic numbers is connected with the existence of those energy gaps between the states or the groups of states.

1.2.1 One-particle model

In the one-particle shell model approach, the quantum mechanical problem of the motion of one nucleon inside the nucleus is similar to the situation with an electron in the hydrogen atom. However, in contrast to the atom's spatially well defined central Coulomb potential, in nucleus the mean field potential is created by all the individual nucleons. The possible values of state energies for a particle moving in a potential are obtained by solving the Schrödinger equation: $H\phi = E\phi$ for this potential, where ϕ is the particle's wave function. The properties of a given nucleus to a large extent are determined by valence nucleons, that is by nucleons located in the single-particle orbitals, starting from the lowest orbital which is allowed by the Pauli exclusion principle.

Some information about the properties of mean nuclear potential can be derived from general considerations. Because a nucleon interacts only with the closest neighbours and the density of matter inside the nucleus is constant, the mean effect should be constant. Consequently, the mean potential near the center of the nucleus should be symmetric, approximately flat and without singularities. From the short-distance character of nuclear force one can deduce that the edge of nucleus must be rather sharp, which implies that the value of the potential should decrease to zero near the nuclear surface. The above mentioned conditions are satisfied to a certain extent by a spherical, square-well potential, which allows to easily calculate the eigenfunctions, but it has to be considered as a rather rough approximation.

Another approximation of the mean nuclear potential is the harmonic oscillator potential given by the equation:

$$V(r) = \begin{cases} -V_0[1-(\frac{r}{R_0})^2], & for\ r < R_0 \\ 0, & for\ r > R_0 \end{cases} \tag{1.2}$$

It has been used very successfully for a long time as the Schrödinger equation with this potential can be solved analytically. Recently, the most popular form of nuclear potential, satisfying the mentioned criteria is the Woods-Saxon potential [8]:

$$V_{WS}(r) = \frac{-V_0}{1+exp(\frac{r-R_0}{a})} \tag{1.3}$$

The parameters in this formula typically have values: $V_0 = (51 + 33(N-Z)/A$ MeV (the potential well depth), $R_0 = 1.27A^{1/3}$ fm (nuclear radius) and $a = 0.67$ fm (the diffuseness of the nuclear surface) [9]. The comparison of the shapes of the three mentioned potentials is displayed in Fig. 1.2.

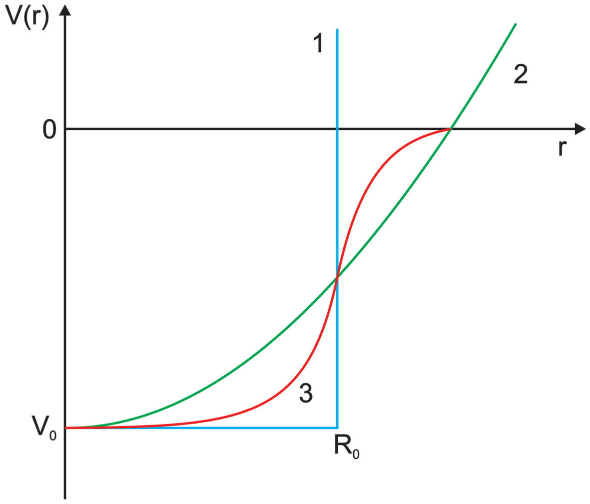

Figure 1.2. The comparison of shapes of different potentials used in the one-particle shell model: 1 - square-well potential, 2 - harmonic oscillator potential, 3 - Woods-Saxon potential.

In the case of protons, the part corresponding to the repulsive Coulomb potential must be included – it is usually done by assuming an isotropic charge distribution inside the nucleus:

$$V_C(r) = \begin{cases} \frac{Ze^2}{r}, & for\ r > R_0 \\ \frac{Ze^2r^2}{R_0^3}, & for\ r < R_0 \end{cases} \tag{1.4}$$

To reproduce the magic numbers with the calculations, the spin-orbit interaction must be taken into account. It was firstly introduced by Marie Göppert-Mayer [10] and independently

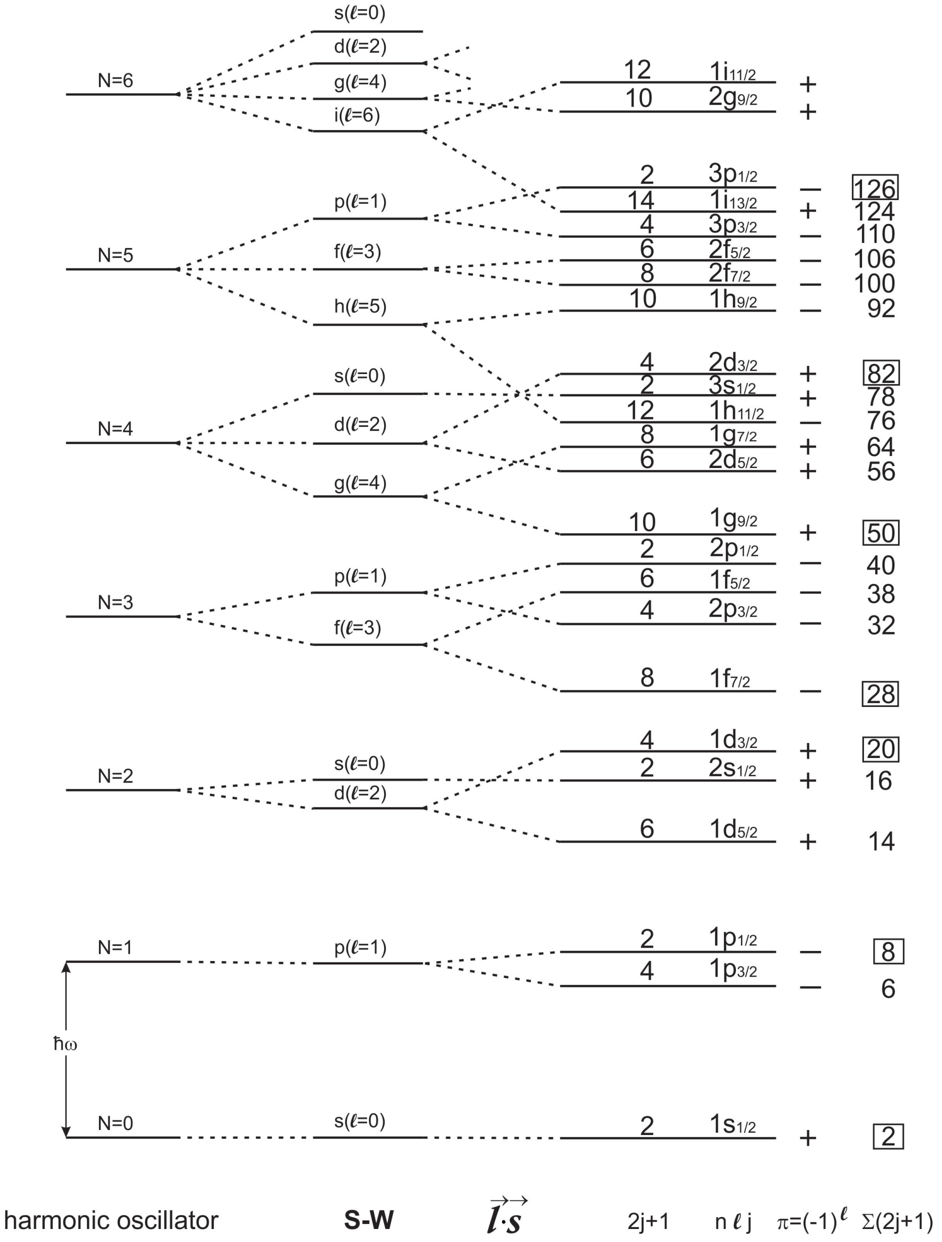

Figure 1.3. Energy levels in many-particle shell model – harmonic oscillator, Woods-Saxon potential without and including spin-orbit interaction.

by Otto Haxel, Hans Jensen, and Hans Suess [11]. This interaction depends on the relative direction of orbital angular momentum $\vec{l}$ and spin $\vec{s}$ vectors. In the case of nuclear forces it appeared to be very important. The part describing this interaction is written as:

$$V_{LS}(r) = -V_{ls}R_0^2\frac{1}{r}\frac{dV(r)}{dr}\hat{l}\cdot\hat{s}, \tag{1.5}$$

where $\hat{l}$, $\hat{s}$ denote the orbital angular momentum and spin operators of a nucleon, respectively, and V_{ls}=0.44 MeV. One can notice that this potential has maximal value near the surface of the nucleus and disappears inside. The existence of the $\hat{l}\cdot\hat{s}$ part in this equation may be explained by consideration of interactions of nucleons spins in the nucleus. The spin-orbit coupling becomes important, when the spins of the considered nucleons are parallel but its sign depends on the relative momentum. Thus, for nucleons having frequent 'meetings' from both sides (inside the nucleus) this interaction, on average, is equal to zero. On the other hand, near the surface, the probability of meeting the nucleon from the outside is lower, so this interaction starts playing important role.

The sum of three mentioned potentials gives the average shell-model potential V_i. The Schrödinger equation for the particle being in this potential is presented below:

$$[-\frac{\hbar^2}{2m}\nabla_i^2 + V_{WS}(r) + V_C(r) + V_{LS}(r)]\phi_\alpha(i) = E_i\phi_\alpha(i). \tag{1.6}$$

One should note, that in the case of Woods-Saxon potential, the analytical solutions are not available, the eigenvalues can be obtained only numerically. In any case, the solutions of equation 1.6, which are usually called single-particle states – SPS's, are characterized by radial quantum numbers n = 1, 2, 3, ... which specifiy the number of the nodes of radial wave function, as well as by orbital quantum number l (0, 1, 2, ...) labeled: $s, p, d, f, g, ...$. The spin-orbit interaction results in splitting of an SPS with given l into two levels with total spin $\vec{j} = \vec{l} + \vec{s}$, where s denotes intrinsic spin. The effect of including the spin-orbit potential is lowering the energy of $j = l + 1/2$ states (spin parallel to the orbital momentum) and raising that of $l - 1/2$ state (spin antiparallel). As the energy splitting due to the spin-orbit coupling is approximately proportional to the l value, it becomes more important for large l.

Every level with given j is degenerated on $(2j + 1)$ magnetic substates; this means that it can be occupied by at most $2j + 1$ nucleons. Because of this degeneracy, the single particle energy (SPE) is referred to j, and, if one discusses an 'orbit', it means j, having $(2j + 1)$ degenerated substates. The neutron and proton shells are filled independently. For the protons the depth of the potential well is smaller because of Coulomb repulsion.

Therefore, the solution of equation 1.6 can be written as:

$$\phi_\alpha(i) = \phi_{nljm}(r_i, \sigma_i)\xi_\nu(\tau_i), \tag{1.7}$$

where the α index denotes the full set of quantum numbers characterizing the orbital $(nljm\nu)$, $\phi_{nljm}(r_i, \sigma_i)$ is a function of space coordinates and spin, and $\xi_\nu(\tau_i)$ is a function of isospin of i-th nucleon with third component ν.

The nucleus is described in this approach by the Hamiltonian H_0 being a sum of Hamiltonians $h_0(i)$ of particular nucleons:

$$H_0 = \sum_{i=1}^{A} h_0(i) = \sum_{i=1}^{A} (-\frac{\hbar^2}{2m}\nabla_i^2 + V_i). \tag{1.8}$$

The solution of this equation, ψ_α, can be written as a product of wave functions of nucleons $\psi_{\alpha_n}(i)$ (where i are coordinates of i-th nucleon), antisymmetrized with respect to the exchange of any two nucleons to obey the Pauli principle. The construction of such wave function can be done by using Slater determinant:

$$\psi_\alpha = \frac{1}{\sqrt{A!}} \begin{vmatrix} \phi_{\alpha_1}(1) & \phi_{\alpha_1}(2) & \dots & \phi_{\alpha_1}(A) \\ \phi_{\alpha_2}(1) & \phi_{\alpha_2}(2) & \dots & \phi_{\alpha_2}(A) \\ \vdots & \vdots & & \vdots \\ \phi_{\alpha_A}(1) & \phi_{\alpha_A}(2) & \dots & \phi_{\alpha_A}(A) \end{vmatrix}. \tag{1.9}$$

For constructing the wave function of the nucleus with nucleons spins coupled to a given spin J, one has to additionally expand it in terms of Slater determinants using Clebsch-Gordan coefficients.

Fig. 1.3 shows the arrangement of SPS's in energy calculated with use of the W-S potential and a spin-orbit coupling term. With the simplest approach, one can construct a given nucleus by placing the appropriate number of protons and neutrons on the single particle orbitals. One can see that in nuclei with proton/neutron numbers equal to 2, 8, 20, 28, 50, 82 or 126 a proton/neutron will be particularly strongly bound because of the large energy gap above those numbers.

Besides the explanation of magic numbers, the one-particle shell model explains also other phenomena, like the 0 angular momentum of the ground state in nuclei with doubly-closed shells, where all magnetic quantum numbers are occupied, so the angular momenta of the nucleons can couple only to zero. The spin of the nucleus can be clearly defined also in the cases when one nucleus is above the closed shells. Then, the spin-parity of the nucleus ground state is determined by the spin-parity of the level occupied by this nucleon. Similarly, when there is one nucleus left to the almost closed shell, the spin-parity value is determined by this hole.

In the frame of the one-particle shell model, the predicting of the energy of the level is possible only for the cases where the cause of excitation lies in the promotion of only one nucleon, i.e. for nuclei with single nucleon over the closed shell. In the cases of partially filled shells, the spins of the nucleons may couple to different values, thus the one-particle model does not allow to precisely define the value of spin of the ground state or excited states. In addition, in this simple approach the states with the same quantum numbers (nlj) are degenerate in energy. For the proper description of the nuclei with a few nucleons above the closed shells one needs to modify the one-particle shell model.

1.2.2 Many-particle model

In the many-particle model one assumes that nucleons occupying completely closed shells form the core and the nucleons from partially occupied shells above it may interact with each other. Those shells are called valence shells. Consequently, the complex quantum problem of interactions of A bodies can be approximated only by consideration of a mean field and effective interactions among the pairs of valence nucleons. Due to the presence of other nucleons building the nucleus together with the interacting valence nucleons, the form of the effective interactions is expected to be significantly different from the interaction describing the scattering of two free nucleons. This mechanism is strongly accentuated by substantial influence of the Pauli exclusion principle, which eliminates most of the discrete quantum states possible to construct. While constructing the effective interactions, one needs to take into account the symmetry laws, which must be respected by this interaction. These symmetries are common for both effective and free interactions. Moreover, the free interaction is the starting point for constructing the realistic interactions.

The Hamiltonian H for a quantum system of many bodies moving in the spatially limited potential, assuming two-body interactions only, can be formally written as sum of kinetic (T) and potential (V) energy:

$$H = T + V = \sum_{i=1}^{A} T_i + \sum_{i>j=1}^{A} V_{ij}, \tag{1.10}$$

where T_i is kinetic energy of i-th nucleon and V_{ij} is a potential of the pair: nucleon (i) - nucleon (j). One can introduce the mean one-body nuclear potential V_i acting on i-th nucleon and rearrange the formula:

$$H = \sum_{i=1}^{A} (T_i + V_i) + \sum_{i>j=1}^{A} V_{ij} - \sum_{i=1}^{A} V_i. \tag{1.11}$$

This may be written as:

$$H = H_0 + V_R, \tag{1.12}$$

H_0 part describes the independent movement of A nucleons in the mean potential V_i. The eigenfunctions and energies of i-th nucleon are defined by the potential V_i – the solution of Schrödinger equation with H_0 are the nucleon single-particle energies (SPEs) in a central potential. Some interactions between the pair of the nucleons may not be averaged and thus not included into the mean potential. These interactions are described by the potential V_R and are called residual interactions. They are relatively weak and this assumption underlies the many-particle shell model.

The equation $H\,|\Psi_n\rangle = E\,|\Psi_n\rangle$ may be converted [9] into an eigenvalue problem of the

Hamiltonian matrix $H_{kl} \equiv \langle \psi_k | H | \psi_l \rangle$:

$$\begin{bmatrix} H_{11} & H_{12} & \dots & H_{1\alpha} \\ H_{21} & H_{22} & \dots & H_{2\alpha} \\ \vdots & \vdots & & \vdots \\ H_{\alpha 1} & H_{\alpha 2} & \dots & H_{\alpha\alpha} \end{bmatrix} \begin{bmatrix} C_1^{(n)} \\ C_2^{(n)} \\ \vdots \\ C_\alpha^{(n)} \end{bmatrix} = E_n \begin{bmatrix} C_1^{(n)} \\ C_2^{(n)} \\ \vdots \\ C_\alpha^{(n)} \end{bmatrix} \tag{1.13}$$

The eigenvalues (energies) and eigenstates (wave functions) are obtained by diagonalizing the Hamiltonian matrix. The total wave function of the system of A nucleons is then expressed as the linear combination of the α basis states from the one-particle model

$$|\Psi_n\rangle = \sum_\alpha C_\alpha^{(n)} |\psi_\alpha\rangle , \tag{1.14}$$

where $\sum\limits_\alpha (C_\alpha^{(n)})^2 = 1$. The wavefunction obtained this way contains, in general, many components corresponding to different configurations – this is called configuration mixing. This can be interpreted as a result of scattering of nucleons in the valence shells. While in the single-particle picture a nucleon stays in one orbit, in the many-nucleon approach this is true only within the closed shell, where all orbits are occupied and a nucleon cannot change its state. On the contrary, in the valence shell, the interaction scatters two nucleons into different pairs of orbits. Those scatterings occur until a kind of equilibrium is achieved, therefore all possible configurations in a particular eigenstate are mixed.

In the second quantization formalism the Hamiltonian can be written as [9]:

$$H = \sum_i \epsilon_i n_i + \sum_{i,j,k,l} v_{ij,kl} a_i^+ a_j^+ a_l a_k, \tag{1.15}$$

where $\epsilon_i = \langle j_i | H_0 | j_i \rangle$ is the single-particle energy of the nucleon on orbit i, n_i is the number operator of orbit i, $v_{ij,kl}$ is two-body matrix element of the nucleon-nucleon interaction for all possible combinations of orbitals i, j, k, l in the model space, and a^+ and a are creation and annihilation operators. The two-body matrix elements (abbreviated as TBMEs) are characterizing the nucleon-nucleon effective interaction. Their presence as non-diagonal elements of the Hamiltonian matrix in Eq. 1.13 is responsible for the configuration mixing.

The two nucleons which are in single-particle states $|j_1, m_1\rangle$ and $|j_2, m_2\rangle$ can be coupled to total angular momentum J (and its z-projection M) by using Clebsch-Gordan coefficients:

$$|j_1 j_2 J M\rangle = \sum_{m_1, m_2} \langle j_1 m_1, j_2 m_2 | J M\rangle |j_1, m_1\rangle |j_2, m_2\rangle . \tag{1.16}$$

The same coupling occurs before and after the interaction. The matrix elements between such coupled states are considered. Due to the rotational invariance of the interaction J or M cannot be changed. Moreover, it makes all coupled matrix elements independent of M. Thus, the matrix elements of two-nucleon states are specified only by j_1, j_2, j_3, j_4 and J. If isospin is conserved, then the TBMEs also are specified by their T value (0 or 1), where T is the total isospin:

$$\langle j_1 j_2 JMT \left| V \right| j_3 j_4 JMT \rangle \,. \tag{1.17}$$

One can see from the Eq. 1.15 that to get information about the eigenvalues of energies of the system of A nucleons, the two parameters: single-particle energies (SPEs) and the energies of residual interactions defined by TBMEs must be known. SPEs may be taken from experiment and the method to obtain TBME is described in Sec. 1.3. To calculate the energy E_n of a nuclear state the diagonalization of the Hamiltonian matrix is needed. Here, the limit is posed by the dimension of the matrix, whose diagonalization can be strictly made. In practice, one must use approximate methods. Presently used computers allow to calculate the eigenvalues of the energies of low-lying states for the dimension of the matrices up to 10^9 [12].

One should note that three- and higher-body interactions between valence nucleons are not included. Usually it is assumed that their effects are small enough in the energy scale of interest and/or are somehow renormalized into effective two-body interactions. This is an approximation, but it turns out to be reasonable from the viewpoint of comparison to experimental results.

1.3 Shell-model interactions

Shell-model interactions, i.e., the residual interactions between the pairs of particles (in general: particle-particle, particle-hole or hole-hole), which were not averaged in the mean potential (H_R in Eq. 1.12), are the object of interest and development of the present shell-model studies. One can assume that inside the nucleus those interactions, however qualitatively consistent with the pure nucleon-nucleon interaction, are modified by the surrounding particles, thus are called effective interactions. In order to perform shell-model calculations, which properly describe the behaviour of the nucleons inside the nucleus, one has to determine the form of the effective interaction which is equivalent with calculating TBMEs.

While constructing effective interactions, one must take into account some corrections: physical, including the influence of the nuclear matter and shell structure on the interacting nucleons as well as the corrections due to restrictions of the model. Those restrictions cause that over many years many methods of determining the effective interactions of nucleons have been developed [13, 14].

In practice, two parameters of the shell model may be observed in experiments. Firstly, SPEs can be taken as energies of single particle/hole states in the nuclei lying one particle/hole away from the closed-shell core. Secondly, TBMEs of the residual interaction H_R can be extracted from energies of states in the neighbours of magic nuclei with two valence particle/holes. Only some TBME may be determined experimentally. Thus, one cannot construct a fully empirical interaction of nucleons in nuclear matter.

On the other hand, once the potential between two nucleons is given, one can calculate all TBMEs. However, up to the present time, the methods of construction of an effective potential do not allow to precisely take into account all the approximations. Consequently, for the practical use of shell-model calculations, the two main approaches to get SM ingredients – empirical and realistic – must be combined. Below, a brief description of procedures that are used to obtain empirical or realistic SM interactions is given.

1.3.1 Empirical

In the empirical approach, the assumption is made that all single-particle energies as well as two-body matrix elements are the free parameters of the model and may be determined from experimental data or by use of fitting procedures. SPEs may be calculated from experimental binding energies (BE) differences between ground state in magic nuclei (closed shell nuclei - CS) and states in their neighbours with 1 or 2 valence particle/holes, $CS \pm 1$ or $CS \pm 2$:

$$\epsilon_j = BE(CS \pm 1; j) - BE(CS; g.s.), \tag{1.18}$$

where the index j denotes the single particle (hole) ground or excited state of a neighbour nucleus characterized by full set of quantum numbers. TBMEs can be extracted from the formula:

$$\left\langle j^2 J \left| V \right| j^2 J \right\rangle = BE(CS \pm 2; j^2, J) - BE(CS; g.s.) - 2\epsilon_j, \tag{1.19}$$

where $BE(CS \pm 2; j^2, J)$ is the binding energy of the nucleus having two nucleons (particles or holes in general) above the core coupled to spin J. Only diagonal TBME can be extracted this way, in consequence, the configuration mixing cannot be taken into account. For this reason the least-square fitting method is applied to determine SPEs and TBMEs (including non-diagonal) with use of a rich amount of experimental data on binding and excitation energies of states from the given model space.

The empirical approach is useful for not too large model spaces, when the number of fitted parameters is significantly smaller than the number of experimental levels. Thus, the empirical interactions are used, for example, to describe the structures of nuclei with *sd* shells (^{16}O – ^{40}Ca). The Hamiltonian of this interaction (USD interaction [15]) is defined by 63 TBMEs and 3 SPEs. Also, recently, H. Maier [16] used the spectroscopic data from the reaction $^{208}\mathrm{Pb}(p,n)^{208}\mathrm{Bi}$ to extract the energies of the levels built on the particle-hole states for nuclei in the vicinity of ^{208}Pb. The experimental results were used for an empirical fit of 140 diagonal and non-diagonal TBMEs.

The advantage of empirical interactions is that one does not need to directly define the form of nucleon-nucleon potential. However, the empirical interactions have also drawbacks, of which the main is the strong dependence on the experimental data to which the interaction is fitted. Additionally, the energies of some calculated states may not depend on the sign of non-diagonal matrix elements, which makes the uncertainty of certain fitted parameters quite large.

1.3.2 Realistic

The most fundamental solution of the nuclear many-body problem would be to derive TBMEs and SPEs from the free nucleon-nucleon potential (Sec. 1.1) – the shell-model interactions derived in such a way are termed realistic interactions. The first attempt to develop the procedure to calculate the interaction inside the finite nucleus from free-nucleon interactions was made by Kuo and Brown [17], who used, as a starting point, the nucleon-nucleon potential of Hamada and Johnston [2] and the harmonic oscillator wave functions as the single-particle wave functions.

A first step in this method, is to eliminate the strong repulsive core from the nucleon-nucleon potential – it usually done by applying so called G matrix theory [18] for a given model space. In the next step, using perturbation theory, the contributions of configurations extending beyond the model space are included.

Derived in the above method TBMEs depend on the mass A, thus for every new core nucleus a new calculation is required. Also, reliable SPEs cannot be obtained in this way and must be taken from experiment.

An alternative method to eliminate directly the hard core repulsive (high momentum) contributions to the nucleon-nucleon potential, instead of using G-matrix, was recently developed [19]. It is based on a low momentum nucleon-nucleon potential V_{low-k}, which can be derived from meson exchange potentials. Such potential is smooth, non-singular and allows to calculate renormalized TBMEs without A dependence, which makes it suitable for different nuclear regions.

An example of the realistic interaction often used for the nuclei in the vicinity of doubly-magic ^{208}Pb nucleus is the Kuo-Herling interaction [20]. The valence space is defined as a set of orbitals available for valence nucleons, whose partial occupation is described by residual interactions. For example, in order to describe the structure below the ^{208}Pb nucleus, the valence space should include the neutron orbitals: $3p_{1/2}$, $2f_{5/2}$, $3p_{3/2}$, $1i_{13/2}$, $2f_{7/2}$, $1h_{9/2}$ and proton orbitals $3s_{1/2}$, $2d_{3/2}$, $1h_{11/2}$, $2d_{5/2}$, $1g_{7/2}$. For nuclei above ^{208}Pb the model space comprises the neutron orbitals: $2g_{9/2}$, $1i_{11/2}$, $1j_{15/2}$, $3d_{5/2}$, $4s_{1/2}$, $2g_{7/2}$, $3d_{3/2}$ and proton orbitals: $1h_{9/2}$, $2f_{7/2}$, $1i_{13/2}$, $2f_{5/2}$, $3p_{3/2}$, $3p_{1/2}$. The valence space defined in this way, shown in the Fig. 1.4, is usually referred to as the Kuo-Herling model space. This valence space is sufficient to describe the vast majority of the experimentally accessible states of single-particle nature. However, in order to properly describe, for example, the collective 3^- state in ^{208}Pb one must include the possibility of core excitations, thus, in such a case, the valence space consists of 11 orbitals for holes and 13 orbitals for particles above the ^{208}Pb core. The calculations for valence space including 24 orbitals has become available quite recently [21], but only for a small number of valence particles.

In practice, very often some realistic TBMEs are modified to obtain better agreement with the experimental level structure of investigated nuclei, however, in this procedure a part of fundamental information is lost and the proper description with use of such interactions is usually limited to only the chosen region of nuclear chart. The calculations describing the structure of Bi isotopes presented in this work were performed with use of this method

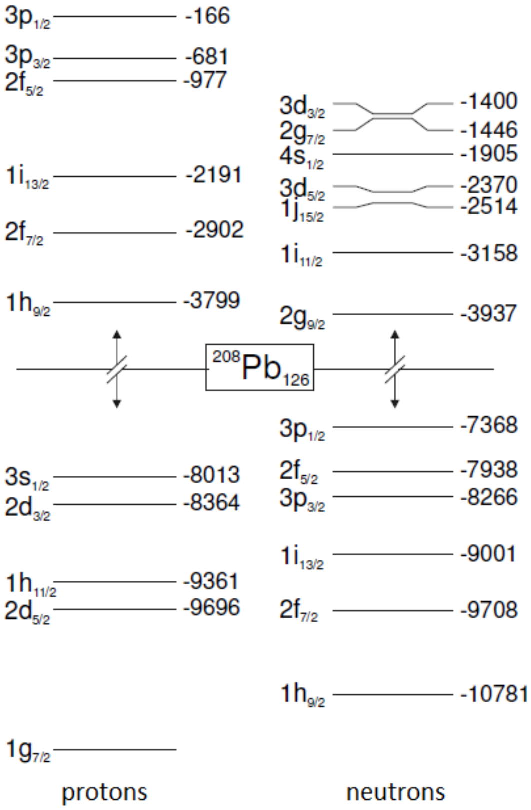

Figure 1.4. Kuo-Herling configuration space.

(however only a very small fraction of all TBMEs has been modified) and the computer code OXBASH [22]. They allowed one proton particle relative to ^{208}Pb in the space of $Z \geq 82$, and one neutron particle in the space of $N \geq 126$ for ^{210}Bi or three/four neutron holes for ^{206}Bi and ^{205}Bi respectively in the $N \leq 126$ space. The single-particle energies were taken from the experimental excitation energies as summarized in Ref. [23]. With respect to the neutron-hole-neutron-hole and proton-particle-neutron-particle interactions, the residual interaction of Kuo and Herling [20] was used as a basis, but with the modifications applied in Ref. [24, 25, 26]. Concerning neutron-hole-neutron-hole interaction, McGrory and Kuo used the ‘bare interaction’ of Ref. [20] for the Pb isotopes plus the ‘bubble’ contribution multiplied by 0.75 [24]. This multiplication factor follows from the fact that at that time it was not possible to calculate all the diagrams up to the second order, therefore it simulates the influence of other terms. In turn, Rydstroem *et al.* [25] additionally adjusted some diagonal matrix elements to reproduce more accurately the experimental energies in ^{206}Pb (as well as in ^{206}Tl and ^{206}Hg) known at that time. The proton-particle-neutron-particle interactions in ^{210}Bi were calculated by Warburton and Brown [26], who used the ‘bare interaction’ of Ref. [20] plus the ‘bubble’ contribution multiplied by 0.9. They also adjusted some TBMEs. In the case of nuclei lying north-west of ^{208}Pb, that is ^{205,206}Bi, a TBMEs between neutron-hole and proton-particle are required. They were not calculated in the cited works. To calculate these TBMEs a H7B [27] potential has been used [16]. It was shown in [28] that this approach seems to be reliable. In addition, the $\langle \nu i^{-1}_{13/2} \nu i^{-1}_{13/2} | H | \nu i^{-1}_{13/2} \nu i^{-1}_{13/2} \rangle$ matrix elements for J^{π} 10^{+}, 12^{+} and $\langle \pi i_{13/2} \nu i^{-1}_{13/2} | H | \pi i_{13/2} \nu i^{-1}_{13/2} \rangle$ for 12^{+}, 13^{+} have been adjusted to fit the experimental levels [29, 30]. One should note that the more detailed description of the modifications of the TBMEs mentioned above may be found in the references included.

1.4 Tools for shell-model calculations

As was mentioned above, shell-model calculations require the diagonalization of large dimensional matrices. The dimension of the matrix can be calculated from the simple relationship [12]:

$$N = \binom{K_n}{n}\binom{K_p}{p} \tag{1.20}$$

where K_n and K_p are the number of considered orbitals (for neutrons and protons, respectively) and n, p are the numbers of valence particles/holes. Additionally, the time required to diagonalize the N-dimensional matrix increases proportionally to N^3 [12]. A very large dimension of the matrix imposes the limits of available configuration space and inquires using the approximate methods of diagonalization.

The first codes were developed in the early 1960's [31] and a number of codes appeared since taking advantage of progress in computer technology. The most commonly used are codes based on the m-scheme, where the states of the basis are Slater determinants of A particles distributed in k orbits and the jj-coupling scheme, in which the basis splits the full m-scheme matrix in boxes whose dimensions are much smaller [32, 33]. The fundamental advantage of the m-scheme representation is the simplicity of the calculation, but here the dimension of the diagonalized matrix becomes extremely large with increasing particle number. On the other hand, in the jj-coupling scheme approach, the complicated angular-momentum-coupling algebra needs to be performed explicitly. The examples of a few standard codes used in present days are listed below:

- OXBASH [22] – developed under the management of B. A. Brown at Michigan State University (USA). It is a set of procedures allowing to calculate the energies of the levels, transition amplitudes and other values useful in the theoretical analysis of nuclear structure. The code uses a hybrid algorithm between the m-scheme and the jj-coupled scheme. It firstly builds the basis states in the m-scheme and then calculates the Hamiltonian matrix in a jj-coupled scheme. This approach allows to avoid angular-momentum-coupling algebra in setting up the jj-coupled basis and the very large matrices of the m-scheme, but the difficult part here is the transition from the m-scheme to the jj-coupled scheme. Presently, it is one of the mostly often used codes. It includes files with SPEs and TBMEs determined for various potentials in different configuration spaces. The code is open for use and well documented.

- NuShell [34] – written by W. D. M. Rae is a jj-scheme code. The different method of calculations solves some problems that OXBASH may have with angular momentum projection from high spin j levels. This makes NuShell faster than OXBASH in some cases, e.g., for particular regions. However, the large number of Hamiltonian matrix elements must be stored in the memory for maximum efficiency, which limits the range of possible calculations. The improved version, NuShellX [35], calculates Hamiltonian 'on the fly' (elements are calculated when are requested, rather than stored on the disc) which significantly decreases the execution time.

- ANTOINE [33] – elaborated by E. Caurier and F. Nowacki is an m-scheme code. It requires the use of large m-scheme vectors although the matrix is not calculated explicitly. The code uses the computers virtual memory which allows to store many precalculated results. The performance of this code is optimal when the proton and neutron subspaces have comparable dimensions.

CHAPTER 2

The region of interest

^{208}Pb is considered as one of the best examples of doubly magic nuclei and the nuclides lying in its vicinity can be described well within the shell model. It is because of remarkably wide energy gaps, which separate proton shells: A_P =($1g_{7/2}$, $2d_{5/2}$, $2d_{3/2}$, $3s_{1/2}$, $1h_{11/2}$) and B_P = ($1h_{9/2}$, $2f_{7/2}$, $2f_{5/2}$, $3p_{3/2}$, $3p_{1/2}$, $1i_{13/2}$) as well as neutron shells: C_N = ($1h_{9/2}$, $2f_{7/2}$, $2f_{5/2}$, $3p_{3/2}$, $3p_{1/2}$, $1i_{13/2}$) and D_N = ($1i_{11/2}$, $2g_{9/2}$, $2g_{7/2}$, $3d_{5/2}$, $3d_{3/2}$, $4s_{1/2}$, $1j_{15/2}$) – this configuration space was shown in the Fig 1.4. A large amount of experimental data concerning nuclei from the region around ^{208}Pb has been collected until now giving possibilities to test various aspects of the shell model. All of the 24 single-particle states in the major shells above and below the closed core of ^{208}Pb are known from experiments so far. Also, many full multiplets corresponding to pairs of nucleons located on the available orbitals have been identified in: ^{206}Pb (two neutron holes), ^{208}Bi (one neutron particle and one neutron hole), ^{210}Bi (proton particle and neutron particle). These multiplets determine diagonal matrix elements of two-body interactions for the configuration spaces A_P-C_N, B_P-C_N and B_P-D_N. Additionally, in many nuclides belonging to the mentioned configuration spaces excited states originating from spin couplings of a few valence particles or holes were located. For example, low-energy structures in ^{205,206,210}Bi isotopes, which are one-proton-particle neutron-holes/particles systems with respect to the doubly magic ^{208}Pb core, are known as arising from couplings in the B_P-C_N and B_P-D_N configuration spaces.

The information regarding the structure of Bi nuclei, which are of interest here, is briefly summarized below.

2.1 ^{205}Bi

The ^{205}Bi nucleus is a one-proton-particle, four-neutron-hole system with respect to the doubly magic ^{208}Pb core. Its ground state has spin-parity J^π=9/2$^-$ and an assigned $\pi h_{9/2}\nu p_{1/2}^{-2} f_{5/2}^{-2}$ configuration. The yrast and near-yrast structures known so far arise from $1p-4h$ couplings involving $1h_{9/2}$ and $1i_{13/2}$ proton particles, and $3p_{1/2}$, $2f_{5/2}$, $3p_{3/2}$, and

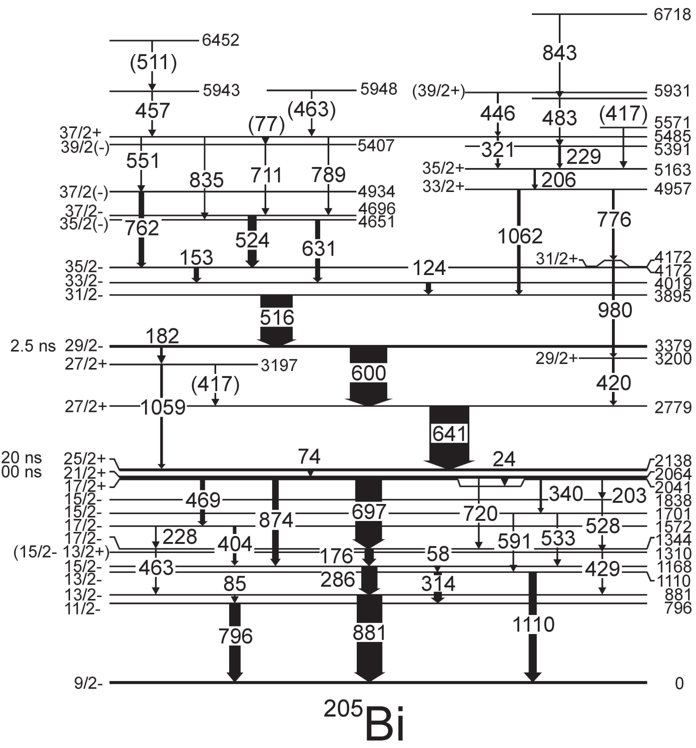

Figure 2.1. Yrast structure of ^{205}Bi nucleus known from previous studies [39].

$1i_{13/2}$ neutron holes, while low-spin structure involves also a proton on $2f_{7/2}$, $2f_{5/2}$, $s_{1/2}$, $d_{3/2}$, $d_{5/2}$, $p_{3/2}$ orbitals. In the ^{205}Bi isotope, three isomeric levels have been identified in earlier studies. One is the $1/2^{+}$ non-yrast state at 1497 keV with $T_{1/2}$=7.9 µs and an assigned $\pi s_{1/2}\nu p_{1/2}^{-2}f_{5/2}^{-2}$ configuration [36]. The other two are yrast levels with J^{π} values of $21/2^{+}$ and $25/2^{+}$ [37, 38]. The lower isomer, lying at 2065 keV, has a half-life of 100 ns and decays by strongly converted 24- and 720-keV γ rays (to which ($E2$) and $M2$ multipolarities were assigned, respectively), whereas the excitation at 2139 keV with $T_{1/2} = 220$ ns decays by a 74-keV transition of $E2$ type. Both isomeric states are of $\pi h_{9/2}\nu p_{1/2}^{-2}f_{5/2}^{-1}i_{13/2}^{-1}$ character. The yrast structure below those isomers was investigated by Lönnroth [37] using the ^{205}Tl(^{3}He$,3n$)^{205}Bi reaction and Byrne *et al.* [39] as well as Hübel *et al.* [38] with a ^{205}Tl$(\alpha,4n)$^{205}Bi process.

The level scheme of the ^{205}Bi nucleus in the upper part was established up to 6719 keV, while the highest assigned spin to a level at 5931 keV is $39/2^{+}$ (from the ^{205}Tl(α,4$n\gamma$) reaction [39]), however, the placement of a number of transitions is uncertain. The presence of a short, 2.5 ns isomer at 3380 keV, deexciting by 182- and 600-keV γ rays of $E1$ character, was also reported [38, 39].

Measurements of angular distributions of γ rays were performed in the cited works and provided the source of information about multipolarities of the transitions, thus helping to assign spin-parity values to the levels. Comparisons with shell-model calculations were also done for the identified states.

The higher-lying yrast structure of ^{205}Bi nucleus, which could not be reached in previous studies, is expected to arise mainly from valence $1p-4h$ couplings, but core excitations are possible as well. Considering the available valence configuration space, it is easy to predict that the highest possible spin value resulting from those couplings should be 53/2 $\hbar$ from the configuration involving proton particle and neutron holes occupying $1i_{13/2}$ orbitals. In general, all valence particle-holes excitations in ^{205}Bi should occur in the energy range up to $\sim$9 MeV.

2.2 ^{206}Bi

The ^{206}Bi nucleus has one proton and three neutron holes ($1p-3h$) with respect to the doubly-closed ^{208}Pb core. Its low-energy yrast and near yrast structure arises primarily from $1p-3h$ couplings involving $1h_{9/2}$, $2f_{7/2}$, and $1i_{13/2}$ proton particles, and $3p_{1/2}$, $2f_{5/2}$, $3p_{3/2}$, $2f_{7/2}$, $1h_{9/2}$, and $1i_{13/2}$ neutron holes. The ^{206}Bi ground state, with spin-parity J^{π}=6^{+}, is of $\pi h_{9/2}\nu f_{5/2}^{-1}$ character, with the isomeric (T$_{1/2}$=7.7 µs) J^{π}=4^{+} member of the $\pi h_{9/2}\nu p_{1/2}^{-1}$ multiplet lying only 60 keV above it and decaying by a 60-keV $E2$ transition [40]. At higher excitation energies, two other isomeric states have been identified in an earlier study with the ^{205}Tl(α,3$n\gamma$) reaction [41]. The 10^{-} state at 1045 keV with T$_{1/2}$=0.89 ms and an assigned $(\pi h_{9/2}\nu i_{13/2}^{-1})\times\nu_{0}^{-2}$ configuration is deexcited by 229- and 904-keV γ rays (to which ($M2$) and $E3$ multipolarities were assigned, respectively). The 15^{+} excitation of $\pi h_{9/2}\nu p_{1/2}^{-1}i_{13/2}^{-2}$ character located at 3147 keV, with a 15.6-ns half-life, decays by a 543-keV transition with assigned $E1$ multipolarity. The highest ^{206}Bi yrast states known thus far; i.e., the 17^{+} and 18^{+} levels at 3604 and 4305 keV, have been located in the ^{205}Tl(α,3$n\gamma$) work as well [41]. In that work, spin-parity assignments were based on γ-ray angular distributions and comparison with the results of shell model calculations.

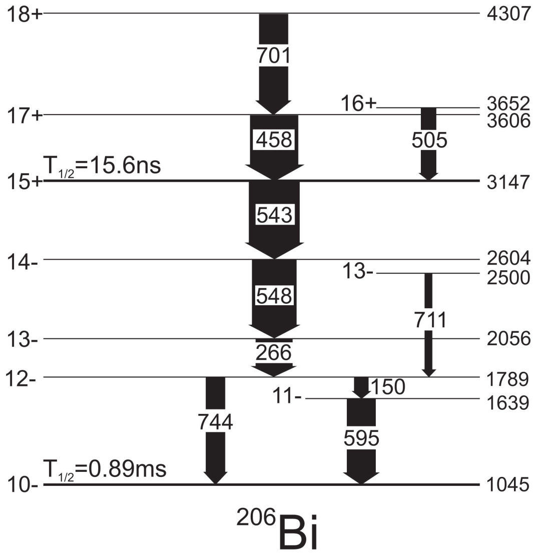

Figure 2.2. Yrast structure of ^{206}Bi nucleus above the 0.89-ms isomer at 1045 keV known from previous studies [41].

States with higher spin, which can be explained as arising from the coupling of a valence proton particle and three neutron holes, are expected to occur in the energy range up to about 7 MeV. The highest spin and parity available as a result of such coupling is 23^+ and originates from a configuration with the proton particle and three neutron holes all occupying the $1i_{13/2}$ orbital. Above 7 MeV, the ^{206}Bi yrast level structure should become more complex as higher lying states have to involve core excitations. These high-lying states in ^{206}Bi could not be reached in previous studies such as those employing the ^{205}Tl(α,3$n\gamma$) reaction of Ref. [41], because only excitations with rather low spin could be populated in α-induced fusion-evaporation process.

2.3 ^{210}Bi

The ^{210}Bi nucleus is a one-proton, one-neutron system with respect to the doubly-magic ^{208}Pb core. Its low-energy structure arises from couplings of a proton on $1h_{9/2}$, $2f_{7/2}$, $1i_{13/2}$, and a neutron on $2g_{9/2}$, $1i_{11/2}$, $1j_{15/2}$ orbitals. Its ground state has spin-parity J^π=1^- and belongs to the fully-identified multiplet of states that originate from $\pi h_{9/2}\nu g_{9/2}$ couplings [42]. The member of this multiplet with maximum spin, J^π=9^-, lies at 271 keV in excitation energy and is the second excited state in this nuclide. Due to the large difference between spins of the first (0^- at 47 keV) and the second (9^-) excited states, the 9^- excitation is a long-lived, α-decaying isomer with $T_{1/2}$=3.04·10^6 y. The presence of two other isomers arising from this multiplet, at 433 (J^π=7^-, $T_{1/2}$ = 57.5 ns) and 439 keV (J^π=5^-, $T_{1/2}$ = 37.7 ns) was also reported [43]. Proton-neutron multiplets $\pi h_{9/2}\nu i_{11/2}$ and $\pi f_{7/2}\nu g_{9/2}$ have been identified in this nucleus as well [44].

The known yrast structure of ^{210}Bi (Fig. 2.3) also includes states arising from core excitations. With use of deep-inelastic reactions ^{48}Ca+^{208}Pb and ^{208}Pb+^{238}U they were traced up to 4595 keV and an angular momentum of approx. 16 $\hbar$ [45], and interpreted in terms of the shell model, although spin-parity assignments to the highest levels are uncertain. The higher lying yrast states must involve promotions of the proton and/or the neutron through the energy gaps, because the highest spin, resulting from the valence particle $\pi i_{13/2}\nu j_{15/2}$ configuration is only 14^-.

On the contrary, the low-spin structure of ^{210}Bi has been investigated in the past with use of different reactions. The excited states were traced up to a level at 4188 keV with the ^{208}Pb$(\alpha, d)^{210}$Bi reaction [46], where besides low-spin also higher-spin excitations (9-13 $\hbar$) were populated. The states above 3 MeV were also investigated by employing processes induced by deuteron beams. For example, the ^{209}Bi$(d, p)^{210}$Bi reaction [47, 48] allowed to reach the 3399-keV level. In turn, the results of γ-ray measurements in the ^{209}Bi$(d, p\gamma)^{210}$Bi reaction [49], were helpful in delineating the low-spin γ-decay scheme of ^{210}Bi up to a 3244-keV level with suggested spin-parity (7^-). Further, the measurements with a thermal neutron capture reaction [50, 51] showed a series of primary γ rays (27 branches of the decay) de-exciting a state at the binding energy of ^{210}Bi, i.e., 4604.63 keV (value from the neutron separation energy [52]). The spin of this state is unsure, but taking into account the spins of the thermal neutrons and the ^{209}Bi ground state, the possible value is 4^- or 5^-. The levels up to 3244-keV (7^-) excitation were populated this way. By employing the thermal

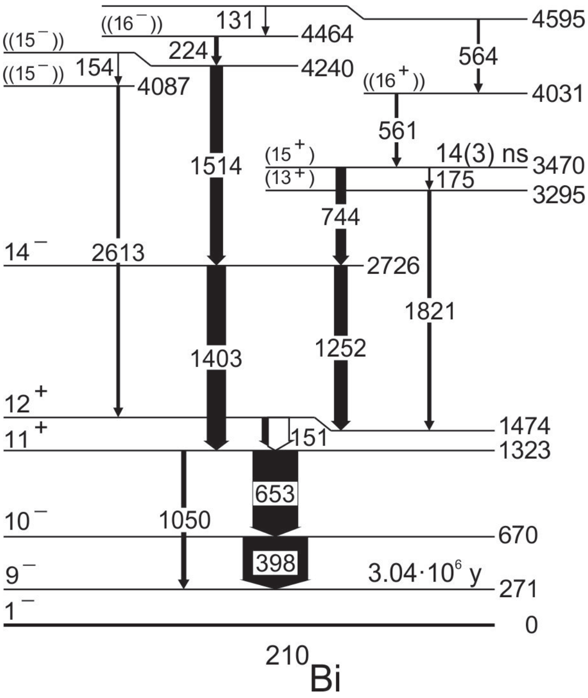

Figure 2.3. Yrast structure of ^{210}Bi nucleus known from previous studies [45].

neutron capture, the investigation of resonant states also may be performed as described in Ref. [53], where the resonances were found in the range of 0.8-23 keV above the neutron binding energy.

CHAPTER 3

Experimental procedures

3.1 Methods to access neutron-rich nuclei

3.1.1 Deep-inelastic reactions

To study the yrast structure of the Bi isotopes of interest, we applied a technique that is based on using deep-inelastic processes (DIC) which occur in heavy-ion collisions. First observations of such processes were reported in the 1960s [54], but the importance of the damped-reaction mechanism was recognized by experimental groups in the early 1970s. The theoretical concepts were developed at that time as well (e.g., [55]). As the excited structures at relatively high spin in nuclei far off the beta stability valley, which are hard to reach by other methods, can be populated in DIC, the usefulness of deep-inelastic reactions for discrete γ-ray spectroscopic studies is unquestionable. This technique relies on using processes which occur at incident energies roughly 20% above the Coulomb barrier where the production of neutron-rich species results from a tendency towards N/Z equilibration of the dinuclear system formed during the collisions.

Taking into account energy of the system and impact parameter b, the nuclear reactions can be characterized in terms of the distance of closest approach r_{min}, which is the distance between the centers of colliding nuclei. Its relation to an interaction radius R_{int} [56], i.e., distance between the centers of nuclei for which nuclear forces start being important, determines the type of reaction. The experimental relation of R_{int} to the radii R_1 and R_2 of the nuclei is given by the approximate formula:

$$R_{int} \approx R_1 + R_2 + 3fm. \tag{3.1}$$

One can distinguish four regions for r_{min}, where the different reactions take place: the Coulomb excitations and elastic scattering for $r > R_{int}$, peripheral collisions for $r \approx R_{int}$, deep inelastic reactions for $r < R_{int}$, and fusion reactions for $r << R_{int}$. The trajectories

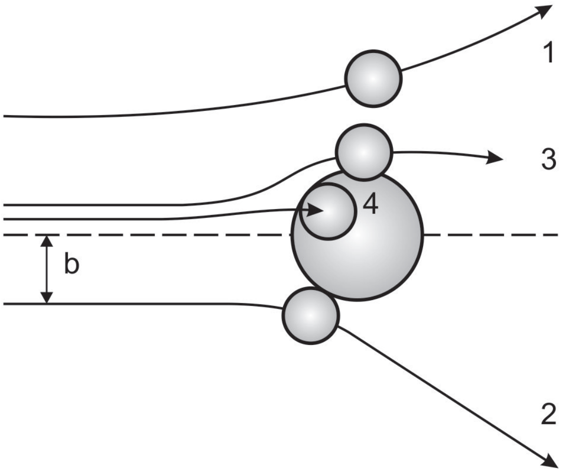

Figure 3.1. Schematic representation of heavy-ion collisions (with energy above the Coulomb barrier) depending on the impact parameter b: 1) elastic scattering, Coulomb excitation , 2) inelastic scattering, transfer reaction, 3) deeply inelastic collision, 4) formation of the compound nucleus.

corresponding to these situations are schematically shown in Fig. 3.1.

For collisions, where the distance of closest approach, r_{min}, is larger than the interaction radius, nuclear interactions do not occur – only elastic scattering and Coulomb excitation are possible. In peripheral collisions ($r = R_{int}$), inelastic scattering and transfer of one or a few nucleons can be observed. It is accompanied by a kinetic energy loss which goes into excitation energy of the products. For collisions where r_{min} is significantly smaller than the interaction radius, nuclei come into solid contact. Then, the reaction's character may be either binary or the compound nucleus is produced, depending on the total angular momentum of the system, energy of the beam and masses of the nuclei. In case the system is in the deep-inelastic regime, the ions interact very strongly and a large amount of kinetic energy is converted into internal excitation energy, however, in the exit channel there are still two different fragments. For more central collisions, the fusion reactions occur, where the kinetic energy dissipates fully and the total angular momentum of the system becomes the spin of the compound nucleus. This is followed by the emission of nucleons or α particles followed by cascades of γ quanta. Alternatively, the compound nucleus fissions in two almost symmetric fragments. The products of fusion-evaporation reactions lie mostly on the neutron deficient side of the stability valley (this is so because the valley bends toward more neutron-rich nuclei with increasing mass so that the product of two lighter mass nuclei ends up in a neutron-deficient nucleus) and this is the reason for having the high-spin structure in this region well explored.

The following features are characteristic for deep-inelastic reactions: formation of a dinuclear system which rotates almost rigidly, damping of the relative kinetic energy between the reaction partners, and transfer of the angular momentum into intrinsic spin of the reaction products. Moreover, even though the products exchange a considerable number of nucleons they retain their projectile- and target-like character. The exchange of nucleons is governed by the N/Z equilibration, which results in population of neutron-rich nuclei, especially from the region of the lighter partner. As regards the spins of the primary fragments produced in DIC, it was shown that average angular momentum of the heavy products in those reactions can be as high as 30 $\hbar$ [57]. Thus, deep-inelastic reactions might be very valuable as a means of preparing excited nuclei with well-defined high angular momenta.

Although the maxima of the distribution of the products are close to the projectile and target nuclei, large fluctuations occur, both in the charge and in the mass distributions. The widths of the distributions strongly depend on the dissipated energy (they increase with increasing energy) and may reach up to several dozens of mass units and over a dozen of charge units. Finally, the production cross-section is spread over hundreds of nuclei, emitting a large number of γ-ray cascades. Thus, special experimental techniques must be employed for γ-ray measurements and analysis of the collected data is a considerable challenge.

Since nearly a two decades, a series of experiments have shown that the yrast states of neutron-rich nuclei, populated in deep-inelastic reactions, can be studied very successfully [58], especially in γ-γ thick target measurements [59, 60]. The resolving power of the large detector arrays has proven sufficient to extract detailed information from coincidence data sets with large statistics, even for weak reaction channels, hence the structures of hard-to-reach nuclei became available for yrast spectroscopy.

3.1.2 Neutron capture reaction ^{209}Bi(n,γ)^{210}Bi

In addition to investigations of yrast structures in the ^{205,206,210}Bi isotopes, complementary studies of low-spin spin states in ^{210}Bi were performed. This was accomplished by measuring γ-ray emission following the cold neutron capture reaction ^{209}Bi(n,γ)^{210}Bi. By employing such a process, one can access rather low-spin states which often cannot be populated in charged-particle-induced reactions. Those states are located at excitation energies up the neutron binding energy.

As neutrons are electrically neutral, they can directly interact with the atomic nucleus without a Coulomb barrier to overcome. The possible reactions between the neutron and the nucleus depend on the incident neutron energy. For low energies, the neutron capture takes place and the $(A{+}1)$ – nucleus is formed usually in an excited state. This process can occur even for very low energies, of the orders of meV. Otherwise, for energies of MeV, other nuclear reactions become important. The cross sections for neutron capture can vary for different nuclei of several orders of magnitude – for ^{209}Bi this value is $\sigma = 3.38 \cdot 10^{-2}$ b.

After the neutron capture, an excited state is formed, which can usually be treated as a compound-nuclear state, that is, as many unresolved individual levels [61]. Occasionally, the capture state may be dominated by one or a few resonances. A resonant state usually corresponds to a complex configuration, where many particles and holes are involved. Its lifetime is of about 10^{-15} s and it can decay through the energetically allowed channels (mainly γ-ray or a neutron emission). In the presented experiment, the energy of the neutron ($\sim$ 5 meV) was too low to produce the lowest resonance state known so far in ^{210}Bi, which was found at 801.6-eV energy [53] thus the final products were populated at excitation close to the separation energy of the neutron in ^{210}Bi, i.e., 4604.63 keV [52]. The J^{π} value of such produced state is restricted to two possibilities. The thermal and cold neutrons, can be described as a s-wave with l=0 and spin s=1/2 [61, 62] because of the wavelength, which is significantly larger than the size of the nucleus (for cold neutrons and ^{209}Bi those values are ~4 Å and ~7 fm, respectively). Thus, the J^{π} value of the populated level, resulting from the coupling of the spins of neutron and the ^{209}Bi ground state, J^{π}=9/2^{-}, must be equal 4^{-} or 5^{-}.

The deexcitation is carried out by so called 'primary' γ radiation, which is often of $E1$ character [61]. The γ decay is very complex, even hundreds of levels may be populated. This gives an opportunity to study in details the low-spin structure, as most of the low-lying states are populated, however such investigations may require use of special experimental setups, i.e., multidetector arrays, and the analysis is rather time-consuming.

3.1.3 Gamma decay

The transitions between the nuclear states with different energies can be associated with the emission or absorption of electromagnetic radiation. Competing process is the transfer of energy to the electron (internal conversion). These processes, connected with the electromagnetic properties of nucleons, depend on the structure of the nucleus. Thus, theoretical expectation based on a given model of this structure can be tested by comparisons with the experimental results. One can test the characteristics of nuclear levels such as: spin, parity, life times depending on the probability of deexcitation to another state as well as the static electric and magnetic moments.

After a nuclear reaction, the final nuclei are produced usually in their excited states. In the case of DIC described in Sec. 3.1.1, $10^{-19} - 10^{-17}$ s after the separation of the products emission of light particles: protons, neutrons and alphas begins and the nucleus loses a major part of excitation energy. The deexcitation by γ-ray emission occurs when the amount of the energy is not sufficient to emit a nucleon ($10^{-16} - 10^{-15}$ s after the collision, or more in case of isomers); after this process the nucleus usually comes to the ground state.

Also in case of cold neutron capture (Sec. 3.3.1) the nucleus is produced in an excited state of which the energy equals the binding energy of the neutron. This process is followed by emission of γ rays – the decay proceeds through low-spin states which can be studied in this way.

The nucleus being in an excited state E_i can spontaneously deexcitate to the state with lower energy E_f by emitting a quantum with energy $E_g = h\nu = E_i - E_f$. If a state at high excitation energy and spin is considered, its decay proceeds through a cascade of γ rays through different intermediate levels. Coincidence measurements are thus a very convenient way of studying the arrangement of excited levels because they allow to detect γ rays from the same cascade.

The quanta can take away different amounts of momenta (excluding $l = 0$): $l = 1$ – dipole radiation, $l = 2$ – quadrupole radiation, $l = 3$ – octupole radiation. γ rays with given order of multipole can occur as electric or magnetic radiation, depending on which component is dominant. The possible values of momenta l_E and l_M are defined by the conservation laws of angular momentum and parity. Between the angular momentum l taken by the γ quantum and momenta (I_i, I_f) and parities (P_i, P_f) of initial and final nuclear states the following relationships must be fulfilled:

$$|I_i - I_f| \leq l \leq I_i + I_f, \tag{3.2}$$

$$P_i \cdot P_f = (-1)^{l_E},\ P_i \cdot P_f = (-1)^{l_M+1}. \tag{3.3}$$

According to formula 3.3, transitions of $E1$ or $M2$ character are possible only between levels with different parities, while $M1$ or $E2$ occur between states with the same parities.

3.2 Experiments at Argonne National Laboratory

3.2.1 Experimental setup

The vast distribution of final nuclei produced in deep-inelastic processes makes the γ-ray spectra very complex, leading to the problem of the assignment of γ quanta to particular products. This difficulty can be overcome by using multidetector Ge arrays, which make possible γ-ray coincidence measurements with high efficiency. The best available system for this type of investigations is Gammasphere [63] at the Argonne National Laboratory. The two experiments which provided the data on yrast structures in Bi isotopes, were performed at Argonne National Laboratory with a ^{76}Ge (450-MeV) and ^{208}Pb (1446-MeV) beams from the Argonne Tandem Linear Accelerator System (ATLAS) on a ^{208}Pb target with the use of the Gammasphere array.

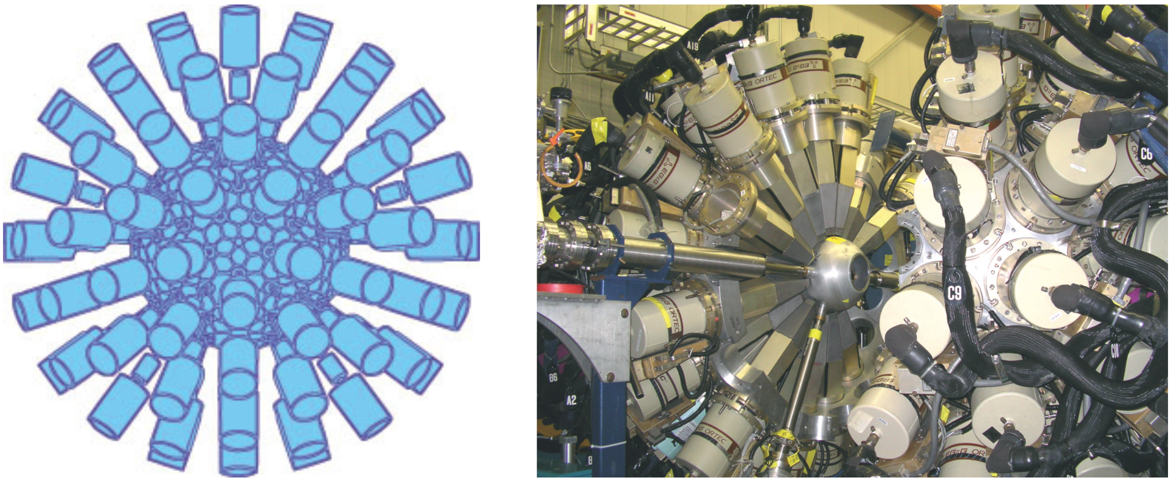

Figure 3.2. Schematic view of Gammasphere array (left); picture taken from [64]. A picture of the real setup of Gammasphere array (right).

Gammasphere is 4π array, which consisted at the time of measurements of 101 working Compton-suppressed n-type Ge detectors [63]. The total efficiency of the HPGe (High Purity Germanium) detectors used in this system is ~10% for 1.3 MeV γ rays with energy resolution

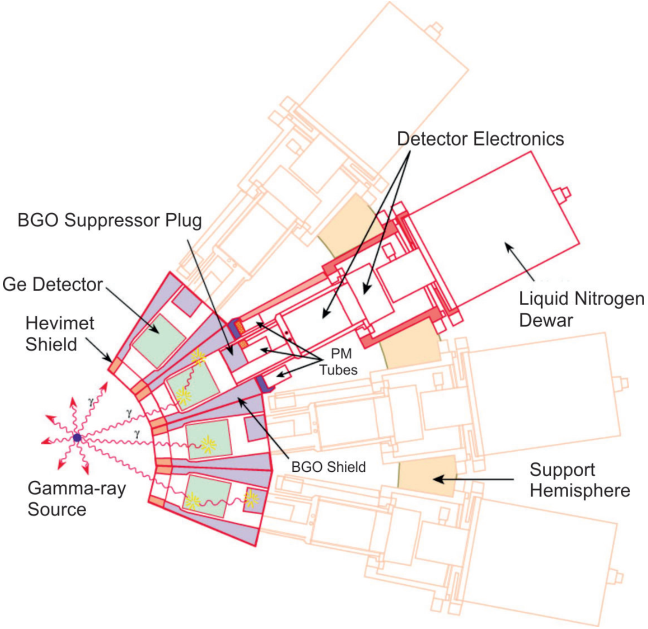

Figure 3.3. Detailed view of the detectors. Picture adapted from [64].

for particular detectors not exceeding 2.5 keV. High granularity (small solid angle of individual Ge detectors) of the system reduces the probability of two γ rays from one event hitting the same detector. The total solid angle coverage is 0.5 sr. Anti-Compton suppressors made of BGO scintillators, working in anticoincidence mode with Ge detectors, reject the pulses which are the result of Compton scattering, thus increasing the peak-to-total ratio. Another important feature of Gammasphere is that the detectors are arranged into six rings symmetric around 90°, what makes a γ-ray angular distributions analysis possible – this will be described in more details in subsection 3.2.3.

The schematic picture of the detection system which was used during the experiments is presented in Fig. 3.2, while a more detailed view of an individual detector arrangement within Gammasphere is shown in Fig. 3.3. The target was placed in the center of the spectrometer. In both experiments the target was a ^{208}Pb foil with thickness of 56 mg/cm^2 for the ^{76}Ge+^{208}Pb experiment and 75 mg/cm^2 in the case of the ^{208}Pb+^{208}Pb reaction. In thick-target experiments, reaction products stop in the material of the target within picoseconds. Thus, γ rays emitted after the stopping time are not affected by the Doppler effect and appear in the spectra as sharp lines. This fact is crucial for the analysis, because it permits setting well defined coincidence gates and it displays discrete γ transition as sharp lines.

The heavy-ion beams used in the experiments presented here had energies about 15-25% above Coulomb barrier. The intensity of the beam was around 1-2 pnA, which equals to 0.6-1.2×10^{10} ions per second. The beam, coming in bursts with a ~0.3-ns time width, was pulsed with a 412-ns repetition rate, i.e., one of five pulses provided with 82.5 ns frequency by ATLAS accelerator was let through. Such time structure allowed for the clean separation between prompt events, when emission of γ rays occurs during the beam pulse and delayed events, when γ rays follow isomeric, α or β decays.

3.2.2 Gamma coincidence measurements

The data from the two mentioned experiments were collected with an event trigger requiring three or more Compton-suppressed γ rays to be measured in coincidence within a 2 µs time window. If that condition was satisfied, the pretrigger (PT) signal was generated at the time of the third detected γ ray. Subsequently, the system waited for ~700 ns and checked if the number of remaining active detectors is still sufficient to satisfy the mastertrigger (MT) condition. At the end of this delay, any of Ge detectors, whose corresponding BGO shield fired was rejected. Every valid MT signal was correlated in time with the third coincident γ ray. Each event contained energy and timing information for all Ge detectors that started the acquisition or fired within 1 µs of the MT signal.

During the off-line analysis, conditions were set on the time parameter to obtain various versions of double and triple coincidence histograms. E_γ-E_γ matrices and E_γ-E_γ-E_γ cubes were constructed, where on the specific axis were the energies of coincidence γ rays. They covered γ-ray energy ranges up to ~4 MeV. A total of 2.1×10^9 and 2.7×10^9 three- and higher-fold events were recorded for ^{76}Ge+^{208}Pb and ^{208}Pb+^{208}Pb measurements, respectively.

The γ-coincidence analysis allows to resolve very complex γ-spectra collected from products of reactions occurring during the experiments. A large number of excited nuclei populated in these processes emit γ rays, which contribute to the total histogram. Since in the thick targets, like the ones used in these experiments, the information about reaction kinematics is lost, the method to identify the products, without the recoils detection, is by selecting the energy of γ transitions. The energies of the peaks in the spectra are characteristic for a given nucleus. Very often the products are isotopes previously studied, thus some spectroscopic information about their structures is available. Thanks to this information, identification of the newly observed cascades from investigated nuclei is possible. When a new transition is visible in coincidence with other lines characteristic for a given nucleus, one can state that the quantum of interest also comes from that product.

Coincidence between a pair of γ rays was defined as prompt if their detection time was within 65 ns with respect to the beam pulse. $\gamma\gamma$ and $\gamma\gamma\gamma$ coincidence histograms which were built with this condition allowed to investigate the states which would be fed shortly after the collision and decay within at most nanoseconds after that. In turn, the ‘off-beam’ matrices were obtained assuming that γ rays satisfy two conditions: they are detected in the time between beam pulses and they are in mutual coincidence. Such matrices were effective source of information about the cascades following the longer-lived isomeric decays, as well as α or β decays. Matrices constructed with the requirement of having, for example, one prompt and two delayed (detected between beam pulses) γ rays were instrumental in identifying transitions preceding the isomers. To analyze half-lives of the isomeric states, the E_γ-E_γ-T_γ cubes were constructed, where T_γ was the time difference between detection time of the two γ rays. The time range available for state lifetimes analyses was from a few ns up to about 2 µs. The shorter isomers placed below longer isomeric states could also be identified by using E_γ-E_γ-T_γ cube for which the prompt component was removed.

The intensity balance between transitions belonging to a decay cascade provided another important source of information regarding the character of the transitions involved. For example, the obvious rule that the sum of the intensities of transitions populating a given state must be equal to the sum of the intensities that deexcite this state allowed to obtain the internal conversion coefficients. Another feature which is related to the intensity balance is that, in the case of isomers, the intensity of the branches along the decay path observed in the 'off-beam' matrix should be constant, while, in the 'in-beam' matrix, the states fed directly in-beam (prompt feeding) should display the intensity which decreases with rising spin and excitation energy. This feature allows to calculate prompt to delay ratio of intensities and in consequence determine the order of lines in the cascades. Existence of parallel branches of the decay from a given state can also be helpful in constructing the level scheme, because the sums of γ-ray energies in parallel cascades connecting a given initial level with a particular final state must be consistent.

A nice characteristics of γ-ray spectroscopic studies with DIC is that coincidences between γ rays emitted from two reaction products can be observed. This feature can be used for identification purposes: by setting gates on the known transitions in one of the reaction partners, γ rays emitted from the complementary fragments can be displayed. This is called the cross-coincidence technique [58]. When performing in-beam experiments with pulsed beam, one has to monitor the amount of random coincidences, which may make the analysis complicated. In the case of measurements presented here, the probability of two nuclear collisions occurring in one beam pulse was reduced to less than 1% – this was sufficient to avoid problems with random coincidences. However, such identification of γ rays still may take much effort due to the high complexity of the spectra. As there is a large number of γ rays, some energies of transitions are similar or the same in various products; therefore a lot of spectra must be produced (or cross-checking in another data, e.g. from experiments with different reaction partners is needed) to build consistent level scheme and calculate the intensities of the transitions. Moreover, to identify very weak transitions, one has to often sum a few spectra, constructed by gating on different pairs of γ rays, to gain better statistics.

3.2.3 Angular distributions of γ rays

The deexcitation of a nucleus by γ quanta (or particles, in general) is not isotropic: the probability of γ-ray emission in a particular direction depends on the angle between the nuclear spin vector and the direction of emission. If the ensemble of nuclei is randomly oriented in space, one observes the isotropic distribution. To obtain the anisotropic radiation pattern, the nuclear spins orientation must not be isotropic. This can be realized by use, for example, of a magnetic field or it can be a result of the reaction. The latter situation occurs for the products of deep-inelastic collisions: their spins show a specific alignment which has been evidenced in earlier works in 1970s [65, 66, 67] as well as observed lately [68]. The alignment is resulting simply from the kinematics of the reaction. The initial momentum of the system of two nuclei, the projectile and the target, has an angular momentum arising from their relative motion and spins, perpendicular to the beam direction. Then, the rotating complex has also angular momentum perpendicular to the beam. Next, after the separation

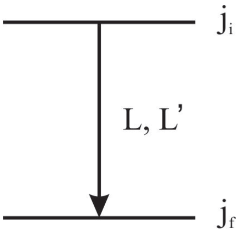

Figure 3.4. Gamma decay from initial to final state with spins j_i and j_f by a quantum of a mixed multipolarity.

of products, there is a partition of the total angular momentum between the spins of final nuclei and the orbital angular momentum of the whole system. The vectorial sum of all these spin components must be perpendicular to the beam axis. Thus, the vectorial sum of spins of the products also should be perpendicular to the beam direction. It has been shown that, in spite of the significant dispersion of products spin direction, they still maintain an overall alignment in the plane perpendicular to the beam. This is the same situation as in fusion-evaporation reactions and the familiar formalism for the angular distributions of γ rays emitted from DIC products can be applied [69, 70] – it is briefly presented below.

For a state with angular momentum j its spin has $2j+1$ components m $(m = -j, ..., j)$ along chosen quantization axis. As the direction of the products of deep-inelastic reactions are not measured in a thick target experiment, the only definite axis in the laboratory frame of reference is the beam direction. In the real, experimental situation, we do not deal with an individual state characterized by m quantum number, but an ensemble of states. Because of the lack of more detailed information, the occupation of the m-states of products is usually described by the population parameter $P_m(j)$ given by a Gaussian distribution – Eq. 3.4. The width of this distribution is a single, free parameter determining the degree of alignment ($\sigma = 0$ means the complete alignment):

$$P_m(j) = \frac{exp(-\frac{m^2}{2\sigma^2})}{\sum\limits_{m'=-j}^{j} exp(-\frac{m'^2}{2\sigma^2})}. \tag{3.4}$$

Gamma rays deexciting spin-aligned reactions products exhibit angular distribution depending on their multipolarities and the spin sequences. The angular distribution function is parameterized by the three coefficients A_0, A_2, and A_4 of the Legendre polynomials $P_n(\cos\theta)$ in:

$$W(\theta) = A_0[1 + A_2P_2(\cos\theta) + A_4P_4(\cos\theta)], \tag{3.5}$$

where

$$A_n = \alpha_n B_n(j) F_n(\delta),\ with\ n = 2, 4. \tag{3.6}$$

A_n coefficients (Eq. 3.6) depend on the angular momentum alignment of the nucleus resulting from the reaction, the spins of the two levels involved in the γ decay, as well as on the multipolarity and mixing ratio δ of the transition. α_n are the attenuation coefficients, and $B_n(j)$ – statistical tensors for complete alignment. The width of the distribution can be extracted from the attenuation of the A_2 coefficient determined for a known transition. The α_2 value also determines the attenuation of the A_4 coefficient.

If the radiation consists of two types of multipole (i.e. is mixed) the mixing ratio δ can be defined as the ratio of the transitions amplitudes from the initial to final state:

$$\delta \equiv \frac{\langle j_f||L'||j_i\rangle}{\langle j_f||L||j_i\rangle}. \tag{3.7}$$

The multipole orders usually differ by 1. The ratio of the total intensity of the L' pole to that of the L pole is equal to δ^2:

$$\delta^2 \equiv \frac{I_{L'}}{I_L}. \tag{3.8}$$

This quantity can be calculated from the relationship $F_n(\delta)$:

$$F_n(\delta) = \frac{1}{1+\delta^2}\left[F_n(j_fLLj_i) + 2\delta F_n(j_fLL'j_i) + \delta^2 F_n(j_fL'L'j_i)\right], \tag{3.9}$$

where F_n functions are tabularized [70]. It should be mentioned, that the sign of δ obtained from the analysis of angular distribution for particular γ-transition is opposite to the one obtained from $\gamma\gamma$-angular correlations for the $j_i \to j \to j_f$ cascade, described in subsection 3.3.2.

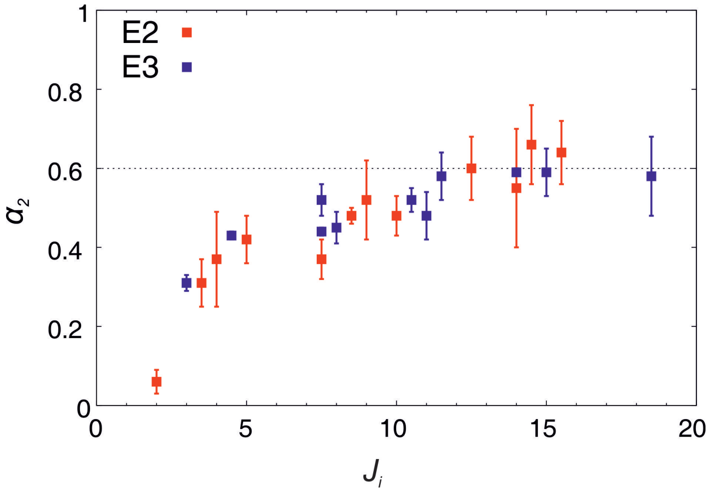

Figure 3.5. Attenuation coefficient α_2 calculated for the pure $E3$ and $E2$ γ transitions from strongly populated products of ^{208}Pb + ^{208}Pb reaction.

To perform such analysis on the data obtained from a deep-inelastic experiment one can use the fact that each detector in Gammasphere is associated with a pair of angles (θ,ϕ) with respect to the beam direction. This allows to divide detectors into six rings around the beam axis with average values of θ: 17.3°, 35.5°, 52.8°, 69.8°, 79.9°, 90.0° with equivalent rings at backward angles. The number of double and triple γ-coincidences that was acquired during the experiments with ^{76}Ge and ^{208}Pb beams was sufficient to carry out an analysis of the angular distribution for the strongest lines in the Bi isotopes. The gates were set on transitions in in-beam coincidence matrices (or cubes) and γ-ray yields detected in a specific ring were obtained. To get a proper result one has to normalize the number of counts obtained for a given ring, taking into account the number of detectors in this ring and other factors that may influence the ring's efficiency (for example, the additional dead-time in forward detectors associated with neutron emission). The counts in various rings were normalized in most cases using the isotropic distribution of the 516-881-803-keV cascade deexciting the 125-µs isomer in ^{206}Pb [71]. That way, the normalized intensity of a transition can be expressed as a function of the detection angle, as in Eq. 3.5.

It is known that the spin alignment of an excited nuclear state produced in nuclear reaction depends on the value of spin [70]. This effect was experimentally observed in the present work for the system ^{208}Pb + ^{208}Pb: it was done by analyzing the angular distributions of pure $E3$ and $E2$ transitions known in nuclei strongly produced in this reaction and by extracting subsequently the α_2 attenuation coefficient for those transitions. The results are displayed in Fig. 3.5 where one can see that α_2 coefficient shows a tendency to saturate at spin 23/2 for a value of 0.6. The average value of α_2 extracted from 8 points is 0.6(1).

3.3 Experiment at Institute Laue-Langevin

3.3.1 Experimental setup and coincidence measurements

The experiment was performed at the PF1B cold-neutron facility in the Institute Laue-Langevin in Grenoble. The neutron beam from ILL reactor, after travelling through the collimation line, had a diameter of 12 mm and the capture flux was about $10^8/(\mathrm{s}\times\mathrm{cm}^2)$ at the target position. The target was a 3 g solid cylinder of ^{209}Bi placed in the center of EXILL array. This array consisted of 8 EXOGAM clover detectors [72] and 6 GASP detectors [73] with their BGO anti-Compton suppressors, as well as two clovers from the ILL LOHENGRIN collaboration [74].

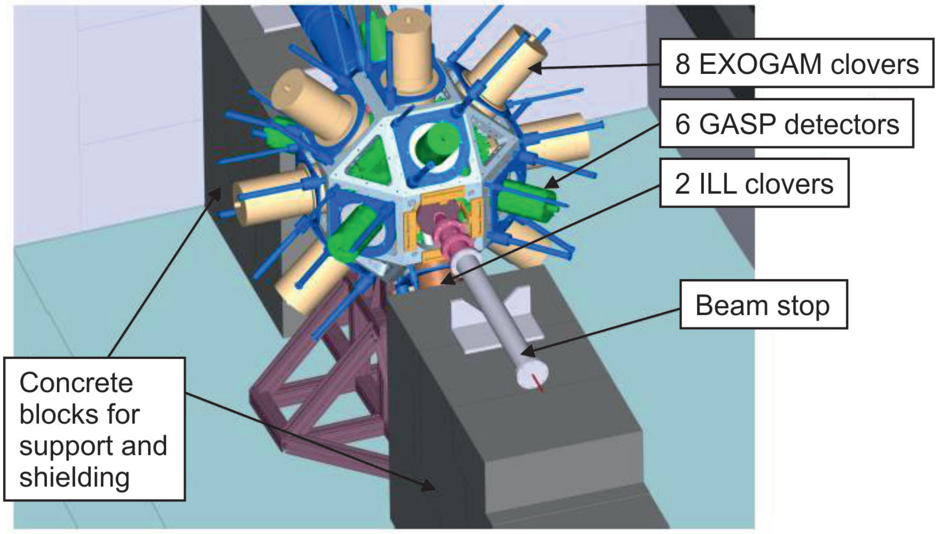

Figure 3.6. The EXILL setup [75].

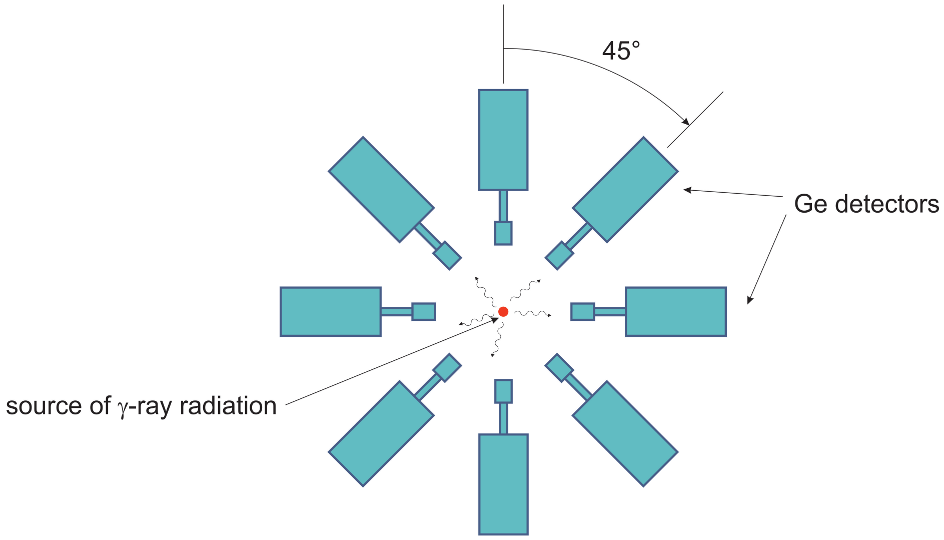

Figure 3.7. Schematic picture of ILL EXOGAM detectors. The direction of the beam is perpendicular to the plane of the figure.

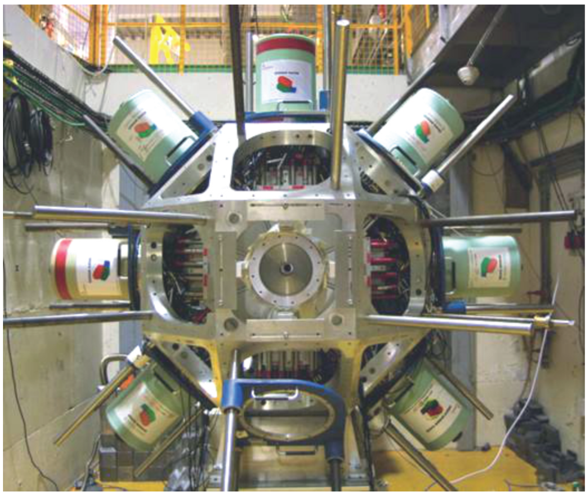

Figure 3.8. A picture of the real setup of the EXOGAM ring.

The neutron capture reaction led to ^{210}Bi, which then would decay through emission of γ-ray cascades. As the measured γ-spectrum was very complex due to a large number of decay paths, the γ-coincidence technique was applied. To collect and process the signals from the detectors, digital electronics was used and the data were stored trigerless. The events contained information about γ-ray energy, the time of the registration (with a time stamp every 10-ns) and the ID of the specific detector that fired.

The data were sorted offline into $\gamma\gamma$-coincidence matrix and $\gamma\gamma\gamma$-coincidence cube with a coincidence time window of 200 ns. The energy calibration was done based on the contaminant strong peaks from ^{28}Al and ^{36}Cl isotopes. The procedures of time and energy calibration are described in details in [76]. The gating on the already known, low-spin transitions in ^{210}Bi allowed to produce coincidence spectra, the analysis of which resulted in building the level scheme of this nucleus below the state which was populated after neutron capture. Although mainly ^{210}Bi was produced in this reacton, in contrast to DIC, the collected data contain many peaks. This is because of the large number of primary γ rays feeding numerous states. Thus, this analysis was challenging as well, because it required identification of the many various paths of the decay – constructing a lot of coincidence spectra was necessary to build a complex level scheme.

3.3.2 Angular correlations of γ rays

As described in section 3.2.3, to observe anisotropy in the emission direction of a γ-ray radiation one needs to provide orientation of nuclear spins. While in case of deep-inelastic collisions such orientation resulted from the character of the reaction, after the neutron capture the final nuclei are randomly oriented. One needs then a method to specify the nuclei with preferred direction of the spin. In γ-ray coincidence measurements this may be realized by choosing a particular transition in a fixed direction, which will select an ensemble of emitters with nonisotropic orientation of the spins. The rest of the transitions emitted in coincidence with that γ ray of reference should show a nonisotropic angular distribution with respect to the emission direction of the chosen one. In practice, the detectors are divided into groups depending on the relative angle between them.

The angular correlation function is usually expressed (similarly to angular distribution fuction) as the sum of Legendre polynomials $P_n(\cos\theta)$ parameterized by coefficients A_2 and A_4 [70, 77]:

$$W(\theta) = A_0[1 + A_2P_2(\cos\theta) + A_4P_4(\cos\theta)]. \tag{3.10}$$

A_n is the product of two coefficients $A_n(1)$ and $A_n(2)$ depending on the character of two considered γ rays:

$$A_n = q_nA_n(1)A_n(2), \ \ with\ n = 2, 4 \tag{3.11}$$

where q_n are attenuation coefficients associated with the finite solid angle of the detectors (geometry and size of the crystal, distance from the radiation source) and may be calculated from theory or extracted from experimental data. The coefficients A_2 and A_4 depend on the following parameters: the multipole orders L_1 and L_2 of the γ rays and the spins j_i, j, and j_f of the nuclear states. If a γ ray is a mixture of two multipoles, the equation for $A_n(k)$ coefficients is:

$$A_n(k) = \frac{1}{1+\delta_k^2}\left[F_n(j_iL_iL_ij) + 2\delta_kF_n(j_iL_iL_i'j) + \delta_k^2F_n(j_iL_i'L_i'j)\right], \tag{3.12}$$

where F_n functions are tabularized [70]. Thus, from the measured A_n coefficients of the angular correlation function one can determine the mixing ratio δ of the considered transition by solving an elementary quadratic equation.

Full information about the order of multipole and the mixing ratio of one transition can be obtained only if the second transition is pure or its mixing ratio is well defined. The type of multipole (electric or magnetic) and, as a result, the change of parity cannot, however, be defined. Thus, the angular correlation measurements do not allow to completely determine all the characteristics of a transition. Only in conjunction with other methods it is possible

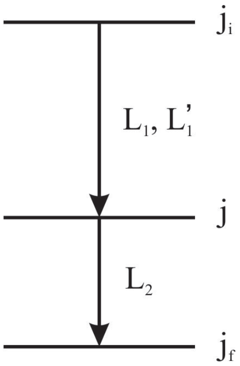

Figure 3.9. Gamma cascade from initial to final state characterized by spins j_i and j_f through the intermediate state with spin j by the quanta, the first of which is of mixed multipolarity.

to establish a complete decay scheme. The mixing ratio is defined similarly as in the angular distribution method, but the convention used in case of this formalism causes a change of the sign when comparing to the one obtained from angular distributions in Eq. 3.7 (the discussion of the sign can be found for example in [77]). Let us consider the first γ ray:

$$\delta \equiv \frac{\langle j_i || L'_1 || j \rangle}{\langle j_i || L_1 || j \rangle}. \tag{3.13}$$

The ratio of the intensities of L pole to L' pole radiation defines a mixing ratio:

$$\delta^2 \equiv \frac{I_{L'_1}}{I_{L_1}}. \tag{3.14}$$

The formula 3.13 is constructed in such a way as if the intermediate state with spin j were the initial state for both transitions. The sign of δ is related to the direction of the transition $j_i \rightarrow j$). Therefore the sign of $\delta(j \rightarrow j_i)$ determined from the angular correlation of the pair of γ rays is opposite to the one calculated from the coefficients of angular distribution function for transition $j_i \rightarrow j$.

As the detectors of EXOGAM used in the experiment were placed in one ring in octagonal geometry (as shown in Fig. 3.7), the double γ-coincidence data could be sorted into three matrices corresponding to average angles between detectors of 0° (in practice 180°), 45° (and 135°), and 90°. The number of counts in a given peak of a particular matrix was normalized depending on the number of detector pairs available in each of the three groups (4, 16 and 8 for the angles 0°, 45°, and 90°, respectively). The attenuation coefficients q_n were determined by using cascades from ^{60}Co and ^{152}Eu sources with well-defined anisotropies [76]. This resulted in $q_2 = 0.87$ and $q_4 = 0.6$ coefficients [78].

CHAPTER 4

Experimental results

4.1 ^{206}Bi

As discussed in Section 2.2, the level scheme of ^{206}Bi was established in earlier studies up to the 18^+ state at 4307 keV [41], decaying via a cascade of a few γ rays that feed the 10^-, 0.89-ms isomer at 1045 keV. The analysis of the data from the present ^{76}Ge+^{208}Pb deep-inelastic experiment fully confirmed this known part of the ^{206}Bi decay scheme – it is printed in black and white in Fig. 4.2. One could then use this known part as a starting point for the delineation of higher yrast excitations. Double coincidence gates were placed in the off-beam cube on various pairs of known transitions at 701, 458, 505, 543, 548, 266, 744, 150, and 595 keV. Many off-beam coincidence spectra produced in this way - see Fig. 4.1 for representative examples - were investigated and provided clean evidence for new transitions belonging to ^{206}Bi which, apparently, followed the decay of unknown higher-lying isomers.

One of the first findings was a cascade consisting of 1152-, 189-, 214-, 304-, and 417-keV γ rays feeding the first 16^+ state at 3652 keV. The ordering of these transitions was established based on their intensities and the presence of parallel decay branches such as the 1234-, 1371-, and 1388-keV lines. As a result, the location of new levels at 4805, 4993, 5207, 5511, and 5928 keV were located. Further, the first 18^+ state at 4307 keV was found to be populated by a sequence of 1485-, 1102- and 231-keV transitions which establish additional new levels at 5793, 6895 and 7126 keV. The location of the highest of these excitations at 7126 keV was confirmed by the presence of yet another cascade of 777-, 467-, 503- and 1772-keV γ rays connecting it to the lower portion of the scheme via new states at 6349, 5882, and 5378 keV. Further support for the proposed level arrangement came from the analysis of weaker transitions found only by summing the appropriate coincidence spectra. For example, levels placed at 4982, 5096, and 5278 keV were found to be fed by the 1913-231-keV, 513-332-1074-111-keV and 124-110-1234-245-136-keV cascades, respectively. Some of the low-energy transitions at 110, 111, 118, 124, 136, and 245 keV were observed only as weak peaks, even in the summed spectra, most likely because of strong internal conversion. Furthermore, an

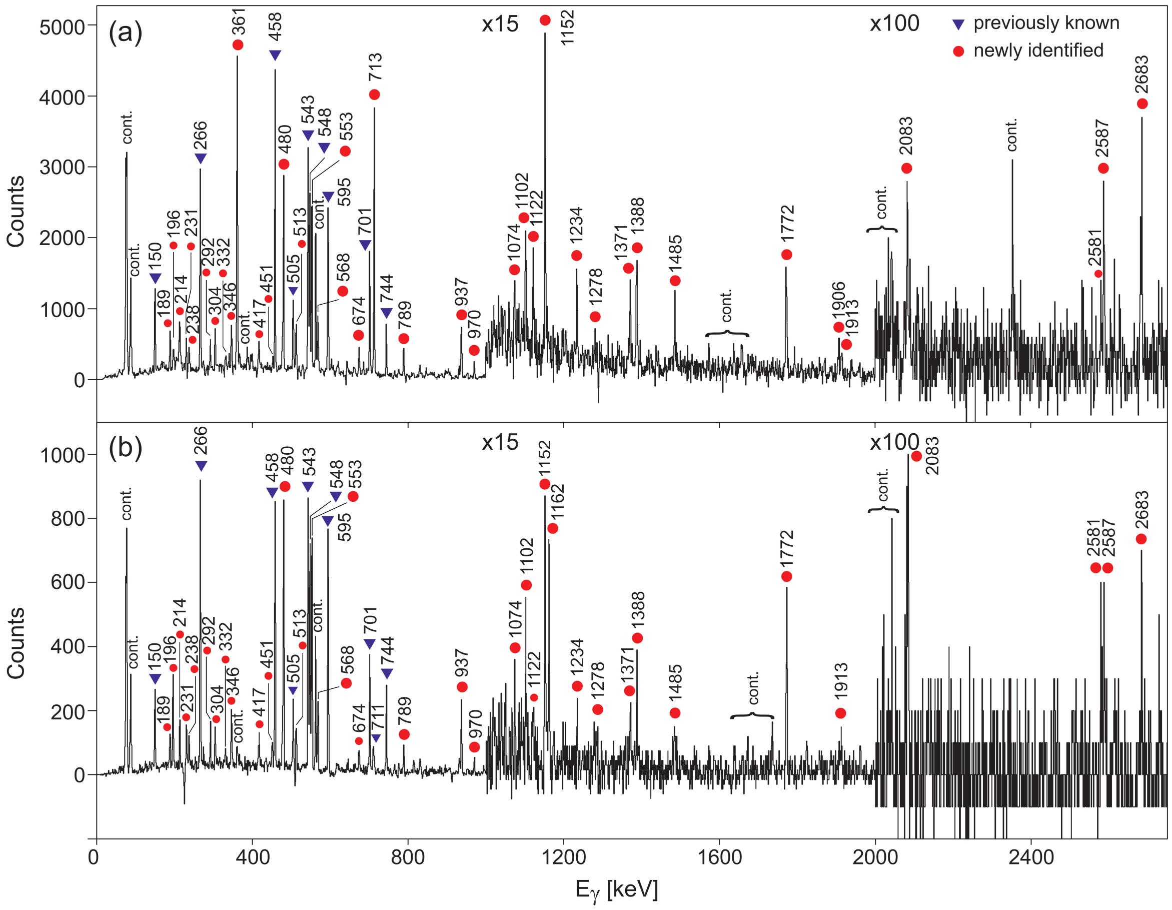

Figure 4.1. Representative off-beam coincidence spectra: (a) sum spectrum double-gated on every pair of transitions at 150, 266, 543, 548, and 595 keV, (b) spectrum gated on the 361- and 713-keV transitions.

addition has been proposed to the structure in the known part of the scheme: a 2951-keV level was defined by the 196-1162-keV cascade and confirmed through a 451-keV decay branch.

While performing the γ-coincidence analysis described above, a set of five intense, mutually coincident γ rays with energies of 361, 480, 553, 713, and 937 keV was found to be present in all spectra. After construction of the complete level scheme up to a level at 7126 keV, it became clear that this new cascade is located above the 7126-keV state. In addition, since all these new lines appeared in the off-beam spectra, it became apparent that they had to belong to a cascade deexciting one or more new high-lying isomers. This strong cascade was, therefore, placed at the top of the level scheme of Fig. 4.2. As it was mentioned, the ratio of prompt to delayed transition intensities has to decrease monotonically with excitation energy of the state of origin of this transition, independently of branching and detector efficiency – see Table 4.1. Using this criterion, the ordering of the 361-, 480-, 553-, 713-, and 937-keV γ rays was determined and is displayed in Fig. 4.2. Eventually, this part of the analysis established new levels at 7679, 8159, 8520, 9233, and 10170 keV above the 7126-keV excitation.

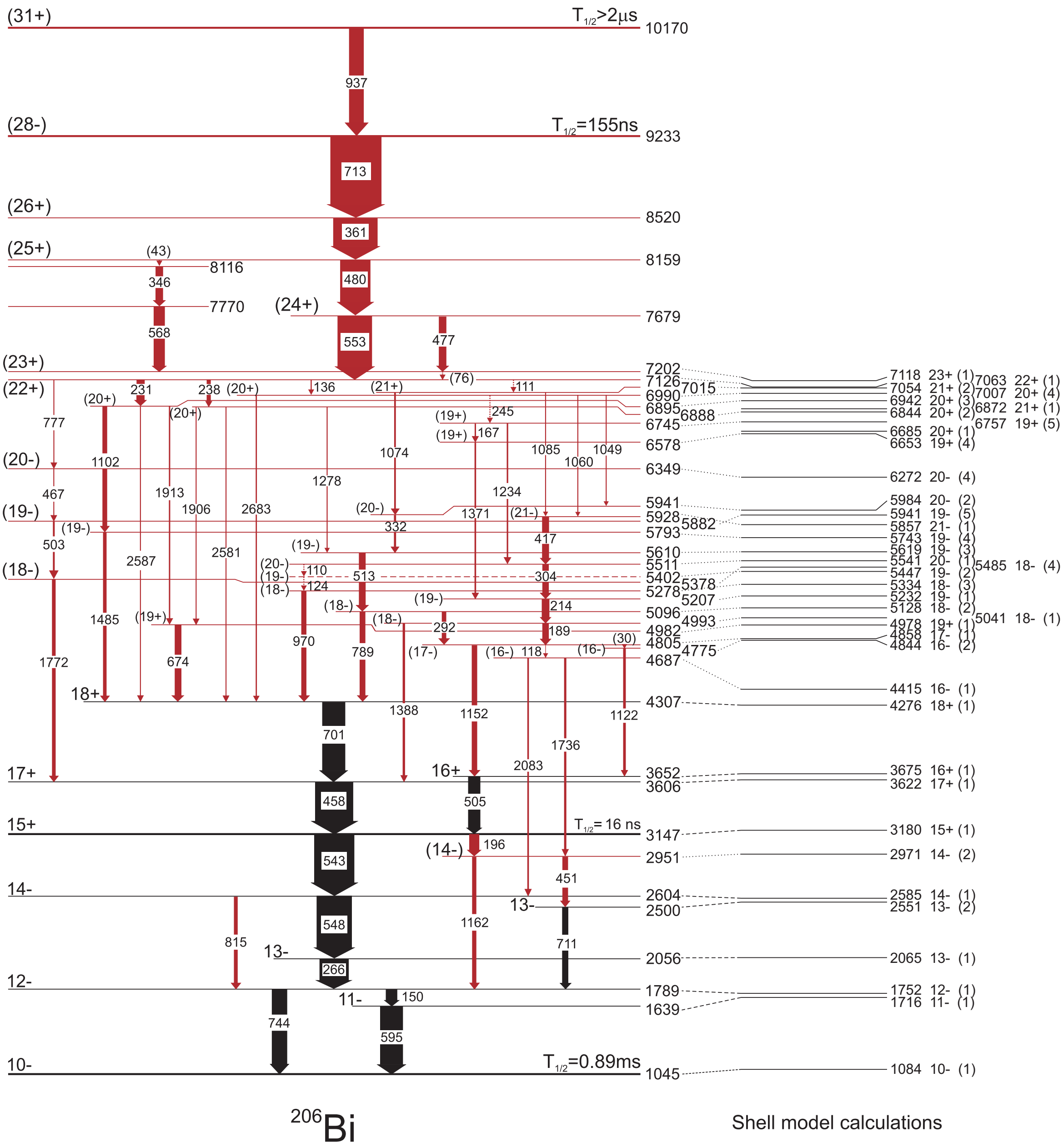

Figure 4.2. Proposed level scheme for the high-spin states in ^{206}Bi (left) compared with the results of shell-model calculations (right). Transitions in red were identified in the present study. Intensities are indicated by the widths of the arrows. Note that the low-spin level structure of ^{206}Bi is not shown, but can be found in Ref. [40]. Note that there is uncertainty of $1\hbar$ for the spin assignments to the levels located above the 7202-keV state; see text for a detailed discussion.

Table 4.1. Information on levels and transitions in ^{206}Bi from the present experiment.

E_i (keV)	J^π_i	E_f (keV)	J^π_f	E_γ (keV)	I_del	I_pr	$\left(\frac{I_\mathrm{pr}}{I_\mathrm{del}}\right)$
1639	11^-	1045	10^-	594.8(1)[a]	71(4)	71(2)	1.00(7)
1789	12^-	1639	11^-	149.8(1)[a]	24(4)	23(1)	0.94(17)
		1045	10^-	744.5(1)[a]	32(2)	31(1)	0.99(9)
2056	13^-	1789	12^-	266.4(1)[a]	61(5)	63(7)	1.04(14)
2500	13^-	1789	12^-	711.0(1)[a]	12(2)	12(3)	1.00(31)
2604	14^-	2056	13^-	548.1(1)[a]	73(5)	73(7)	0.99(11)
		1789	12^-	814.8(1)	8(1)	7(1)	0.89(20)
2951	(14^-)	2500	13^-	451.2(1)	12(2)	12(3)	0.99(31)
		1789	12^-	1161.8(2)	9(2)	8(1)	0.93(27)
3147	15^+	2951	(14^-)	196.0(1)	21(2)	16(3)	0.79(15)
		2604	14^-	543.5(1)[a]	84(7)	80(7)	0.96(12)
3606	17^+	3147	15^+	458.4(1)[a]	79(7)	54(6)	0.68(9)
3652	16^+	3147	15^+	505.1(1)[a]	25(2)	15(3)	0.59(13)
4307	18^+	3606	17^+	701.5(1)[a]	48(6)	20(4)	0.41(9)
4687	(16^-)	2951	(14^-)	1735.7(3)	5(1)	[b]	
		2604	14^-	2083.4(2)	2(1)	[b]	
4775	(16^-)	3652	16^+	1121.9(1)	5(1)	2(1)	0.34(13)
4805	(17^-)	4775	(16^-)	(30)	[b]	[b]	
		4687	(16^-)	118.5(4)	<1	[b]	
		3652	16^+	1152.4(2)	11(2)	8(2)	0.74(22)
4982	(19^+)	4307	18^+	674.5(1)	14(2)	2(1)	0.18(6)
4993	(18^-)	4805	(17^-)	188.6(2)	13(4)	5(1)	0.35(12)
		3606	17^+	1387.9(1)	5(1)	4(1)	0.78(27)
5096	(18^-)	4805	(17^-)	292.0(1)	9(1)	2(1)	0.26(8)
		4307	18^+	788.9(2)	12(3)	6(2)	0.52(19)
5207	(19^-)	4993	(18^-)	213.7(2)	16(4)	6(2)	0.39(14)
5278	(18^-)	4307	18^+	970.4(2)	11(2)	4(1)	0.39(11)
5378	(18^-)	3606	17^+	1772.2(2)	8(2)	6(1)	0.81(24)
5402	(19^-)	5278	(18^-)	124	[b]	[b]	
5511	(20^-)	5402	(19^-)	110	[b]	[b]	
		5207	(19^-)	304.3(2)	13(1)	5(1)	0.39(9)
5610	(19^-)	5096	(18^-)	513.1(1)	14(1)	10(2)	0.69(17)
5793	(19^-)	4307	18^+	1485.4(2)	7(1)	2(1)	0.23(8)
5882	(19^-)	5378	(18^-)	503.4(1)	4(1)	3(2)	0.80(51)
5928	(21^-)	5511	(20^-)	417.0(3)	15(3)	3(1)	0.20(7)
5941	(20^-)	5610	(19^-)	331.6(4)	5(1)	[b]	
6349	(20^-)	5882	(19^-)	466.8(5)	<1	[b]	
6578	(19^+)	5207	(19^-)	1370.7(5)	3(2)	2(1)	0.48(38)

Table 4.1 – continued from previous page

E_i (keV)	J_i^π	E_f (keV)	J_f^π	E_γ (keV)	I_del	I_pr	$\left(\frac{I_\mathrm{pr}}{I_\mathrm{del}}\right)$
6745	(19^+)	6578	(19^+)	166.6(2)	3(1)	[b]	
		5511	(20^-)	1234.5(2)	3(1)	[b]	
6888	(20^+)	5610	(19^-)	1277.9(5)	2(1)	[b]	
		4982	(19^+)	1906.2(2)	2(1)	[b]	
		4307	18^+	2580.8(3)	<1	[b]	
6895	(20^+)	5793	(19^-)	1102.0(1)	10(2)	0.6(2)	0.06(2)
		4982	(19^+)	1913.4(2)	3(1)	[b]	
		4307	18^+	2586.6(4)	2(1)	[b]	
6990	(20^+)	6745	(19^+)	245	[b]	[b]	
		5941	(20^-)	1049.0(2)	2(1)	[b]	
		5928	(21^-)	1059.7(2)	2(1)	[b]	
		4307	18^+	2683.3(4)	3(1)	0.6(2)	0.23(11)
7015	(21^+)	5941	(20^-)	1073.8(2)	4(1)	[b]	
		5928	(21^-)	1085.2(1)	2(1)	[b]	
7126	(22^+)	7015	(21^+)	111	[b]	[b]	
		6990	(20^+)	136	[b]	[b]	
		6895	(20^+)	230.8(2)	17(3)	1.4(3)	0.08(3)
		6888	(20^+)	237.5(2)	8(2)	[b]	
		6349	(20^-)	777.3(2)	<1	[b]	
7202	(23^+)	7126	(22^+)	(76)	[b]	[b]	
7679	(24^+)	7202	(23^+)	477.4(1)	8(1)	1(0.5)	0.08(3)
		7126	(22^+)	552.9(1)	71(10)	7(1)	0.10(3)
7770	[c]	7202	(23^+)	568.3(2)	19(4)	3(1)	0.14(4)
8116	[c]	7770	[c]	346.4(2)	16(3)	2(1)	0.12(4)
8159	(25^+)	8116	[c]	(43)	[b]	[b]	
		7679	(24^+)	480.2(1)	69(6)	5(1)	0.08(2)
8520	(26^+)	8159	(25^+)	361.2(1)	79(10)	6(1)	0.07(2)
9233	(28^-)	8520	(26^+)	713.2(1)	91(5)	4(1)	0.04(1)
10170	(31^+)	9233	(28^-)	937.2(1)	31(5)	0	0

[a] γ rays seen also in Ref. [41]

[b] intensity too weak to be determined

[c] the spin-parity value could not be assigned

In the course of further analysis, double gating on the 553-, 480-, 361-, and 713-keV lines in the prompt-delayed-delayed cube displayed the 937-keV transition which indicated that this γ ray must be preceding in time the 553-480-361-713-keV cascade. This observation pointed to the existence of yet another isomeric state at 9233 keV decaying via the 713-keV line. Gates placed on various combinations of the 744-, 595-, 266-, 548-, 543-, 458-, and 701-keV

γ rays displayed also other transitions belonging to the structure above the 7126 keV-state. These were the 477-keV line (parallel to the 553-keV γ ray) and a cascade consisting of 346- and 568-keV transitions which connects the 8159- and 7202-keV levels. From the differences in energies of the levels, the existence of two unobserved, low-energy transitions: 76 keV (for the 477-keV transition) and 43 keV (for the 346-568-keV cascade) was inferred. Their placement is tentative and will be also discussed in Sec. 5.1. The connection of the 8159- and 7126-keV levels by a 346-568-119-keV cascade was excluded because a required 119-keV transition was not present in the spectra.

The intensities of the identified γ rays were obtained from double-gated coincidence spectra in the off-beam data. At first, the intensities of the 744-, 595-, and 150-keV transitions at the bottom of the scheme were established relative to each other from the spectrum gated on the 266- and 548-keV lines. The next step was to calculate the intensities of the 815-, 548-, 1162-, and 711-keV γ rays from the 595-713 keV gated spectrum assuming that their sum is equal to the sum of intensities measured for the 744- and 595-keV transitions. The intensities of stronger lines were calculated relative to the 548-keV line from the same spectrum. In the case of weaker transitions, the intensities were obtained from the sum spectra; for example, in the spectrum gated on every pair among the 361-, 595-, 713-keV transitions, the intensities of lines such as those at 1906, 1913, 2581, 2587, and 2683 keV were calculated relative to the 458-keV yield. The intensity of the 713-keV line was obtained from the 266-361-keV gated spectrum, relative to the 543-keV transition. All the intensities were normalized to that of the 713-keV line (after the inclusion of the contribution from internal conversion, its intensity was defined as 100). A similar analysis was made for the prompt transitions assuming that the prompt/delayed intensity ratio for the 595-keV line deexciting the lowest observed level (1639 keV) is equal to 1.

The delayed intensity of the higher, strong transition at 713 or 361 keV is equal to the sum of the yields for the 744- and 595-keV γ rays. However, in the medium part of the scheme, below the 7126-keV level, up to 74% of the intensity is missing. This observation indicates that (a) many decay branches remain unobserved, due to their weak intensity, and that (b) the level structure in this region is even more complex than deduced in the present study.

A detailed analysis of the intensity balance for the lines above the 7126-keV level was performed in order to obtain information on the total conversion coefficients of some of the observed transitions. For example, the coefficient for the 361-keV line, 0.26(2), was obtained by comparing its intensity to the sum of the intensities of the 477- and 553-keV transitions (the strong 553-keV γ ray is an $E2$ transition and has a small conversion coefficient) in the spectrum gated on pairs of lines with the 480-keV γ ray and any of the 266-, 458-, 543-, 701-, 744-keV transitions. A similar analysis carried out for the 480-, 553-, and 713-keV γ rays resulted in the determination of their conversion coefficients as well (Table 4.2).

The analysis of prompt-delayed matrices and cubes confirmed the existence of the short-lived isomeric state at 3147 keV. Its half-life could be determined from a spectrum of time differences between the detection time of the 505- and 701-keV transitions with respect to the 266-, 543-, 548-, and 744-keV γ rays below the isomer. The resulting value of 16(1) ns

Table 4.2. Total conversion coefficients $\alpha_{\text{tot-exp}}$, The second column gives the measured delayed intensity, while the third provides the total intensity as expected from the decay scheme. A specific set of gates was applied to reduce the intensity uncertainties. Column 4 presents the total conversion coefficient deduced from the missing γ-ray intensities while columns 5-8 provide the theoretical values for the different multipolarities ($E1$, $M1$, $E2$, and $M2$ multipolarities were considered). The assigned values are marked in bold characters.

E_γ(keV)	I_γ	I_{tot}	$\alpha_{\text{tot-exp}}$	$E1$	$M1$	$E2$	$M2$
118	0.8(4)	7.0(3)	8(4)	2.955E–01	**6.350E+00**	3.367E+00	4.544E+01
361	79.4(11)	100.0(12)	0.26(2)	1.999E–02	**2.805E–01**	7.090E–02	9.400E–01
480	68.6(11)	81.0(14)	0.18(4)	1.079E–02	**1.307E–01**	3.388E–02	3.851E–01
553	70.9(12)	73.0(16)	0.03(4)	8.059E–03	8.980E–02	**2.423E–02**	2.511E–01
713	90.9(13)	100.0(13)	0.10(3)	4.882E–03	4.613E–02	1.385E–02	**1.195E–01**

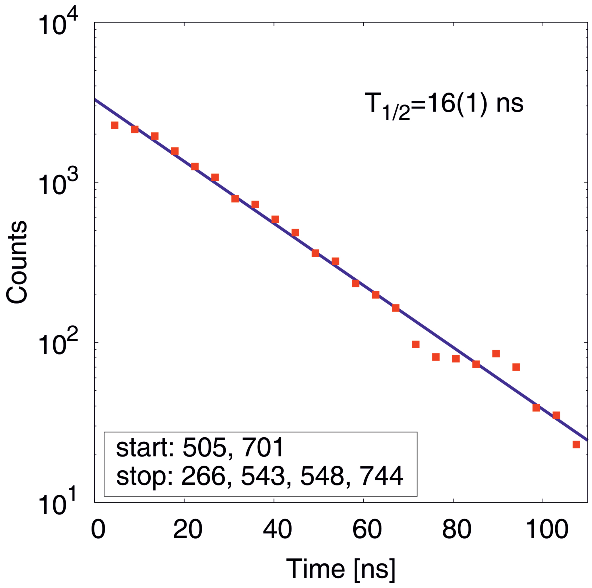

Figure 4.3. Summed time distribution between the 505- and 701-keV γ rays, and any of the 266-, 543-, 548-, or 744-keV lines.

(Fig. 4.3) is in agreement with $T_{1/2}$=15.6 ns reported in [41].

As stated above, the 9233-keV level is an isomer fed by a 937-keV transition. Its half-life could then be determined from a spectrum of time differences between the detection time of the 937-keV γ ray with respect to the 361-, 458-, and 480-keV transitions that deexcite the isomer. The analysis yielded $\text{T}_{1/2}$=155(15) ns (Fig. 4.4). In addition, the 937-keV line deexcites a level at 10170 keV, which is also an isomer. In order to estimate $\text{T}_{1/2}$ for this long-lived state, a time spectrum started by the RF signal of the accelerator and stopped by the detection of the 937-keV transition was constructed while requiring in addition a coincidence between this line and other strong γ rays in the decay cascade (Fig. 4.2). In the electronics setup used here, this spectrum only covers effectively a 400-ns range which was sufficient only to establish that the associated $\text{T}_{1/2}$ value must be larger than 2 µs.

The information on all the transitions and energy levels deduced in the present work is summarized in Table 4.1.

As mentioned earlier, the yrast cascade above the long-lived 10^- isomer extending up to an 18^+ level was established and the spin-parity of the states determined with the help of

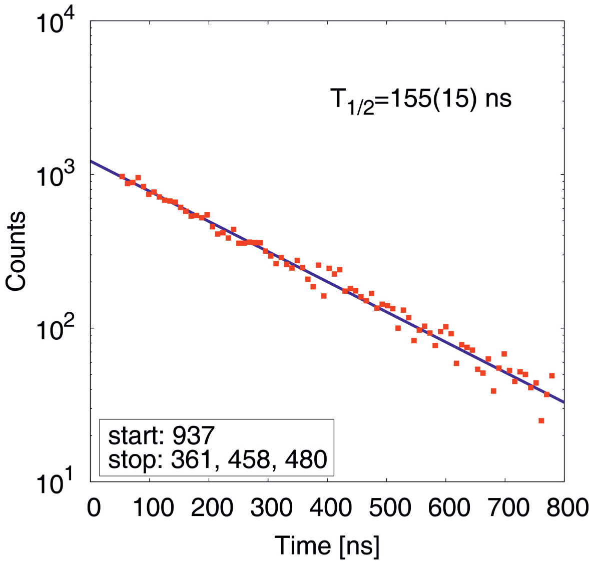

Figure 4.4. Summed time distribution between the 937-keV γ ray, and any of the 361-, 458-, or 480–keV lines.

γ-ray angular distributions following the ^{205}Tl(α,3$n\gamma$)^{206}Bi reaction by Lönnroth *et al.* [41]. In order to check, whether the ^{206}Bi states populated in the ^{76}Ge+^{208}Pb experiment exhibit sufficient spin alignment to use γ-ray angular distributions for multipolarity assignments, the low-lying, intense γ rays in ^{206}Bi were first investigated. The procedure described in Sec. 3.2.3 was applied.

The intensities of the lines observed in six rings of the Gammasphere array were used to construct their angular distributions. To obtain cleaner spectra, a cube was constructed for each ring from prompt triple coincidence events. The γ rays detected in a specific ring were allocated to one axis and the two other coincident photons from any detector in other rings to the other two axes. Spectra for the rings were then generated by double gating on any pair of the 361-, 480-, 553-, 970-, 701-, 458-, 543-, 548-, 266- and 744-keV lines. Sample angular distributions obtained in this way are presented in Fig. 4.5.

Table 4.3. The measured angular-distribution coefficients A_2 and A_4 and the ensuing mixing ratios δ.

E_γ (keV)	Multipolarity	A_2	A_4	δ
361	$M1$	$-0.14(1)$	$-0.01(2)$	$-0.08(2)$
458	$E2$	$0.21(6)$	$-0.03(8)$	0.0
480	$M1$	$-0.22(5)$	$0.06(7)$	$-0.20(9)$
543	$E1$	$-0.18(4)$	$-0.02(5)$	0.0
548	$M1+E2$	$-0.33(3)$	$0.02(4)$	$-0.14(3)$
553	$E2$	$0.13(1)$	$-0.05(1)$	0.0
701	$M1+E2$	$-0.34(5)$	$0.00(6)$	$-0.15(5)$
713	$M2$	$0.14(2)$	$0.00(3)$	$0.03(5)$

The 458-keV ($17^+ \rightarrow 15^+$) transition is of pure $E2$ character while the 543-keV ($15^+ \rightarrow 14^-$) γ ray is a pure $E1$ transition. The attenuation of the former transition was measured

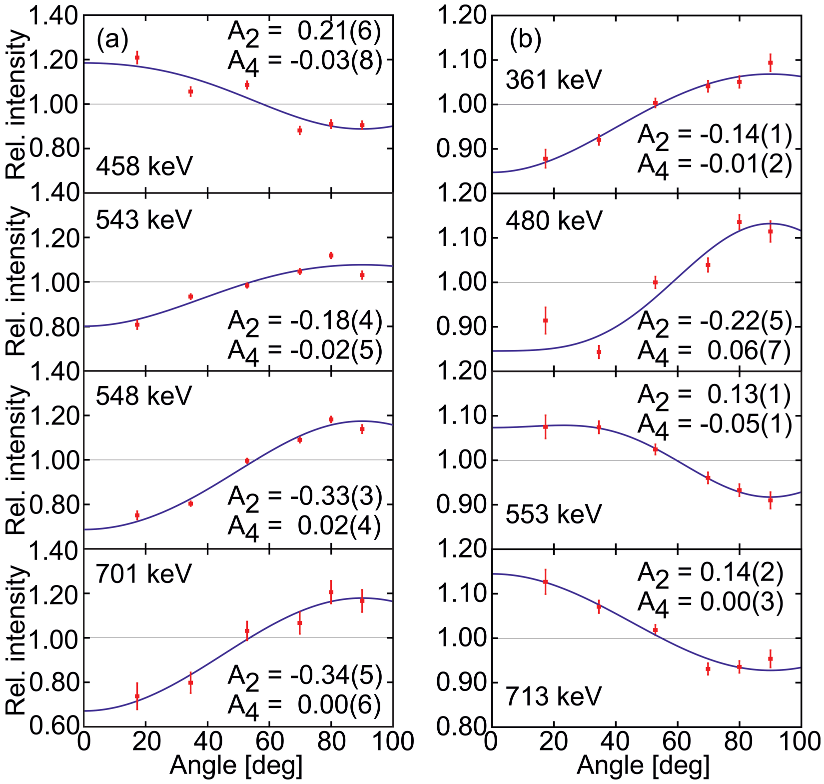

Figure 4.5. Angular distributions for known (a) and four new, strong γ rays (b) in ^{206}Bi. Measured points are shown together with the fitted curves and the corresponding A_2 and A_4 coefficients.

to be 0.54(15) and agrees with that inferred from the latter of 0.64(14). The attenuation of the A_2 coefficient resulting from this analysis is then 0.6(1) [69]. A similar analysis carried out for the A_4 coefficient shows that its attenuation is 0.2(6). These attenuation coefficients do not change significantly over the full cascade. Measured A_2 and A_4 coefficients together with deduced δ mixing ratios can be found in Table 4.3 for relevant transitions. The other two transitions on the left section of Fig. 4.5; i.e., the 548- ($14^- \to 13^-$) and 701- ($18^+ \to 17^+$) keV lines are of dominant $M1$ multipolarity. The A_2 coefficient results in the $E2/M1$ mixing ratio δ given in Table 4.3. A second solution of $\delta \sim -5$ would be possible for the measured A_2 value in both cases, but would give too large an A_4 coefficient: 0.11 for both the 548- and 701-keV transitions, clearly outside of the experimental errors. The results of the present analysis for the known 458-, 543-, 548- and 701-keV transitions in Fig. 4.5 are in agreement with the multipolarities assigned in the work of Lönnroth *et al.* [41]. From the newly established transitions, only the four with energies of 361, 480, 553, and 713 keV are sufficiently intense to obtain angular distributions (Fig. 4.5) and provide information on the associated multipolarities. The spin alignment gained in deep-inelastic collisions does not survive the $T_{1/2}$>2 µs isomer, but the analysis of the angular distributions of prompt γ rays from levels located below this 10170-keV long-lived state was possible due to the presence of strong prompt side feeding to the levels at 9233, 8520, 8159, and 7679 keV. The 361- and 480-keV lines are characterized by a negative A_2 value and, therefore, are of ΔJ=1 character.

The positive A_2 value for the 553-keV line indicates a stretched-$E2$ transition (note that $M2$ or $E3$ possibilities would be isomeric) whereas the 713-keV line below the 155-ns isomer must be of $M2$ or $E3$ character. Mixing ratios for the 361-, 480-, and 713-keV γ rays were derived from their A_2 coefficients, assuming that the 553-keV line is a pure $\Delta J{=}2$ $E2$ transition.

4.2 ^{205}Bi

The structure of ^{205}Bi was investigated with use of the data from the ^{208}Pb+^{208}Pb deep-inelastic reaction. The starting point for the search of new transitions was the level scheme established in previous studies by A. P. Byrne *et al.* [39] – it is marked in black in Fig 4.7. Those earlier studies shown the rather complex character of the level structure in both the lower and higher-energy parts. The structure lying below two isomers at 2139 and 2064 keV was fully confirmed by the analysis of the present data, although the transitions of 74 and 24 keV deexciting those isomers could not be observed. Similarly, the transitions of 58 and 85 keV from levels at 1168 and 881 keV could not be detected, but their presence could be deduced from the observed coincidence relationships. Also, higher excitations, including levels at 6453, 5942, and 5931 keV, were seen in the present studies, with exception of the 6718- and 5874-keV states. According to Byrne *et al.* those two states would deexcite via a 834-482-keV cascade, placed above the 5931-keV level. Unfortunately, this finding of Byrne *et al.* could not be confirmed here: only the 482-keV γ ray was identified but in the higher part of the level scheme (see further text).

The low-energy part of the ^{205}Bi level scheme is separated from the upper part by two close-lying isomers: the 100-ns isomer at 2064 keV and 220-ns one at 2139 keV. This arrangement significantly reduces the possibility of displaying higher-lying transition by gating on the lines below those isomers. To show higher lying transitions, double coincidence gates were set on the lines above the 2139-keV isomeric level. When the off-beam $\gamma\gamma\gamma$ cube was used with such gating, a series of peaks belonging to ^{205}Bi was displayed, indicating the existence of a new isomeric state at quite high excitation energy. The sum spectrum produced by gating on every pair of transitions: 516, 600, 641 keV is shown in Fig 4.6(a). The new transitions, following the decay of the high-lying isomer, are marked with red color. One can easily notice several intense γ rays belonging probably to the main branch of decay as well as other, weaker transitions.

In order to locate new levels by using information about new γ rays, the gates were set in the off-beam coincidence cube on the strongest, previously known transitions, that is 516, 524, 600, and 641 keV, as well as on the higher-lying lines. Many off-beam coincidence spectra were constructed this way – a representative example is shown in the Fig. 4.6(b). Out of newly displayed γ rays which certainly belong to ^{205}Bi and follow the decay of a new isomer, the strongest were lines at 295, 385, 482, 1145, 1272, and 2444 keV.

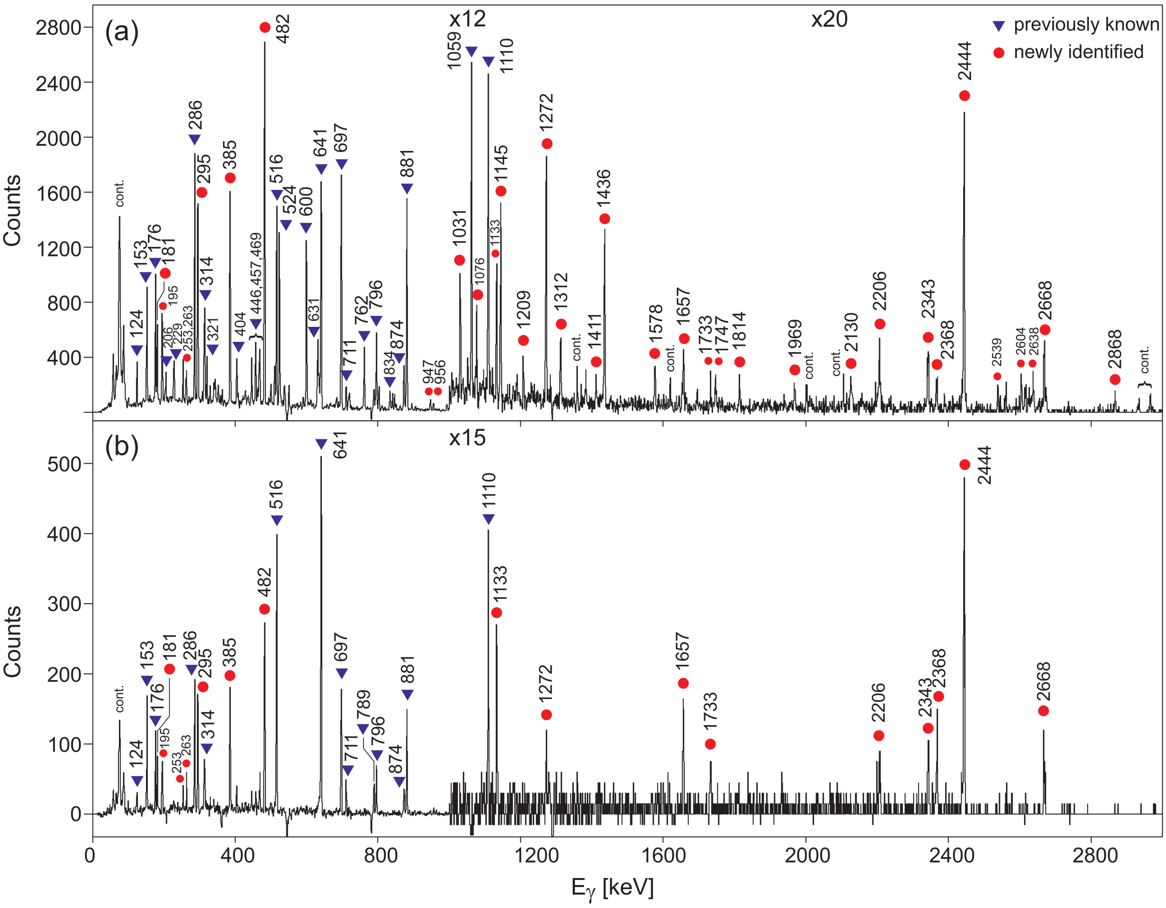

Figure 4.6. Representative off-beam coincidence spectra of ^{205}Bi: (a) sum spectrum double-gated on every pair of transitions at 614, 600, and 516 keV, (b) spectrum gated on the 524- and 600-keV transitions.

Table 4.4. Information on levels and transitions in ^{205}Bi from the present experiment.

E_i (keV)	J_i^π	E_f (keV)	J_f^π	E_γ (keV)	I_d	I_p	$\left(\frac{I_\mathrm{p}}{I_\mathrm{d}}\right)$
796	$11/2^-$	0	$9/2^-$	795.9(1)^{a}	27(1)	27(3)	0.99(13)
881	$13/2^-$	796	$11/2^-$	(85)^{a}	^{b}	^{b}	
		0	$9/2^-$	881.4(1)^{a}	61(2)	65(3)	1.05(6)
1110	$13/2^-$	796	$11/2^-$	313.9(1)^{a}	19(1)	20(2)	1.02(11)
		0	$9/2^-$	1109.9(1)^{a}	12(1)	12(1)	0.96(18)
1168	$15/2^-$	1110	$13/2^-$	(58)^{a}	^{b}	^{b}	
		881	$13/2^-$	286.3(1)^{a}	38(2)	38(2)	1.00(3)
1310	$(13/2^-)$	881	$13/2^-$	428.7(1)^{a}	3(1)	^{b}	
1344	$17/2^-$	1168	$15/2^-$	176.2(1)^{a}	22(1)	20(1)	0.89(6)
		881	$13/2^-$	462.4(2)^{a}	3(1)	^{b}	
1572	$(17/2^-)$	1344	$17/2^-$	228.2(2)^{a}	3(1)	^{b}	
		1168	$15/2^-$	404.4(2)^{a}	8(1)	7(1)	0.80(14)
1701	$15/2^-$	1168	$15/2^-$	533.4(2)^{a}	<1	^{b}	

Table 4.4 – continued from previous page

E_{i} (keV)	J_{i}^{π}	E_{f} (keV)	J_{f}^{π}	E_{γ} (keV)	I_{d}	I_{p}	$\left(\frac{I_{\mathrm{p}}}{I_{\mathrm{d}}}\right)$
		1110	$13/2^-$	591.2(2)[a]	3(1)	[b]	
1838	$15/2^-$	1344	$17/2^-$	527.8(1)[a]	3(1)	[b]	
2041	$17/2^+$	1838	$15/2^-$	203.4(1)[a]	1(1)	[b]	
		1701	$15/2^-$	340.1(2)[a]	5(1)	[b]	
		1572	$(17/2^-)$	469.0(1)[a]	12(1)	7(1)	0.58(10)
		1344	$17/2^-$	697.4(2)[a]	64(2)	32(2)	0.50(2)
		1168	$15/2^-$	873.5(1)[a]	15(1)	8(1)	0.53(8)
2064	$21/2^+$	2041	$17/2^+$	(24)[a]	[b]	[b]	
		1344	$17/2^-$	720.3(2)[a]	3(1)	[b]	
2139	$25/2^+$	2064	$21/2^+$	(74)[a]	[b]	[b]	
2779	$27/2^+$	2139	$25/2^+$	640.9(1)[a]	95(7)	95(5)	1.00(8)
3198	$27/2^+$	2139	$25/2^+$	1059.1(3)[a]	5(1)	[b]	
3200	$29/2^+$	2779	$27/2^+$	420.4(2)[a]	6(1)	5(1)	0.97(25)
3379	$29/2^-$	3198	$27/2^+$	181.8(2)[a]	6(2)	[b]	
		2779	$27/2^+$	599.8(1)[a]	89(4)	92(4)	1.03(5)
3895	$31/2^-$	3379	$29/2^-$	516.1(1)[a]	77(3)	62(2)	0.81(4)
3927	$(31/2^-)$	3895	$31/2^-$	(32)	[b]	[b]	
4020	$33/2^-$	3895	$31/2^-$	124.1(2)[a]	12(3)	6(1)	0.68(11)
		3379	$29/2^-$	640.7(4)	14(3)	11(2)	0.84(30)
4172	$35/2^-$	4020	$33/2^-$	152.5(1)[a]	12(2)	10(2)	0.77(15)
4180	$31/2^+$	3200	$29/2^+$	980.4(2)[a]	5(1)	3(1)	0.57(13)
4651	$35/2^-$	4020	$33/2^-$	631.2(1)[a]	12(2)	9(2)	0.80(17)
4696	$37/2^-$	4172	$35/2^-$	523.6(1)[a]	21(2)	13(1)	0.60(6)
4934	$37/2^-$	4172	$35/2^-$	761.8(1)[a]	13(2)	8(1)	0.73(6)
4958	$33/2^+$	4180	$31/2^+$	778.0(2)[a]	5(1)	[b]	
		3927	$31/2^-$	1030.8(2)	3(1)	[b]	
		3895	$31/2^-$	1062.6(1)[a]	8(1)	[b]	
5164	$35/2^+$	4958	$33/2^+$	206.0(2)[a]	5(1)	[b]	
		4020	$33/2^-$	1144.5(2)	7(1)	4(1)	0.62(9)
5249	$(37/2^-)$	4172	$35/2^-$	1077.2(3)	2(1)	[b]	
5392	$(37/2^+)$	5164	$35/2^+$	228.3(2)[a]	6(1)	[b]	
5407	$(39/2^-)$	4696	$37/2^-$	710.9(2)[a]	3(1)	[b]	
5485	$37/2^+$	5164	$35/2^+$	320.6(1)[a]	6(1)	[b]	
		4934	$37/2^-$	550.5(1)[a]	3(1)	[b]	
		4696	$37/2^-$	789.2(1)[a]	3(1)	2(1)	0.61(8)
		4651	$35/2^-$	834.1(2)[a]	3(1)	[b]	
		4172	$35/2^-$	1312.4(2)	2(1)	[b]	
5598	$(37/2^+)$	4651	$35/2^-$	947.3(2)	2(1)	[b]	

Table 4.4 – continued from previous page

E_i (keV)	J_i^π	E_f (keV)	J_f^π	E_γ (keV)	I_d	I_p	$\left(\frac{I_\mathrm{p}}{I_\mathrm{d}}\right)$
		4020	$33/2^-$	1578.1(3)	<1	[b]	
5652	$(39/2^-)$	4934	$37/2^-$	717.9(3)	2(1)	[b]	
5704	$(39/2^+)$	5598	$(37/2^+)$	105.2(2)	<1	[b]	
		5164	$35/2^+$	539.5(2)	2(1)	[b]	
		4651	$35/2^-$	1052.3(3)	<1	[b]	
5931	$(39/2^+)$	5485	$37/2^+$	446.1(1)[a]	4(1)	[b]	
5942	$(41/2^+)$	5931	$(39/2^+)$	(11)	[b]	[b]	
		5485	$37/2^+$	457.3(1)[a]	14(3)	10(1)	0.69(10)
6453	$(43/2^+)$	5942	$(41/2^+)$	510.8(2)[a]	13(2)	[b]	
6711	$(41/2^+)$	4172	$35/2^-$	2538.8(3)	<1	[b]	
6777	$(41/2^+)$	4172	$35/2^-$	2604.4(3)	<1	[b]	
6809	$(41/2^+)$	4172	$35/2^-$	2636.9(4)	<1	[b]	
6846	$(41/2^+)$	4172	$35/2^-$	2673.5(4)	<1	[b]	
6903	$(41/2^+)$	4934	$37/2^-$	1969.2(2)	3(1)	[b]	
		4696	$37/2^-$	2207.5(2)	3(1)	[b]	
7039	$(41/2^+)$	4934	$37/2^-$	2104.2(1)	<1	[b]	
		4696	$37/2^-$	2342.9(2)	2(1)	[b]	
		4172	$35/2^-$	2867.6(3)	<1	[b]	
7063	$(43/2^+)$	7039	$(41/2^+)$	(24)	[b]	[b]	
		6903	$(41/2^+)$	160.5(2)	2(1)	[b]	
		5942	$(41/2^+)$	1121.1(3)	<1	[b]	
		5931	$(39/2^+)$	1132.7(2)	4(1)	[b]	
		5652	$(39/2^-)$	1411.2(2)	<1	[b]	
		5407	$(39/2^-)$	1656.6(2)	3(1)	[b]	
		5249	$(37/2^-)$	1813.9(3)	<1	[b]	
		4934	$37/2^-$	2130.0(4)	<1	[b]	
		4696	$37/2^-$	2367.8(2)	<1	[b]	
7140	$(43/2^+)$	7039	$(41/2^+)$	(100)	[b]	[b]	
		6846	$(41/2^+)$	293.9(5)	<1	[b]	
		6809	$(41/2^+)$	330.0(2)	<1	[b]	
		6777	$(41/2^+)$	363.1(3)	<1	[b]	
		6711	$(41/2^+)$	428.6(4)	<1	[b]	
		5942	$(41/2^+)$	1208.5(2)	<1	[b]	
		5704	$(39/2^+)$	1435.8(1)	7(1)	[b]	
		5407	$(39/2^-)$	1733.0(2)	<1	[b]	
		5249	$(37/2^-)$	1747.0(3)	2(1)	[b]	
		4934	$37/2^-$	2205.6(3)	2(1)	[b]	
		4696	$37/2^-$	2443.6(2)	10(1)	3(2)	0.25(20)

Table 4.4 – continued from previous page

E_i (keV)	J_i^π	E_f (keV)	J_f^π	E_γ (keV)	I_d	I_p	$\left(\frac{I_\mathrm{p}}{I_\mathrm{d}}\right)$
7214	$(43/2^+)$	7063	$(43/2^+)$	151.2(2)	8(3)	[b]	
		5942	$(41/2^+)$	1272.1(1)	10(1)	4(1)	0.44(10)
7364	$(43/2^+)$	4696	$37/2^-$	2668.1(2)	2(1)	1(1)	0.44(40)
7409	$(45/2^+)$	7214	$(43/2^+)$	194.7(1)	13(2)	5(2)	0.37(11)
		6453	$(43/2^+)$	956.0(3)	5(1)	[b]	
7590	$(47/2^+)$	7409	$(45/2^+)$	181.1(2)	11(2)	2(1)	0.19(6)
7622	$(45/2^-)$	7140	$(43/2^+)$	482.1(1)	59(3)	9(1)	0.16(5)
7627	[c]	7364	$(43/2^+)$	263.2(2)	4(1)	[b]	
7726	[c]	7627	[c]	99.0(3)	3(1)	[b]	
7916	$(49/2^-)$	7622	$(45/2^-)$	294.9(1)	32(2)	4(1)	0.12(5)
7975	$(51/2^-)$	7916	$(49/2^-)$	(59)	[b]	[b]	
		7590	$(47/2^+)$	385.4(1)	29(2)	2(1)	0.06(2)

[a] γ rays seen also in Ref. [39]

[b] line contaminated or intensity too weak to be determined

[c] the spin-parity value could not be assigned

The construction of the high-energy part of the ^{205}Bi level scheme started with identifying a set of mutually coincident γ rays with energies 385, 181, 195, and 1272 keV, feeding the 5942-keV level. This cascade provided the location of the states at 7214, 7409, 7622, and 7975 keV. Some uncertainty regarding the 181-keV transition, which is close in energy to the 182-keV γ ray depopulating the 3379-keV level, was clarified by using the coincidence with 600-keV line. The ordering of the transitions under discussion was based on the intensity pattern (prompt to delayed ratio) and the observation of parallel branches: 956 keV and 151-1133 keV. Further support for this arrangement came from the observation of 160-, 1121-, 1657-, 1814-keV lines connecting the 7063-keV state with previously known or newly found excitations. Similarly, the state at a 7140 keV energy was established thanks to many decay paths passing through it and involving the 100-, 294-, 330-, 363-, 429-, 1208-, 1435-, 1733-, 1747-, 2206-, and 2444-keV γ rays. Due to strong internal conversion, the line at 100 keV, supposingly feeding a level at 7040 keV, is very weak, but the placement of 7040-keV state was confirmed by two parallel branches: 2868 and 2343 keV. It should be noted, that the ordering of γ-ray pairs: 294-2674, 330-2637, 363-2604, 429-2539 is not certain, because, due to their weak intensity, it was not possible to calculate prompt to delayed intensity ratios. Their placement was done based on the comparison with shell-model calculations, which will be discussed in Sec. 5.2.

After the construction of a consistent level scheme for ^{205}Bi up to the 7140-keV excitation, two strong lines: 482 and 295 keV, observed in coincidence with all transitions deexciting the 7140-keV state, were placed above it, defining 7622- and 7916- keV levels. The line of 253 keV was observed to be parallel to the 295-keV transition. The cascade 295-482 keV defines a state

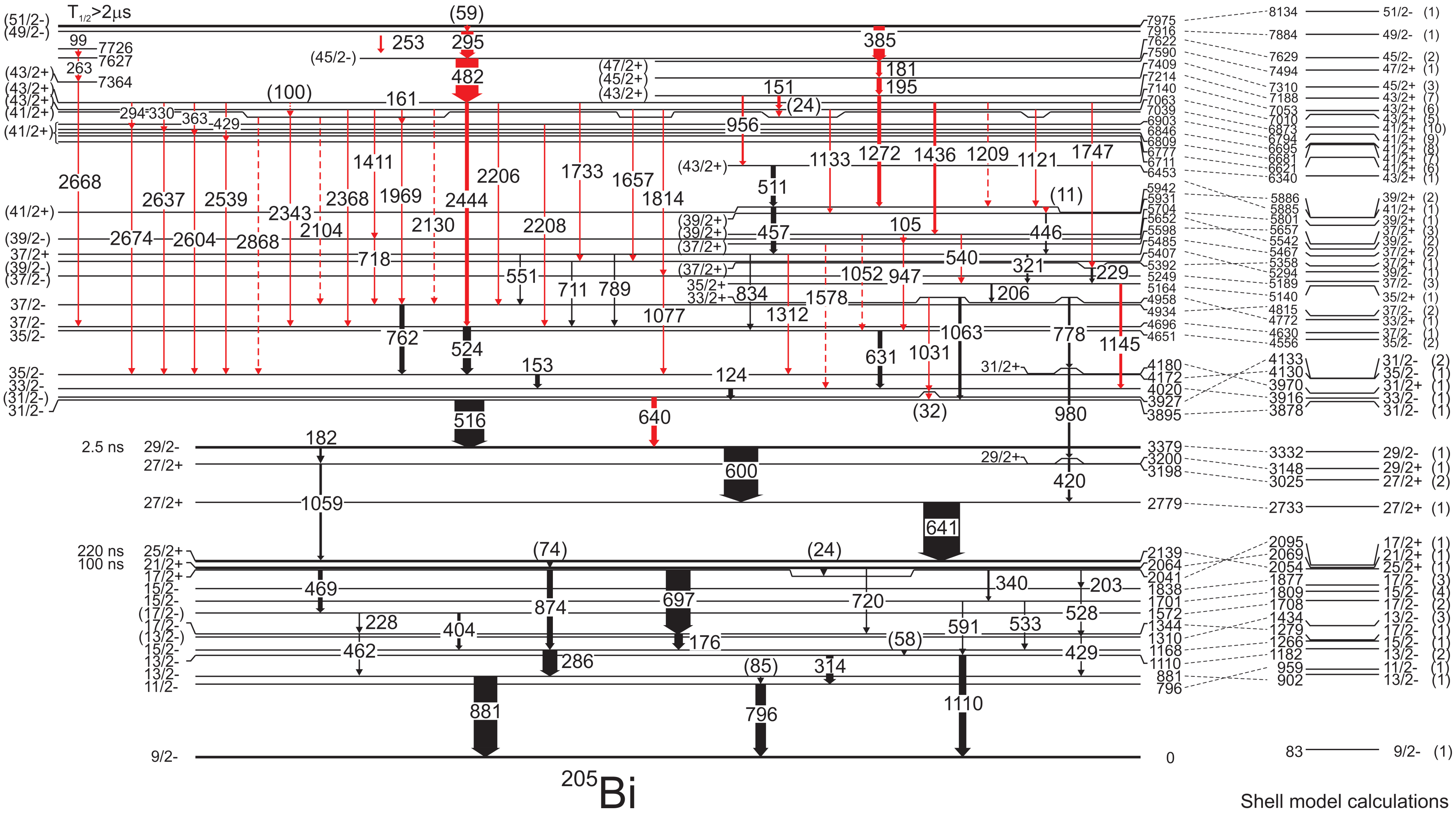

Figure 4.7. Level scheme of ^{205}Bi established in the present work. The newly found transitions are marked in red. The widths of the arrows indicates the observed intensities. The experimental levels are compared to the results of shell-model calculations (see Sec. 5.2)

at 7916 keV, thus an unobserved 59-keV γ ray probably connects this level with the highest excitation at 7975 keV. From the level energy differences, the existence of other unobserved low-energy lines was inferred, that is 11-, 24-, and 33-keV transitions depopulating states at 7063, 5942, and 3927, respectively.

From the fact that a 641-keV line is visible rather strongly in the spectrum gated on the pair of transitions 600-641 keV, but not in coincidence with 516- and 124-keV γ rays, one has to infer that it must be a doublet of transitions, one of which connects the 4020- and 3379-keV levels which was not assigned previously. Furthermore, the states at energies 4172, 4020, and 3895 keV were found to be fed by transitions at 1312, 1145, and 1031 keV, respectively. A level at 5704 keV was established by displaying two branches of its decay: a 105-947-keV cascade (the ordering was confirmed by observation of a 1578-keV γ ray going to the 4020-keV state) and a 540-keV line. The connection between levels at 5485 and 5407 keV by a 77-keV γ ray reported by Byrne *et al.* was not confirmed, because the transition of 711 keV could not be observed in coincidence with the 457- or 446-keV lines. Similarly, lines 417 and 463 keV, tentatively placed as feeding 2779- or 5164- and 5485-keV levels, respectively, in the mentioned work, could not be confirmed. One should note that, in addition to transitions placed in the level scheme, also a 634-keV γ ray was assigned to ^{205}Bi as parallel to the 295-482- and 385-181-195-keV cascades, but its exact placement could not be established.

The intensities of the transitions were calculated from double-gated off-beam coincidence spectra. For transitions lying below the two isomers, intensities were taken from the spectrum gated on the 600- and 641-keV γ rays feeding the $25/2^+$ isomer. They were normalized to the sum of the intensities of the 881-, 796-, and 1110-keV γ rays feeding the ground state, for which a value of 100 was assumed. Intensities above the 100- and 220-ns isomers were calculated separately: in the off-beam cube a gate was first set on the 697- and 881-keV lines and the intensities of transitions at 600, 420 and 1059 keV observed in this spectrum were normalized to 100. The intensities of the remaining strong lines were also taken from this spectrum. For less intense lines, gating on a specific set of γ rays was chosen to obtain their intensities relative to stronger transitions. By summing the intensities of parallel branches one may notice that in the middle region of the scheme, below the 6711-kev state, up to 40% of the intensity is missing. Similarly to the case of ^{206}Bi described in previous section, this observation suggests that (a) some decay branches remain unobserved due to their weak intensity, and that (b) the level structure in this region is even more complex than established in the present study.

More detailed analysis of the intensity balance for lines lying at the top of the level scheme was performed to obtain information on the associated conversion coefficients. Due to the very complex structure of the scheme in its medium part, the intensity balance for high-lying transitions relied on comparisons with the intensities of γ rays at the bottom of decaying cascades. For example, the intensity of 195-keV line extracted from a spectrum gated on 385- and 516-keV was compared to the sum of the intensities of the 600 and 1059-keV transitions. A similar procedure was applied to the 161- and 181-keV lines. Values of the conversion coefficients obtained for those four transitions agree, within the error, with

Table 4.5. Total conversion coefficients $\alpha_{\text{tot-exp}}$. The second column gives the measured delayed intensity, while the third provides the total intensity as expected from the decay scheme. A specific set of gates was applied to reduce the intensity uncertainties. Column 4 presents the total conversion coefficient deduced from the missing γ-ray intensities and column 5-7 the theoretical values for the different multipolarities ($E1$, $M1$, and $E2$ multipolarities were considered). The assigned values are marked by bold characters.

E_γ (keV)	I_γ	I_{tot}	$\alpha_{\text{tot-exp}}$	$E1$	$M1$	$E2$
161	2.0(3)	6.6(13)	2.32(84)	1.386E–01	**2.672E+00**	1.010E+00
181	10.0(8)	32.9(13)	1.99(27)	1.022E–01	**1.887E+00**	6.403E–01
195	13.0(15)	35.3(18)	1.71(36)	8.510E–02	**1.531E+00**	4.905E–01

theoretical coefficients for $M1$ multipolarity. The results are shown in Table 4.5. Since specific gates were used to obtain the intensities given in Table 4.5, these values cannot be calculated directly by using the values presented in Table 4.4. One should note, however, that the intensities I_γ presented in Table 4.5 were scaled to values from Table 4.4.

Only at rough estimation of the half-life of the isomer at 7975-keV excitation energy was possible. As in the case of ^{206}Bi, the time spectrum started by the RF signal of the accelerator and stopped by the detection of the 385-keV transition was constructed. Also, the coincidences between this line and other strong γ rays in the decay were required. As this time spectrum covers effectively only a 400-ns range, the $T_{1/2}$ value for this long-lived state could be estimated to be larger than 2 µs.

The information on all transitions and energy levels deduced in the present work has been summarized in Table 4.4.

4.3 ^{210}Bi

4.3.1 Yrast states – Argonne data

In ^{210}Bi, the existing information about the structure above the α-decaying isomer at 271 keV shown in Fig. 4.9 was a starting point in a search for high-spin states. The spectra of prompt and delayed γ rays were analyzed by requiring coincidence relationships with the known ^{210}Bi yrast transitions. Mainly the ^{208}Pb+^{208}Pb data were used for the analysis described below.

As a first step, by using the off-beam cube, double gating on every pair of lines at 151, 398, 653, 744, 1252, 1403, and 1514 keV was made. The resulting summed spectrum, displayed in Fig. 4.8(a), showed new transitions belonging to cascades deexciting an unknown isomeric state at higher excitation energy. After the first identification, the attempt was made to delineate a complete level structure under the isomer. The detailed gating was done, but unfortunately the exact placement of this isomer could not be determined. A reason for this difficulty could be the presence in the deexcitation cascades of low-energy transitions which, due to their high internal conversion and low detection efficiency, remained unobserved.

Further analysis involved also the in-beam γ-ray coincidence relationships. The detailed investigation of spectra double gated on the pairs of transitions (see Fig 4.8(b) for a represen-

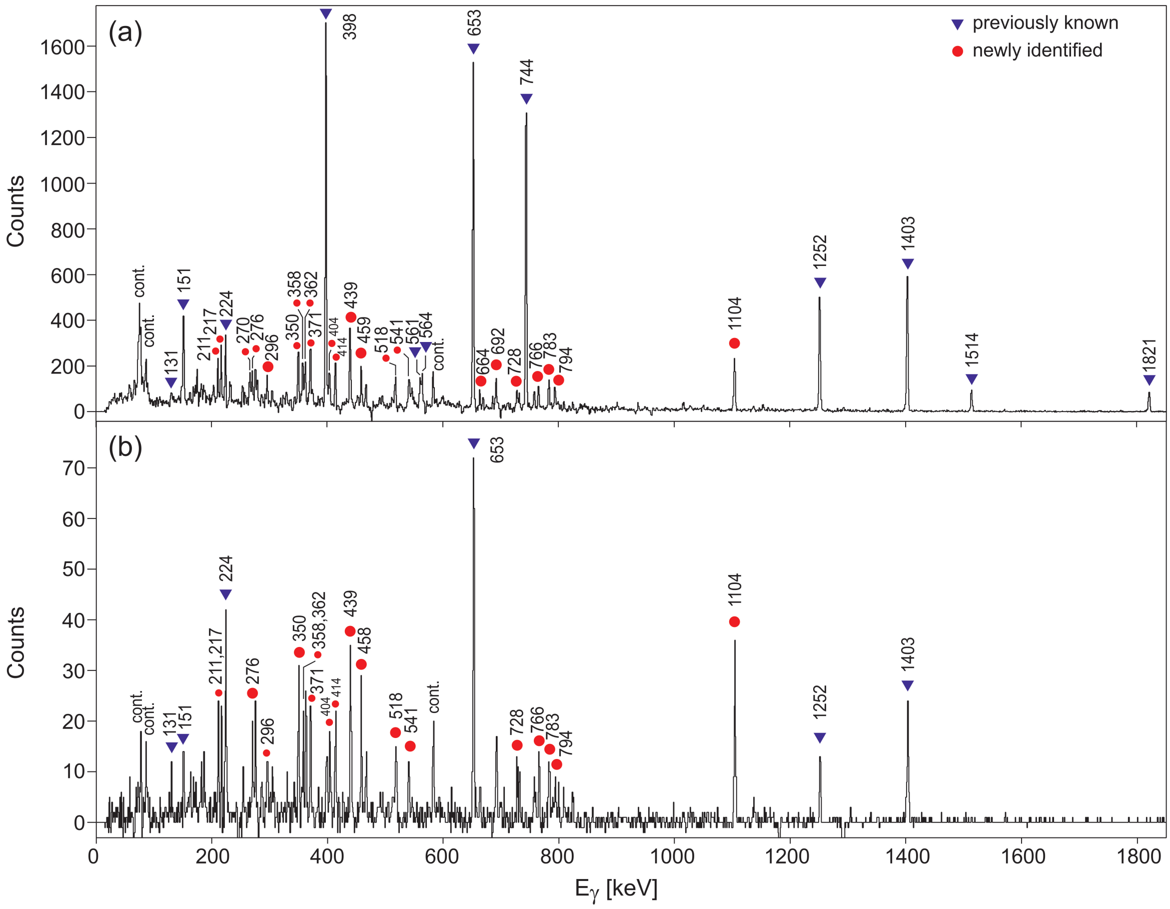

Figure 4.8. Representative off-beam coincidence spectra of ^{210}Bi: (a) sum spectrum double-gated on every pair of transitions at 151, 398, 653, 744, 1252, 1403, and 1514 keV, (b) spectrum gated on the 398- and 1514-keV transitions.

tative example) confirmed the level scheme obtained in previous studies [45] and resulted in the addition of new prompt lines. In the level scheme of ^{210}Bi presented in Fig. 4.9 the black part shows the yrast structure identified so far, on top of which new findings are shown. The state at 4594 keV is fed by the cascade consisting of 371-, 217-, 296-, and 518-keV γ rays, which established levels at 4965, 5181, 5478, and 5996 keV. The parallel branches, 783- and 663-keV transitions, populating the 4965- and 5181-keV levels were used to locate 5748- and 5845-keV excitations, respectively. The ordering of these γ rays was determined by analyzing their in-beam to off-beam intensity ratio, which should decrease monotonically with excitation energy. In particular, the existence of a 4085-keV state was confirmed by the observation of a parallel 1361-keV branch connecting it with the level at 2725 keV. The lines present in the off-beam spectra double gated on strong lines in ^{210}Bi which were also identified as present in cascades originating from an unknown isomer in ^{210}Bi are: 211, 217, 270, 276, 296, 350, 358, 362, 404, 414, 439, 459, 518, 541, 692, 728, 766, 794, 1104 keV. They could not be placed in the level scheme, but their energies and off-beam intensities were determined and are reported in Table 4.6. All the intensities were normalized to the sum of the intensities of the 653- and 1050-keV transitions, which was set as 100.

Table 4.6. Information on levels and transitions in ^{210}Bi from the present studies.

E_{i} (keV)	J^{π}_{i}	E_{f} (keV)	J^{π}_{f}	E_{γ} (keV)	I_{d}	I_{p}	$\left(\frac{I_{\mathrm{p}}}{I_{\mathrm{d}}}\right)$
669	10^-	271	9^-	397.9(1)[a]	76(3)	76(1)	1.00(4)
1322	11^+	669	10^-	652.6(1)[a]	91(4)	89(1)	0.97(3)
		271	9^-	1050.3(2)[a]	9(1)	9(1)	1.02(7)
1473	12^+	1322	11^+	151.3(2)[a]	13(2)	12(1)	0.94(6)
2725	14^-	1473	12^+	1251.9(1)[a]	31(2)	19(1)	0.60(3)
		1322	11^+	1403.2(1)[a]	45(3)	29(1)	0.64(3)
3294	(13^+)	1473	12^+	1821.1(2)[a]	17(1)	7(1)	0.40(3)
3469	(15^+)	3294	(13^+)	174.7(2)[a]	10(1)	2(1)	0.23(2)
		2725	14^-	744.0(1)[a]	68(3)	17(1)	0.26(2)
4030	(16^+)	3469	(15^+)	561.1(2)[a]	3(1)	8(1)	2.7(7)
4085	(14^-)	2725	14^-	1360.6(5)	<1	<1	
		1473	12^+	2612.5(3)[a]	2(1)	5(1)	2.7(6)
4239	(15^-)	4085	(14^-)	154.2(8)[a]	<1	<1	
		2725	14^-	1514.3(1)[a]	8(1)	19(1)	2.3(2)
4463	(16^-)	4239	(15^-)	224.0(2)[a]	6(1)	10(1)	2.1(2)
4594	(17^-)	4463	(16^-)	130.6(2)[a]	2(1)	3(1)	1.5(4)
		4030	(16^+)	564.1(2)[a]	3(1)	7(1)	2.0(5)
4965	[c]	4594	(17^-)	370.8(1)	6(1)	8(1)	1.4(2)
5181	[c]	4965	[c]	216.6(1)	3(1)	4(1)	1.2(2)
5478	[c]	5181	[c]	296.4(1)	2(1)	2(1)	1.1(2)
5748	(20^-)	4965	[c]	783.5(1)	4(1)	5(1)	1.1(2)
5845	[c]	5183	[c]	664.0(3)	2(1)	2(1)	0.95(18)
5996	[c]	5478	[c]	518.2(2)	3(1)	2(1)	0.66(21)
				211.0(2)	3(1)		
				270.3(2)	3(1)		
				275.6(1)	2(1)		
				296.4(2)	1(1)		
				349.9(1)	5(1)		
				358.0(1)	3(1)		
				362.2(1)	4(1)		
				403.7(2)	4(1)		
				413.8(2)	3(1)		
				439.4(1)	7(1)		
				459.1(3)	2(1)		
				541.2(2)	3(1)		
				692.1(1)	4(1)		
				727.8(3)	3(1)		
				765.6(2)	2(1)		
				793.9(2)	3(1)		
				1104.3(1)	8(1)		

[a] γ rays seen also in Ref. [45]

[b] intensity too weak to be determined

[c] the spin-parity value could not be assigned

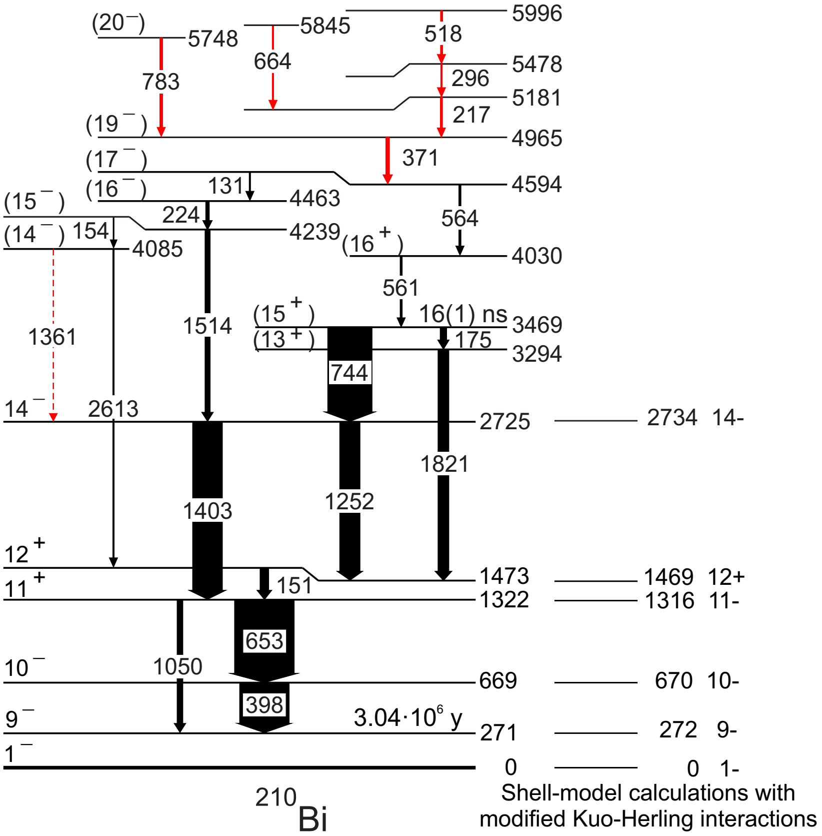

Figure 4.9. Level scheme of ^{210}Bi established in the present work. The newly found transitions are marked in red. The widths of the arrows indicates the observed intensities. The experimental levels are compared to the results of shell-model calculations (see Sec. 5.3).

An analysis of conversion coefficients for low-energy lines was performed using intensity balance. For example, the intensity of the 398-keV line was compared to the intensity of the 653-keV line (which is an $E1$, weakly converted, transition with $\alpha_{tot} = 0.006$) in the off-beam sum spectrum gated on 1252-1514-, 744-1252-, 1403-1514-, 744-1430-keV pairs of γ rays. The obtained coefficient of 0.19(5) indicates a $M1 + E2$ character for the 398-keV line. A similar analysis for the line at 175 keV yielded $\alpha_{tot} = 0.7(1)$ which confirmed its $E2$ multipolarity. Total conversion coefficients obtained for the 131-, 151-, and 224-keV transitions, e.g.: 4.78(48), 3.17(28), and 0.98(9), respectively, allowed to deduce their $M1$ multipolarity. This analysis was also carried out for the 154-keV line deexciting the 4239-keV level, but due to its weak intensity and to a close-lying 151-keV transition, only a very rough value could be extracted: 5(2), which can be associated within errors with an $M1$ transition. All the mentioned results regarding conversion coefficients of selected transitions in ^{210}Bi, together with theoretical estimates are summarized in Table 4.7.

The analysis of prompt-delayed matrices and cubes confirmed the existence of the short-lived isomeric state at 3469 keV. Its half-life could be determined from a spectrum of time differences between the detection time of the 561- and 564-keV transitions with respect to the 653-, 744-, 1252-, 1403-keV γ rays below the isomer. The resulting value of 16(1) ns is in agreement with $T_{1/2}$=14(5) ns reported in [45].

Table 4.7. Total conversion coefficients $\alpha_{\text{tot-exp}}$. The second column gives the measured delayed intensity, while the third provides the total intensity as expected from the decay scheme. A specific set of gates was applied to reduce the intensity uncertainties. Column 4 presents the total conversion coefficient deduced from the missing γ-ray intensities and column 5-7 the theoretical values for the different multipolarities ($E1$, $M1$, and $E2$ multipolarities were considered). The assigned values are marked by bold characters.

E_γ (keV)	I_γ	I_{tot}	$\alpha_{\text{tot-exp}}$	$E1$	$M1$	$E2$
131	1.85(21)	10.7(6)	4.78(48)	2.279E–01	**4.714E+00**	2.200E+00
151	13.1(5)	54.6(28)	3.17(28)	1.601E–01	**3.148E+00**	1.259E+00
154	0.33(6)	2.00(28)	5(2)	1.549E–01	**3.033E+00**	1.197E+00
175	9.7(3)	16.5(5)	0.7(1)	1.111E–01	2.075E+00	**7.239E–01**
224	5.4(3)	10.7(6)	0.98(9)	6.074E–02	**1.039E+00**	3.044E–01
398	76.4(20)	90.9(24)	0.19(5)	1.611E–02	**2.156E–01**	5.449E–02

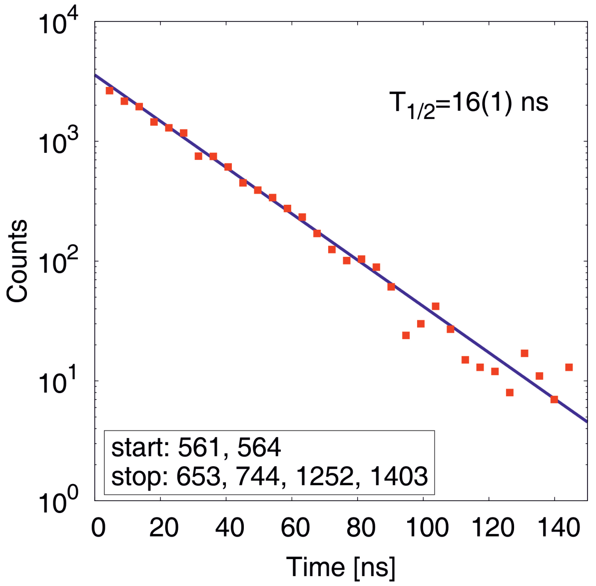

Figure 4.10. Summed time distribution between the 561- and 564-keV γ rays, and any of the 653-, 744-, 1252-, or 1403-keV lines.

Table 4.8. The measured angular-distribution coefficients A_2 and A_4, assigned multipolarity and the ensuing mixing ratios δ for transitions in ^{210}Bi.

E_γ (keV)	Multipolarity	A_2	A_4	δ
151	$M1+E2$	0.06(10)	0.00(13)	0.19^{+10}_{-8}
224	$M1(+E2)$	−0.19(4)	0.01(6)	−0.02(4)
371	$E2$	0.23(6)	0.08(9)	0.00(9)
398	$M1+E2$	0.01(6)	0.00(8)	0.15(5)
653	$E1$	−0.20(3)	0.03(3)	0.0
744	$E1$	−0.20(3)	−0.01(4)	−0.03(4)
783	$(M1+E2)$	−0.24(2)	0.13(2)	-7.5^{+17}_{-31}
1050	$M2(+E3)$	0.32(5)	0.11(6)	0.09^{+11}_{-9}
1252	$M2+E3$	0.38(2)	0.04(3)	0.19^{+11}_{-9}
1403	$E3$	0.41(1)	0.04(1)	0.0
1514	$M1+E2$	0.49(2)	0.11(2)	1.10^{+76}_{-46}
1821	$M1+E2$	−0.68(5)	0.14(7)	-1.35^{+43}_{-74}
2613	$M2(+E3)$	0.28(5)	0.00(6)	0.05^{+10}_{-8}

Only a rough estimate of the half-life of the new isomer could be obtained as 10÷100 ns. The spectrum of time differences between γ rays could not be constructed for this case, because of the lack of observed transitions above the isomer. By summing the energies of mutually coincident transitions, the energy of the new isomeric excitation in ^{210}Bi could be estimated as >10 MeV.

To obtain information on multipolarities of transitions in ^{210}Bi, the angular distribution analysis of γ rays was performed. This method was applied for the first time for the transitions in this nucleus. As shown above, the normalized intensities of γ rays in specific rings of the Gammasphere array were used to construct the distributions. In order to gain more statistics, the γ-γ matrices were constructed for various rings. The spectra were rather clean, because most of the transitions of interest were not strongly contaminated. Only for specific cases, where the background could influence significantly the result, the $\gamma\gamma\gamma$-cubes were used to obtain cleaner spectra. Final spectra for different angles were produced by summing the histograms gated on 398-, 653-, 744-, 1252-, 1403-, 1514-keV transitions. Angular distributions obtained in this way are presented in Fig. 4.11.

The first step in the interpretation of the results was the assumption (based on the previous comparisons with shell-model calculations) that the 653- ($11^+ \to 10^-$) and 1403-keV ($14^- \to 11^+$) γ rays are of pure $E1$ and $E3$ character, respectively. As the angular distribution for these lines were obtained, the attenuation of the A_2 coefficients, 0.70(11) and 0.59(1), could be extracted. The α_2 value resulting from this analysis is 0.65(9), which is in agreement with the general relationship $\alpha_2(J)$ calculated for ^{208}Pb+^{208}Pb data and presented in Fig. 3.5 ($\alpha_2 = 0.6(1)$ for $J \approx 23/2$ and does not change significantly at higher spins). This determines also the attenuation of the A_4 coefficient: α_4=0.2(1) [79], which was confirmed by the experimental estimation: 0.1(1).

All γ-ray angular distributions obtained for the ^{210}Bi nucleus are presented in Fig. 4.11. Almost isotropic functions for the transitions: 398- ($10^- \to 9^-$) and 151-keV ($12^+ \to 11^+$)

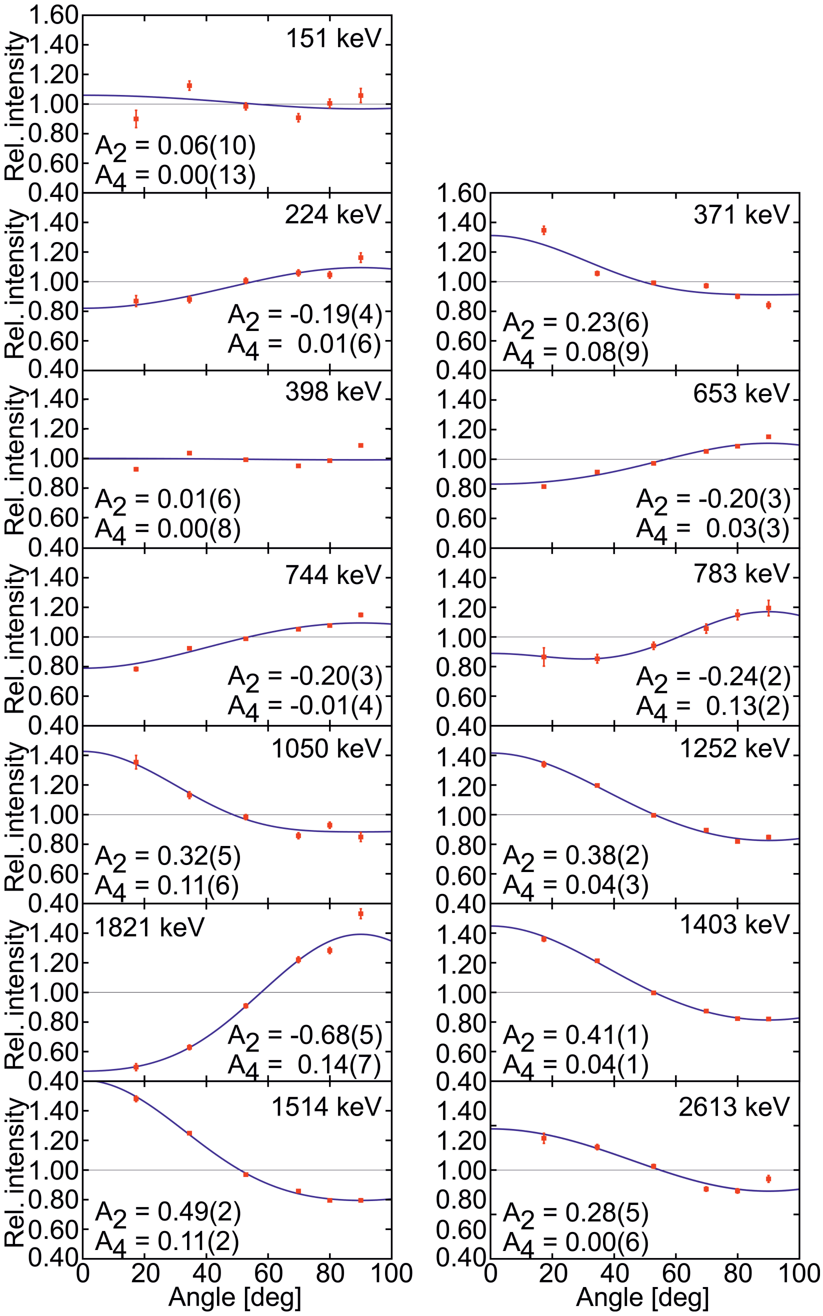

Figure 4.11. Angular distributions for strong γ rays in ^{210}Bi. Measured points are shown together with the fitted curves and the corresponding A_2 and A_4 coefficients.

indicate their mixed $M1 + E2$ character. The $E2/M1$ mixing ratios δ extracted from A_2 coefficients are presented in Table 4.8. The results of the present analysis for the known 151-, 224-, 398-, 653-, 744-, 1050-, 1252-, 1403-, and 1821-keV transitions are in agreement with the multipolarities assigned in the work of B. Fornal [45]. The 744-keV transition is of pure $E1$ character, while 224-keV line, having $\Delta J{=}1$ and taking into account the value of its conversion coefficient, must be a $M1(+E2)$ γ ray. The 1050- and 1252-keV lines are, as it was predicted, of $M2$ type, but probably mixed with an $E3$ component. The 2613-keV transition is characterized by $A_2 = 0.28(4)$ which indicates its $\Delta J{=}2$ character, which does not confirm the previous $E3$ assignment. As a small mixing is possible, the $M2(+E3)$ multipolarity was assigned to it, although one cannot completely rule out the stretched $E2$ possibility (an alternative possibility of $E2(+M3)$ was excluded because it would be associated with a long lifetime and this was not observed). Positive and large values of $A_2 = 0.49(2)$ and $A_4 = 0.11(2)$ for the 1514-keV γ ray suggest mixing. The following types of multipoles may be considered in this case: $E1 + M2$, $M1 + E2$, and $M2 + E3$. Taking into account the multipolarities $M1$ and $E2$ of the transitions in the parallel 154-2613-keV cascade, the most probable scenario would be $M1{+}E2$ mixing (similar to the case of 1821-keV line).

Out of the newly established transitions, only the 371- and 783-keV γ rays are sufficiently intense to obtain their angular distribution. The positive A_2 value for the 371-keV line indicates a stretched-$E2$ transition. The large A_4 value obtained for the 783-keV γ ray suggests strong mixing of $\Delta J{=}2$, thus $(M1{+}E2)$ multipolarity was assigned to this transition (note, that $E1{+}M2$ would lead to an isomer). Measured A_2 and A_4 coefficients together with deduced δ mixing ratios for the relevant transitions can be found in Table 4.8.

4.3.2 Low-spin states – ILL data

Searching for low-spin states in ^{210}Bi populated in a cold-neutron capture reaction was also performed with use of the γ-coincidence technique. Following the neutron capture on a ^{209}Bi target, a state at $\sim$4605 keV is populated in ^{210}Bi. The decay of this level proceeds through many paths feeding a large number of states. Many of these were already known from similar cold-neutron capture investigations [51], but those studies have never been performed with the discrete multi-coincidence γ spectroscopy technique employing modern detector arrays. Hence, the present investigation allows to study low-spin structure of ^{210}Bi in greater detail.

The building of the level structure started from producing spectra of γ rays coincident with the ones previously observed in the lower part of the scheme; i.e., the 320-keV ($2^- \rightarrow 1^-$) γ ray feeding the ground state or the 162-keV ($7^- \rightarrow 9^-$) transition populating a long-lived isomeric state. These histograms were generated by using the $\gamma\gamma$-matrix, but resulting spectra were very complex – they displayed a large amount of lines belonging to ^{210}Bi. Only at higher energies was the density of lines relatively low. For example, the two peaks at 4285 and 4171 keV, associated with transitions from the 4605-keV state to the first 2^- and 7^- levels at 320 and 433 keV, respectively, could be easily seen. However, in order to confirm the previous level scheme and to perform a search for new transitions, the $\gamma\gamma\gamma$-coincidence cube had to be used.

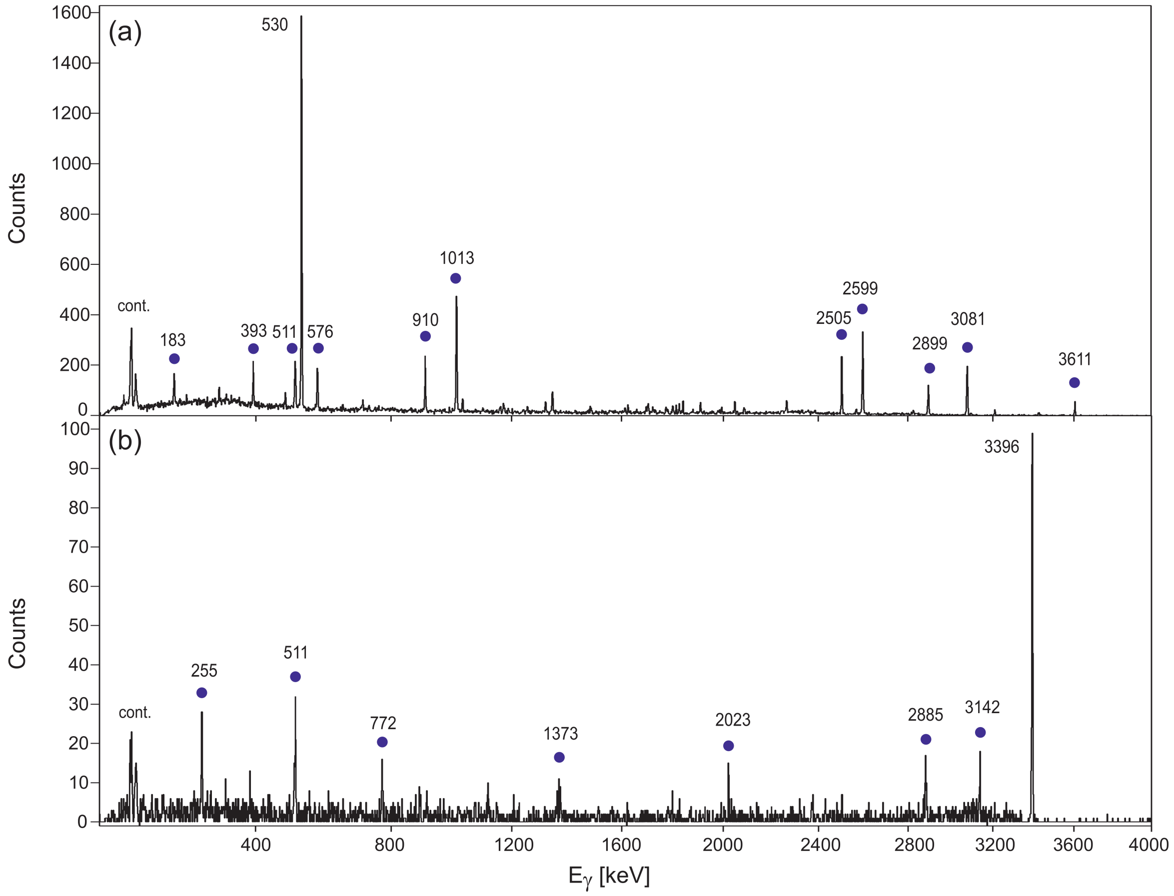

Figure 4.12. Representative coincidence spectra for ^{210}Bi: (a) spectrum double-gated on the pair of transitions at 320 and 674 keV, (b) spectrum double-gated on the 162- and 775-keV transitions.

The analysis involved inspection of many spectra gated on different combinations of γ rays. In particular, a search for coincident transitions energies that would sum up to 4605 keV (when feeding 320-keV state) or 4334 keV (when feeding 271-keV state) was performed (some transitions could, of course, be coincident with both 320- and 162-keV lines). The very complex level scheme resulting from this investigation is shown in Fig. A.1-4 and information on the observed transitions is also presented in Table 4.9. The investigations allowed to establish 54 branches of the decay from the neutron-capture state, of which 31 are newly observed. Twenty four new states populated mainly by primary γ rays were also located in the energy range of 1902-4221 keV. The energy of the state produced in thermal neutron capture was calculated from the sums of energies in different strong cascades. The value resulting from this analysis is 4605.2(1) keV.

An analysis of angular correlations of γ rays was carried out aimed at establishing what spin-parity value, 4^- or 5^-, is preferably produced after the neutron-capture reaction. To this end, angular correlation functions of γ rays were constructed with the help of three $\gamma\gamma$-matrices containing events with the detection of pairs of γ rays in the EXOGAM detectors located at average angles of 0°, 45°, and 90° with respect to each other. By using such matrices and gating on a transition, whose multipolarity is known, one can observe the anisotropic angular distribution of the second photon. From such a distribution one can infer the multipolarity of this second γ quantum and use it to assign spin-parity values to the nuclear states which are involved.

During the data analysis, at first, an angular correlation function was constructed for the pair of transitions 320-4257 keV. The latter one is a primary γ ray feeding the 3^- state at 348 keV. As the 320-keV γ ray is a pure $M1$ transition, the order of multipole of the 4257-keV photon could be extracted. The extracted coefficients, $A_2 = -0.08(2)$ and $A_4 = 0.02(3)$ indicate its ΔJ=2 nature, which suggest the $J^\pi = 5^-$ value for the neutron-capture state. The multipolarity of the 4101-keV transition, a primary γ ray feeding the 4^- state at 503 keV, was deduced from the correlation with the 320-keV γ ray as $E1$ or $M1$. Also, the measurements of the same 4101-keV line in coincidence with the stretched $E2$ 348-keV transition, feeding the ground state from level 3^-, pointed to its ΔJ=1 character. All these observations are consistent with an $M1$ multipolarity for the 4101-keV γ ray and with the $J^\pi = 5^-$ assignment for the neutron-capture state. Further support for this scenario comes from the 1337-2828-keV cascade, in which the first transition is of pure $E1$ character confirmed by its correlation with the 320-keV line. The 2828-keV primary transition, feeding the 6^+ state, was found to be of $\Delta J = 1$ character, which again is in line with a $J^\pi = 5^-$ spin-parity for the 4605-keV state. On the other hand, one should notice that some primary γ rays (i.e., 4285, 3633, 3430 keV) feed the 2^- states. Thus, the $J^\pi = 5^-$ value of neutron-capture state would not be possible, because such γ rays would be forbidden $M3$ transitions. In order to check this, another pair of lines was considered: a 409-keV (pure $M1$ $2^- \to 1^-$) transition and the 3633 keV primary γ ray leading to the 2^- state. The analysis yielded coefficients values $A_2 = -0.07(4)$ and $A_4 = 0.05(7)$. The resulting value ΔJ=2 suggests that this primary γ ray is of $E2$ character (as changing parity $M2$ would not be possible) and, as a consequence, the searched J^π value for the state at 4605 keV would be 4^-. This leads to the conclusion that two states with possible spin-parity values of 4^- and 5^- may well be populated after the neutron capture on the ^{209}Bi nucleus.

Values of the A_2 and A_4 coefficients established for transitions deexciting the neutron-binding state are presented in Table 4.10.

Table 4.9. Information on levels and transitions in ^{210}Bi from the present experiment.

E_i (keV)	J_i^π	E_f (keV)	J_f^π	E_γ (keV)
46	0^-	0	1^-	(46)
271	9^-	—	—	—
320	2^-	0	1^-	319.91(8)
348	3^-	320	2^-	(28)
		0	1^-	348.13(72)
434	7^-	271	9^-	162.49(3)
439	5^-	434	7^-	(6)
		348	3^-	91.35(94)
503	4^-	439	5^-	(64)

Table 4.9 – continued from previous page

E_i (keV)	J_i^π	E_f (keV)	J_f^π	E_γ (keV)
		348	3^-	155.09(12)
551	6^-	439	5^-	111.05(3)
		434	7^-	116.90(4)
563	1^-	320	2^-	243.87(19)
		46	0^-	516.76(3)
		0	1^-	563.37(2)
583	8^-	434	7^-	149.69(18)
		271	9^-	311.40(3)
916	8^-	434	7^-	482.26(5)
		271	9^-	644.62(3)
972	2^-	563	1^-	408.95(2)
		348	3^-	624.11(4)
		0	1^-	971.95(2)
993	3^+	503	4^-	491.00(5)
		348	3^-	645.96(2)
		320	2^-	674.10(7)
1175	2^-	503	4^-	672.67(11)
		348	3^-	827.36(8)
		320	2^-	855.57(5)
		0	1^-	1174.52(46)
1209	6^-	551	6^-	658.48(11)
		503	4^-	705.62(11)
		439	5^-	769.43(7)
		434	7^-	775.11(11)
1248	4^-	439	5^-	808.91(1)
		348	3^-	900.22(2)
1336	5^-	1209	6^-	(127)
		551	6^-	786.08(11)
		503	4^-	832.73(5)
		439	5^-	896.44(5)
1374	3^-	1248	4^-	(125)
		972	2^-	402.30(3)
		503	4^-	871.25(7)
1390	4^-	1175	2^-	215.12(3)
		503	4^-	887.21(5)
		439	5^-	950.82(3)
		348	3^-	1042.14(6)
		320	2^-	1070.39(24)
1464	5^-	1248	4^-	215.39(10)

Table 4.9 – continued from previous page

E_i (keV)	J^π_i	E_f (keV)	J^π_f	E_γ (keV)
		1209	6^-	254.79(6)
		551	6^-	913.08(4)
		503	4^-	960.37(13)
1524	4^+	993	3^+	529.89(1)
		503	4^-	1020.32(12)
		348	3^-	1175.26(3)
1707	5^+	1524	4^+	183.36(5)
		993	3^+	712.84(10)
		551	6^-	1156.50(4)
		503	4^-	1203.68(2)
		439	5^-	1267.30(10)
1777	6^+	551	6^-	1226.37(2)
		439	5^-	1337.19(7)
		434	7^-	1342.58(21)
1904	[a]	993	3^+	909.79(2)
		320	2^-	1583.74(8)
1981	7^-	1209	6^-	772.28(9)
		916	8^-	1064.69(3)
		583	8^-	1397.95(2)
		551	6^-	1430.31(2)
		434	7^-	1546.80(5)
		271	9^-	1708.99(7)
2007	[a]	1904	[a]	(103)
		1707	5^+	300.00(4)
		1524	4^+	483.12(6)
		1374	3^-	632.41(11)
		1248	4^-	758.71(9)
		993	3^+	1012.63(2)
		503	4^-	1503.44(7)
		439	5^-	1567.21(7)
		348	3^-	1658.84(2)
		320	2^-	(1687)
2034	[a]	551	6^-	1483.88(4)
		503	4^-	1531.11(8)
		439	5^-	1594.63(11)
		434	7^-	1600.36(13)
2081	(4^-)	503	4^-	(1578)
		439	5^-	(1642)
		348	3^-	1732.50(16)

Table 4.9 – continued from previous page

E_i (keV)	J^π_i	E_f (keV)	J^π_f	E_γ (keV)
		320	2^-	1760.97(21)
2100	(5^-)	2007	[a]	(93)
		1777	6^+	(323)
		1707	5^+	393.01(2)
		1524	4^+	576.17(2)
		1248	4^-	851.32(4)
		1209	6^-	890.79(6)
		551	6^-	1549.36(6)
		503	4^-	1596.46(2)
2109	(6^-)	583	8^-	1526.02(12)
		551	6^-	1558.07(8)
		439	5^-	1669.06(7)
2147	(5^-)	551	6^-	1596.07(19)
		503	4^-	1643.82(14)
2177	(4^-)	439	5^-	1737.74(10)
		348	3^-	1829.05(9)
2315	[a]	993	3^+	1321.06(11)
		551	6^-	1764.98(18)
		348	3^-	1966.38(22)
2525	4^-	1464	5^-	1061.31(8)
		1248	4^-	1276.52(15)
		503	4^-	2021.66(9)
		439	5^-	2085.16(18)
		348	3^-	2176.54(14)
2556	4^+	1524	4^+	1032.81(4)
		1248	4^-	1308.06(10)
		439	5^-	2116.99(10)
2581	(6^-)	1524	4^+	1054.92(3)
		1464	5^-	1118.36(5)
		1209	6^-	1372.84(7)
		551	6^-	2028.32(6)
		434	7^-	2147.84(7)
2607	[a]	993	3^+	1613.27(16)
2696	3^+	1524	4^+	1172.52(12)
		993	3^+	1701.86(8)
2726	[a]	1707	5^+	(1019)
		993	3^+	1731.33(22)
		503	4^-	2223.78(65)
2731	[a]	1707	5^+	1023.93(14)

Table 4.9 – continued from previous page

E_i (keV)	J_i^π	E_f (keV)	J_f^π	E_γ (keV)
		551	6^-	2180.16(11)
2765	(4^-)	1524	4^+	1241.67(11)
		1248	4^-	1517.09(36)
		993	3^+	1771.45(8)
		503	4^-	2262.51(5)
		439	5^-	2325.74(8)
		348	3^-	2416.93(9)
2780	(5^+)	1777	6^+	1003.28(6)
		1524	4^+	1256.23(5)
		551	6^-	2229.40(6)
		439	5^-	2340.29(4)
2807	(4^+)	993	3^+	1812.56(7)
		439	5^-	2367.27(18)
2850	(3^-)	503	4^-	2346.58(5)
2883	(6^-)	1777	6^+	1106.22(6)
		1524	4^+	1359.23(10)
		551	6^-	2332.41(9)
2910	6^+	2607	[a]	302.42(12)
		551	6^-	2359.04(11)
		439	5^-	2471.70(30)
2962	3^-	503	4^-	2458.29(11)
		348	3^-	2614.97(9)
2979	(5^+)	993	3^+	1984.84(16)
		439	5^-	2539.75(13)
		348	3^-	2631.04(9)
3120	(4^-)	503	4^-	2617.39(17)
		348	3^-	2772.08(13)
3140	(6^-)	551	6^-	2589.32(10)
		439	5^-	(2699)
		434	7^-	2706.63(17)
3182	(4^-)	503	4^-	2678.81(7)
		439	5^-	2742.20(8)
		348	3^-	2834.15(31)
3236	(5^-)	1209	6^-	2026.62(28)
		439	5^-	2797.26(15)
3244	(5^-)	1464	5^-	1780.68(26)
		1336	5^-	1908.34(12)
		551	6^-	2693.64(7)
		439	5^-	2804.87(50)

Table 4.9 – continued from previous page

E_i (keV)	J^π_i	E_f (keV)	J^π_f	E_γ (keV)
		434	7^-	2810.65(45)
3326	(4^-)	503	4^-	2822.89(12)
		439	5^-	2886.06(16)
3394	(6^-)	583	8^-	2811.25(8)
		434	7^-	2960.88(7)
3444	(3^-)	1904	[a]	1540.44(19)
		993	3^+	2449.57(34)
3662	4^+	1248	4^-	2413.33(10)
		993	3^+	2668.32(40)
3879	[a]	503	4^-	3375.55(39)
		439	5^-	3439.6(19)
		348	3^-	3530.70(18)
3900	[a]	1248	4^-	2651.33(10)
		503	4^-	3397.19(26)
		348	3^-	3551.69(9)
4094	[a]	2100	(5^-)	1994.32(14)
		2007	[a]	2087.37(14)
		1777	6^+	2317.40(5)
		1524	4^+	2570.16(7)
		1248	4^-	2845.89(6)
		1209	6^-	2885.48(7)
		972	2^-	3122.02(7)
		551	6^-	3543.90(3)
		503	4^-	3591.06(4)
		434	7^-	3660.39(4)
		348	3^-	3745.94(9)
4221	[a]	1248	4^-	2973.09(15)
		348	3^-	3873.02(9)
4605	(5^-)	4221	3^+	384.36(10)
		4094	[a]	510.82(30)
		3900	[a]	705.24(9)
		3879	[a]	726.72(17)
		3662	4^+	943.88(6)
		3444	3^-	1160.78(14)
		3394	6^-	1211.09(16)
		3326	4^-	1279.60(17)
		3244	(5^-)	1360.97(6)
		3236	(5^-)	1367.77(18)
		3182	(4^-)	1423.30(9)

Table 4.9 – continued from previous page

E_i (keV)	J_i^π	E_f (keV)	J_f^π	E_γ (keV)
		3140	(6^-)	1464.68(9)
		3120	(4^-)	1484.68(11)
		2979	(5^+)	1625.91(11)
		2962	3^-	1641.78(9)
		2910	6^+	1696.70(12)
		2883	(6^-)	1722.29(9)
		2850	(3^-)	1755.07(5)
		2807	(4^+)	1798.53(8)
		2780	(5^+)	1825.33(2)
		2765	(4^-)	1839.77(4)
		2731	[a]	1874.30(9)
		2726	[a]	1879.43(15)
		2696	3^+	1909.30(6)
		2607	[a]	1997.38(24)
		2581	(6^-)	2023.42(6)
		2556	4^+	2048.86(11)
		2525	4^-	2080.29(10)
		2315	[a]	2290.10(12)
		2177	4^-	2427.82(13)
		2147	(5^+)	2458.18(10)
		2109	(6^-)	2496.51(7)
		2100	(5^-)	2505.42(3)
		2081	(4^-)	2524.03(34)
		2034	[a]	2570.85(10)
		2007	[a]	2598.57(3)
		1981	7^-	2624.44(3)
		1777	6^+	2828.88(10)
		1707	5^+	2898.71(10)
		1524	4^+	3081.23(2)
		1464	5^-	3142.17(9)
		1390	4^-	3214.81(6)
		1374	3^-	3231.02(6)
		1336	5^-	3269.32(9)
		1248	4^-	3356.96(2)
		1209	6^-	3396.52(2)
		1175	2^-	3429.62(14)
		993	3^+	3611.10(11)
		972	2^-	3633.11(7)
		551	6^-	4054.75(2)

Table 4.9 – continued from previous page

E_{i} (keV)	J_{i}^{π}	E_{f} (keV)	J_{f}^{π}	E_{γ} (keV)
		503	4^-	4101.56(28)
		439	5^-	4165.61(2)
		434	7^-	4171.38(1)
		348	3^-	4256.89(2)
		320	2^-	4285.10(11)

[a] the spin-parity value could not be assigned

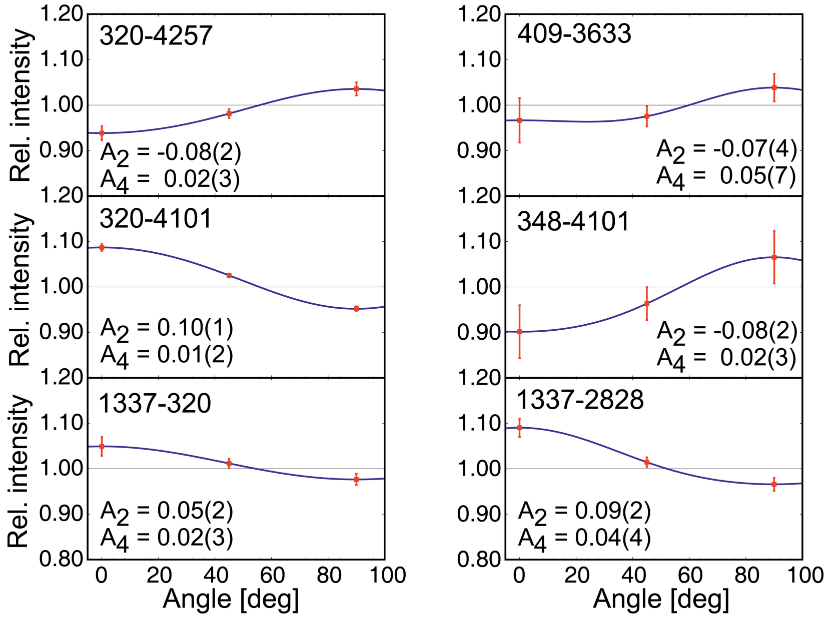

Figure 4.13. Angular correlations for the pairs of strong γ rays in ^{210}Bi. Measured points are shown together with the fitted curves and the corresponding A_2 and A_4 coefficients. Note, that the coefficients have been already corrected for attenuation factors.

Table 4.10. The measured angular-correlations coefficients A_2 and A_4, assigned multipolarity and the theoretical values of A_2 and A_4.

$E_{\gamma} - E_{\gamma}$ (keV)	Multipolarity	A_2	A_4	A_2^{theor}	A_4^{theor}
320 – 4257	$M1-(E2)$	–0.08(2)	0.02(3)	–0.086	0.0
320 – 4101	$M1-(M1)$	0.10(1)	0.01(2)	0.067	0.0
348 – 4101	$E2-(M1)$	–0.08(2)	0.02(3)	–0.079	0.0
409 – 3633	$M1-(E2)$	–0.07(4)	0.05(7)	–0.071	0.0
320 – 1337	$M1-E1$	0.05(2)	0.02(3)	0.071	0.0
1337 – 2828	$E1-(E1)$	0.09(2)	0.04(4)	0.080	0.0

CHAPTER 5

Comparison with shell-model calculations

As it was stated in Chapter 2, the remarkably large energy gaps separating both proton and neutron shells at Z=82 and N=126, respectively, make the ^{208}Pb nucleus one of the best doubly-magic nuclei in nature. As a result, nuclei located in its immediate vicinity, like the ^{205,206,210}Bi isotopes investigated in the present work, are usually described rather well within the frame of shell model.

Considering the spin-parity assignments for the newly identified excitations in these ^{205,206,210}Bi nuclei, one has to remember that deep-inelastic reactions strongly favor the population of yrast and near-yrast levels. Thus, level sequences are mostly characterized by a monotonic rise of spin with excitation energy. This consideration provides input complementary to firm experimental information in the form of selection rules, conversion coefficients, and angular distributions. Mostly $E1$, $M1$, and $E2$ multipolarities were considered for prompt transitions, however, for higher-energy γ rays ($E_\gamma > 1$ MeV) also $M2$ or $E3$ multipolarities were taken into account. In addition to the experimental information, the results of shell-model calculations were used to interpret the new levels of ^{205,206,210}Bi. On the other hand, the investigation of the decay pattern and comparison to shell-model calculations formed the basis for the spin-parity assignments to the non-yrast structure explored in ^{210}Bi using neutron-capture reaction.

In the present study, an improved version of the Kuo-Herling interaction [20] was selected in view of its success in describing recent, extensive results in ^{205,204}Pb [80, 81], ^{208}Bi [30], ^{203}Hg [29] and ^{204}Tl [82]. The calculations, performed with the OXBASH code [22], allowed one proton particle and three/four neutron holes relative to ^{208}Pb in the space of $Z\geq82$, $N\leq126$ comprising the orbitals $p_{1/2}$, $p_{3/2}$, $f_{5/2}$, $f_{7/2}$, $h_{9/2}$, and $i_{13/2}$ for the ^{205,206}Bi isotopes, as well as one neutron particle in the space of $N\geq126$ and orbitals $g_{9/2}$, $i_{11/2}$, $j_{15/2}$, $d_{5/2}$, $s_{1/2}$, $g_{7/2}$, and $d_{3/2}$, for the ^{210}Bi nucleus. The calculated energies are presented in Tables. 5.1-4.

They were calculated as binding energies relative to ^{208}Pb, but shifted by the proper number so that the experimental ground state of the considered Bi isotope is at 0 keV.

5.1 ^{206}Bi

5.1.1 Spin-parity assignments

The results of the calculations for ^{206}Bi, including only yrast and near-yrast states in the spin range 10-23, are compared with the data in Fig. 4.2 and Table 4.1. The calculated energies of all low-lying states with J=10-18 agree well with experiment. Above the 18^+ state at 4307 keV, the density of states increases. Nevertheless, there is a clear similarity between the experimental and calculated level structures in the energy range 4.3-7.1 MeV. Only two states, 20^+_1 and 21^+_1 at 6685 and 6872 keV respectively, stayed without experimental counterparts (Table 5.1). The decay proceeds through many branches resulting in a rather complex structure in this part of the level scheme. For example, five 19^- states at energies of 5207, 5402, 5610, 5793 and 5882 keV were identified. At 7118 keV, the calculations predict the state with J^π=23^+ arising from the maximally-aligned spin coupling of the valence proton particle and three neutron holes, $\pi i_{13/2} \nu i^{-3}_{13/2}$. This calculated state is associated with the experimental level at 7202 keV; i.e., with the highest excitation in the 4.3- to 7.2-MeV range. Consequently, a state identified at 7126 keV is a good candidate for the 22^+ excitation. The 76-keV $M1$ transition between these two states is not observed due to the high conversion probability and the low detection efficiency of Gammasphere at this energy. Tentative spin-parity assignments have been proposed for the levels located in this part of the level scheme; i.e., between the yrast 18^+ and 23^+ states, based on their decay pattern and the results of shell-model calculations. It is worth noting that all but three of the newly found states have their theoretical counterparts within 80 keV and, except for one level, have the same ordering. The proposed spin-parity assignments are given in Fig. 4.2. and are listed in Table 4.1. However, it should be emphasized again that the spin assignments rely heavily on comparison with calculations and, in view of the calculated high level density in parts of the spin range, remain tentative.

Table 5.1. List of yrast and near-yrast states up to spin J=23 in ^{206}Bi. Spin-parity values, main configurations, and calculated energies are given in the first three columns and compared with experimental energies in the fourth column. The last column provides the probability of the main configuration.

J^π	Main configuration	Calc. energy (keV)	Exp. energy (keV)	Probability of the main configuration (%)
10^-_1	$\pi h_{9/2} \nu p^{-2}_{1/2} i^{-1}_{13/2}$	1084	1045	55.37
11^-_1	$\pi h_{9/2} \nu f^{-1}_{5/2} p^{-1}_{1/2} i^{-1}_{13/2}$	1716	1639	58.00
12^-_1	$\pi h_{9/2} \nu f^{-1}_{5/2} p^{-1}_{1/2} i^{-1}_{13/2}$	1752	1789	75.93
13^-_1	$\pi h_{9/2} \nu f^{-1}_{5/2} p^{-1}_{1/2} i^{-1}_{13/2}$	2065	2056	92.63

Table 5.1 – continued from previous page

J^π	Main configuration	Calc. energy (keV)	Exp. energy (keV)	Probability of the main configuration (%)
13^-_2	$\pi h_{9/2}\nu f^{-2}_{5/2}i^{-1}_{13/2}$	2551	2500	45.72
14^-_1	$\pi h_{9/2}\nu f^{-2}_{5/2}i^{-1}_{13/2}$	2585	2604	85.31
14^-_2	$\pi h_{9/2}\nu f^{-1}_{5/2}p^{-1}_{1/2}i^{-1}_{13/2}$	2971	2951	71.32
15^+_1	$\pi h_{9/2}\nu p^{-1}_{1/2}i^{-2}_{13/2}$	3180	3147	87.57
17^+_1	$\pi h_{9/2}\nu f^{-1}_{5/2}i^{-2}_{13/2}$	3622	3606	97.01
16^+_1	$\pi h_{9/2}\nu f^{-1}_{5/2}i^{-2}_{13/2}$	3675	3652	72.14
18^+_1	$\pi h_{9/2}\nu f^{-1}_{5/2}i^{-2}_{13/2}$	4276	4307	97.48
16^-_1	$\pi h_{9/2}\nu f^{-1}_{7/2}f^{-1}_{5/2}i^{-1}_{13/2}$	4415	4687	89.93
16^-_2	$\pi i_{13/2}\nu p^{-1}_{1/2}i^{-2}_{13/2}$	4844	4775	75.29
17^-_1	$\pi i_{13/2}\nu p^{-1}_{1/2}i^{-2}_{13/2}$	4858	4805	80.53
19^+_1	$\pi h_{9/2}\nu f^{-1}_{5/2}i^{-2}_{13/2}$	4978	4982	98.15
18^-_1	$\pi i_{13/2}\nu p^{-1}_{1/2}i^{-2}_{13/2}$	5041	4993	66.58
18^-_2	$\pi h_{9/2}\nu i^{-3}_{13/2}$	5128	5096	97.26
19^-_1	$\pi i_{13/2}\nu f^{-1}_{5/2}i^{-2}_{13/2}$	5232	5207	49.39
18^-_3	$\pi i_{13/2}\nu f^{-1}_{5/2}i^{-2}_{13/2}$	5334	5278	70.90
18^-_4	$\pi i_{13/2}\nu f^{-1}_{5/2}i^{-2}_{13/2}$	5485	5378	81.13
19^-_2	$\pi i_{13/2}\nu f^{-1}_{5/2}i^{-2}_{13/2}$	5447	5402	51.00
20^-_1	$\pi i_{13/2}\nu f^{-1}_{5/2}i^{-2}_{13/2}$	5541	5511	97.50
19^-_3	$\pi h_{9/2}\nu i^{-3}_{13/2}$	5619	5610	94.03
19^-_4	$\pi i_{13/2}\nu f^{-1}_{5/2}i^{-2}_{13/2}$	5743	5793	97.29
19^-_5	$\pi i_{13/2}\nu f^{-1}_{5/2}i^{-2}_{13/2}$	5941	5882	90.97
21^-_1	$\pi i_{13/2}\nu f^{-1}_{5/2}i^{-2}_{13/2}$	5857	5928	98.62
20^-_2	$\pi i_{13/2}\nu f^{-1}_{5/2}i^{-2}_{13/2}$	5984	5941	94.85
20^-_4	$\pi h_{9/2}\nu i^{-3}_{13/2}$	6272	6349	98.06
19^+_4	$\pi h_{9/2}\nu f^{-1}_{7/2}i^{-2}_{13/2}$	6653	6578	68.84
20^+_1	$\pi h_{9/2}\nu h^{-1}_{9/2}i^{-2}_{13/2}$	6685	—	97.73
19^+_5	$\pi i_{13/2}\nu i^{-3}_{13/2}$	6757	6745	91.39
20^+_2	$\pi h_{9/2}\nu h^{-1}_{9/2}i^{-2}_{13/2}$	6844	6888	90.23
21^+_1	$\pi i_{13/2}\nu i^{-3}_{13/2}$	6872	—	98.87
20^+_3	$\pi i_{13/2}\nu i^{-3}_{13/2}$	6942	6895	88.91
20^+_4	$\pi i_{13/2}\nu i^{-3}_{13/2}$	7007	6990	92.90
21^+_2	$\pi i_{13/2}\nu i^{-3}_{13/2}$	7054	7015	97.29
22^+_1	$\pi i_{13/2}\nu i^{-3}_{13/2}$	7063	7126	100.00
23^+_1	$\pi i_{13/2}\nu i^{-3}_{13/2}$	7118	7202	100.00

The levels located above the 7202-keV state with $J>23$ have to originate from neutron and/or proton excitations across the $N=126$ and $Z=82$ shell gaps, respectively. Since the decay of the isomeric state at 9233 keV proceeds mostly through a single cascade, the intensities of γ rays belonging to this 713-, 361-, 480-, and 553-keV sequence are sufficiently strong to deduce their angular distributions and conversion coefficients. As stated earlier, the angular distribution (Fig. 4.5) and conversion coefficient (Table 4.2) for the 553-keV γ ray uniquely point to its stretched-$E2$ character. Assuming that this transition directly feeds the 22^+ state, a spin-parity of 24^+ can be assigned to the 7679-keV level. In turn, results of a similar analysis for the 480- and 361-keV lines (negative A_2 and conversion coefficients of 0.18(4) and 0.26(2), respectively), are compatible with their $M1$ and $\Delta J=1$ character. This results in respective quantum number assignments of 25^+ and 26^+ for the 8159- and 8520-keV states.

It should be acknowledged, however, that one cannot definitely rule out that all three 480-553, 477-76, and 346-568-keV branches feed the 23^+ state which then in turn would decay to the 22^+ level by a low-energy, $E_\gamma<80$ keV, unobserved $M1$ transition. In such a scenario, the ordering of the 76-keV γ ray in the cascade would be uncertain as well. Furthermore, the spin assignments for the core-excited states, described below, would change and all the values would be larger by $1\hbar$.

Next, for the 713-keV transition deexciting the 155-ns isomer, the angular distribution limits the spin change ΔJ to 2 or 3, whereas the conversion coefficient, 0.10(3), clearly indicates an $M2$ character. Therefore 28^- quantum numbers are assigned to the isomer at 9233 keV.

An analysis of the angular distribution or conversion coefficient for the 937-keV line connecting the two isomers could not be performed. However, by considering that the half-life of the 10170-keV isomer is significantly longer than 2 µs and by taking into account the half-lives of isomers existing in this region of the nuclear chart, an assignment of $E3$ multipolarity to the 937-keV γ ray would appear to be most probable. It follows then that the 10170-keV level would have tentative $J^\pi= 31^+$ quantum numbers.

5.1.2 Valence particle excitations $1p-3h$

As can be seen from Fig. 4.2, the lower part of the ^{206}Bi level scheme up to the 18^+ level at 4.3 MeV, where spin-parity assignments are firm, is described well by the calculations, inspiring confidence in their ability to account for the higher excitations. Indeed, the experimental ground-state binding energy of 18.645(8) MeV relative to ^{208}Pb is calculated to be 18.685 MeV reproducing it to within 40 keV. The success of the calculations can also be realized from the fact that the well-established 22^+ state at the high end of the spin-energy range under consideration has a calculated binding energy within 63 keV of experiment (see Table 5.1).

In the 4.3- to 7.1-MeV range, the yrast and near-yrast structures are rather complex with a large number of states and a multitude of decay paths. Despite this apparent complexity, the comparison between the newly-established data and the calculations in this range is rather striking and the agreement is satisfactory.

The following general features can be highlighted from comparisons between experiment and calculations. The states immediately above the 10^- isomer are characterized by a negative parity and are understood as arising from excitations involving a proton particle occupying the $h_{9/2}$ orbital while the neutron holes occupy the opposite parity $f_{5/2}$, $p_{1/2}$ and $i_{13/2}$ states. Moving up in excitation energy above the 14^- levels, a parity change occurs and the dominant sequence takes place between the 15.6-ns, 15^+ isomer and the 19^+ level at 4982 keV. As seen in Table 5.1, the calculations indicate that these states involve the dominant $\pi h_{9/2} \nu f_{5/2}^{-1} i_{13/2}^{-2}$ configuration, with the exception of the 3147-keV, 15^+ level with a dominant $\pi h_{9/2} \nu p_{1/2}^{-1} i_{13/2}^{-2}$ component in its wave function; i.e., the $f_{5/2}$ neutron hole is being replaced by the $p_{1/2}$ one located close in excitation energy. Starting from an energy of ~4.6 MeV, most of the states are of negative parity, an observation accounted for in the calculations by the proton occupying preferentially the $i_{13/2}$ orbital while two neutron holes are in the corresponding $i_{13/2}$ state with the third occupying either the $p_{1/2}$ or $f_{5/2}$ state. The members of the $\pi i_{13/2} \nu f_{5/2}^{-1} i_{13/2}^{-2}$ multiplet "terminate" in a calculated 5857-keV 21^- state resulting from the maximal alignment of all spins in this configuration. The associated experimental level is located 71 keV higher, at 5928 keV. For the highest valence excitations, above ~6.7 MeV, another change in parity is observed and the levels have a $\pi i_{13/2} \nu i_{13/2}^{-3}$ main configuration, which terminates in a maximally-aligned, "terminating" 23^+ state computed at 7118 keV and associated with the 7202-keV level in the data.

5.1.3 Core excitations

Of particular interest are the two isomers located at 9233 (with the half-life $T_{1/2}$=155 ns) and 10170 keV ($T_{1/2}$>2µs) with probable spin-parity 28^- and 31^+. It is quite certain that these two isomeric states, as well as other yrast excitations located above spin 23^+ in ^{206}Bi, have to involve excitations across the shell gaps at N=126 and/or Z=82; i.e., core excitations. There is, however, no obvious guidance about which of the low-lying states in ^{206}Bi and which of the core excitations in ^{208}Pb would couple to give rise to isomers. Indeed, such couplings on the one hand involve one-proton-particle and three-neutron-holes configurations and, on the other, neutron or proton particle-hole excitations which are too complex to evaluate excitation energies from first principles. In order to describe these levels, the appropriate shell-model calculations would have to be carried out, but these are presently difficult to perform due to limitations imposed by the large model space. Thus, the levels located in ^{206}Bi above spin 23^+, can serve as a suitable testing ground for future large shell-model calculations that involve particle-hole excitations near doubly-magic ^{208}Pb.

5.2 ^{205}Bi

5.2.1 Spin-parity assignments

The results of shell-model calculations for the ^{205}Bi nucleus were compared with experimental data – this is shown in Table 5.2 and Figure 4.7. The yrast states in the spin range

9/2–53/2 and energies up to 10 MeV arise from couplings of 1 proton- 4 neutron-holes on the orbitals belonging to the Kuo-Herling model space. The experimental structure, established up to the 7975-keV isomeric level, is reproduced rather well by these calculations. In the lower part of the level scheme, the experimental spin-parity assignments agree nicely with theory, although the ordering of some calculated levels; e.g., first two excitations at 796 and 881 keV with $J^{\pi}=11/2^{-}$ and $13/2^{-}$, respectively, or two isomeric levels $25/2^{+}$ at 2139 and $21/2^{+}$ at 2065 keV were not reproduced by the calculations. Concerning the tentative spin assignment of $15/2^{+}$ or $13/2^{-}$ to the 1310-keV level, calculations favor the second possibility, e.g. $13/2^{-}$. In the higher excitation energy range of 2139-4180 keV, the spin-parity assignments coming from earlier works also agree well with shell model predictions. The newly added state in this region at 3927 keV fed by a 1031-keV γ ray from the 4958-keV level must have $J^{\pi}=31/2^{-}$. An unobserved 32-keV transition deexciting this level does not have isomeric character, thus is probably of $M1$ multipolarity. This ordering of the 1031-32-keV cascade is also predicted by the calculations. Above the first $35/2^{-}$ excitation, the experimental states are rather dense. In addition, the decay pattern in this portion of the level scheme is quite complex: for example, seven $41/2^{+}$ states were found at energies 5942, 6711, 6777, 6809, 6846, 6903, and 7039 keV. All this causes difficulties in proposing firm spin-parity assignments.

Table 5.2. List of yrast and near-yrast states up to spin $J = 53/2$ in ^{205}Bi. Spin-parity values, main configurations, and calculated energies are given in the first three columns and compared with experimental energies in the fourth column. The last column provides the probability of the main configuration.

J^{π}	Main configuration	Calc. energy (keV)	Exp. energy (keV)	Probability of the main configuration (%)
$9/2^{-}_{1}$	$\pi h_{9/2}\nu f^{-2}_{5/2}p^{-2}_{1/2}$	83	0	36.93
$11/2^{-}_{1}$	$\pi h_{9/2}\nu f^{-3}_{5/2}p^{-1}_{1/2}$	959	796	23.58
$13/2^{-}_{1}$	$\pi h_{9/2}\nu f^{-2}_{5/2}p^{-2}_{1/2}$	902	881	41.15
$13/2^{-}_{2}$	$\pi h_{9/2}\nu f^{-2}_{5/2}p^{-2}_{1/2}$	1182	1110	52.64
$15/2^{-}_{1}$	$\pi h_{9/2}\nu f^{-2}_{5/2}p^{-2}_{1/2}$	1266	1168	58.20
$13/2^{-}_{3}$	$\pi h_{9/2}\nu f^{-2}_{5/2}p^{-2}_{1/2}$	1434	1310	40.55
$17/2^{-}_{1}$	$\pi h_{9/2}\nu f^{-2}_{5/2}p^{-2}_{1/2}$	1279	1344	71.36
$17/2^{-}_{2}$	$\pi h_{9/2}\nu f^{-3}_{5/2}p^{-1}_{1/2}$	1708	1572	39.79
$15/2^{-}_{2}$	$\pi h_{9/2}\nu f^{-1}_{5/2}p^{-1}_{3/2}p^{-2}_{1/2}$	1809	1701	39.59
$15/2^{-}_{3}$	$\pi h_{9/2}\nu f^{-3}_{5/2}p^{-1}_{1/2}$	1877	1838	45.99
$17/2^{+}_{1}$	$\pi h_{9/2}\nu f^{-1}_{5/2}p^{-2}_{1/2}i^{-1}_{13/2}$	2095	2041	51.84
$21/2^{+}_{1}$	$\pi h_{9/2}\nu f^{-1}_{5/2}p^{-2}_{1/2}i^{-1}_{13/2}$	2069	2064	58.84
$25/2^{+}_{1}$	$\pi h_{9/2}\nu f^{-1}_{5/2}p^{-2}_{1/2}i^{-1}_{13/2}$	2054	2139	65.34
$27/2^{+}_{1}$	$\pi h_{9/2}\nu f^{-2}_{5/2}p^{-1}_{1/2}i^{-1}_{13/2}$	2733	2779	62.28
$27/2^{+}_{2}$	$\pi h_{9/2}\nu f^{-1}_{5/2}p^{-2}_{1/2}i^{-1}_{13/2}$	3025	3198	45.58
$29/2^{+}_{1}$	$\pi h_{9/2}\nu f^{-2}_{5/2}p^{-1}_{1/2}i^{-1}_{13/2}$	3148	3200	63.52

Table 5.2 – continued from previous page

J^{π}	Main configuration	Calc. energy (keV)	Exp. energy (keV)	Probability of the main configuration (%)
$29/2^-_1$	$\pi h_{9/2} \nu p^{-2}_{1/2} i^{-2}_{13/2}$	3332	3379	52.71
$31/2^-_1$	$\pi h_{9/2} \nu f^{-1}_{5/2} p^{-1}_{1/2} i^{-2}_{13/2}$	3878	3895	35.67
$31/2^-_2$	$\pi h_{9/2} \nu f^{-1}_{5/2} p^{-1}_{1/2} i^{-2}_{13/2}$	4133	3927	51.39
$33/2^-_1$	$\pi h_{9/2} \nu f^{-1}_{5/2} p^{-1}_{1/2} i^{-2}_{13/2}$	3916	4020	74.49
$35/2^-_1$	$\pi h_{9/2} \nu f^{-1}_{5/2} p^{-1}_{1/2} i^{-2}_{13/2}$	4130	4172	89.87
$31/2^+_1$	$\pi h_{9/2} \nu f^{-2}_{5/2} p^{-1}_{1/2} i^{-1}_{13/2}$	3970	4180	44.74
$35/2^-_2$	$\pi h_{9/2} \nu f^{-1}_{5/2} p^{-1}_{1/2} i^{-2}_{13/2}$	4556	4651	64.45
$37/2^-_1$	$\pi h_{9/2} \nu f^{-2}_{5/2} i^{-2}_{13/2}$	4630	4696	70.87
$37/2^-_2$	$\pi h_{9/2} \nu f^{-1}_{5/2} p^{-1}_{1/2} i^{-2}_{13/2}$	4815	4934	66.32
$33/2^+_1$	$\pi h_{9/2} \nu f^{-1}_{7/2} f^{-1}_{5/2} p^{-1}_{3/2} i^{-1}_{13/2}$	4772	4958	76.44
$35/2^+_1$	$\pi i_{13/2} \nu p^{-2}_{1/2} i^{-2}_{13/2}$	5140	5164	41.32
$37/2^-_3$	$\pi h_{9/2} \nu f^{-1}_{5/2} p^{-1}_{3/2} i^{-2}_{13/2}$	5189	5249	46.71
$37/2^+_1$	$\pi i_{13/2} \nu p^{-2}_{1/2} i^{-2}_{13/2}$	5358	5392	40.02
$39/2^-_1$	$\pi h_{9/2} \nu f^{-2}_{5/2} i^{-2}_{13/2}$	5294	5407	73.78
$37/2^+_2$	$\pi h_{9/2} \nu p^{-1}_{1/2} i^{-3}_{13/2}$	5467	5485	82.02
$37/2^+_3$	$\pi i_{13/2} \nu f^{-1}_{5/2} p^{-1}_{1/2} i^{-2}_{13/2}$	5657	5598	54.03
$39/2^-_2$	$\pi h_{9/2} \nu f^{-1}_{5/2} p^{-1}_{1/2} i^{-2}_{13/2}$	5542	5652	73.42
$39/2^+_1$	$\pi i_{13/2} \nu f^{-1}_{5/2} p^{-1}_{1/2} i^{-2}_{13/2}$	5801	5704	64.17
$39/2^+_2$	$\pi h_{9/2} \nu p^{-1}_{1/2} i^{-3}_{13/2}$	5886	5931	54.17
$41/2^+_1$	$\pi h_{9/2} \nu f^{-1}_{5/2} i^{-3}_{13/2}$	5885	5942	95.55
$41/2^-_1$	$\pi h_{9/2} \nu f^{-2}_{5/2} i^{-2}_{13/2}$	5971	—	90.43
$43/2^+_1$	$\pi h_{9/2} \nu f^{-1}_{5/2} i^{-3}_{13/2}$	6340	6453	94.31
$41/2^+_5$	$\pi h_{9/2} \nu p^{-1}_{3/2} i^{-3}_{11/2}$	6542	6711	48.26
$41/2^+_6$	$\pi f_{7/2} \nu p^{-1}_{1/2} i^{-3}_{13/2}$	6621	6777	28.71
$41/2^+_7$	$\pi i_{13/2} \nu f^{-2}_{5/2} i^{-2}_{13/2}$	6681	6809	28.40
$41/2^+_8$	$\pi h_{9/2} \nu f^{-1}_{5/2} i^{-3}_{13/2}$	6695	6846	44.63
$41/2^+_9$	$\pi i_{13/2} \nu f^{-2}_{5/2} i^{-2}_{13/2}$	6794	6903	50.78
$41/2^+_{10}$	$\pi i_{13/2} \nu f^{-2}_{5/2} i^{-2}_{13/2}$	6873	7039	53.52
$45/2^+_1$	$\pi i_{13/2} \nu f^{-2}_{5/2} i^{-2}_{13/2}$	6962	—	89.35
$43/2^+_5$	$\pi i_{13/2} \nu f^{-2}_{5/2} i^{-2}_{13/2}$	7010	7063	52.52
$43/2^+_6$	$\pi h_{9/2} \nu p^{-1}_{1/2} i^{-3}_{13/2}$	7053	7140	45.27
$43/2^+_7$	$\pi i_{13/2} \nu f^{-1}_{5/2} p^{-1}_{3/2} i^{-2}_{13/2}$	7188	7214	49.76
$43/2^+_8$	$\pi h_{9/2} \nu f^{-1}_{5/2} i^{-3}_{13/2}$	7257	7364	91.17
$45/2^+_3$	$\pi f_{7/2} \nu f^{-1}_{5/2} i^{-3}_{13/2}$	7310	7409	94.89
$45/2^-_1$	$\pi i_{13/2} \nu p^{-1}_{1/2} i^{-3}_{13/2}$	7406	—	50.64

Table 5.2 – continued from previous page

J^π	Main configuration	Calc. energy (keV)	Exp. energy (keV)	Probability of the main configuration (%)
$47/2_1^+$	$\pi h_{9/2}\nu f_{5/2}^{-1} i_{13/2}^{-3}$	7494	7590	98.12
$47/2_1^-$	$\pi i_{13/2}\nu p_{1/2}^{-1} i_{13/2}^{-3}$	7564	—	60.45
$45/2_2^-$	$\pi i_{13/2}\nu f_{5/2}^{-1} i_{13/2}^{-3}$	7629	7622	56.10
$49/2_1^-$	$\pi i_{13/2}\nu f_{5/2}^{-1} i_{13/2}^{-3}$	7884	7916	97.60
$51/2_1^-$	$\pi i_{13/2}\nu f_{5/2}^{-1} i_{13/2}^{-3}$	8134	7975	98.74
$53/2_1^+$	$\pi i_{13/2}\nu i_{13/2}^{-4}$	9457	—	99.74
$53/2_1^-$	$\pi i_{13/2}\nu f_{7/2}^{-1} i_{13/2}^{-3}$	10258	—	79.63

In spite of these difficulties, comparison with theory helped to assign spins to levels at 6846, 6809, 6777, and 6711 keV. The four cascades which were used to locate those levels, that is, 294-2674-, 330-2637-, 363-2604-, and 429-2539 keV, connect the 7140-keV excitation with the $35/2^-$ yrast state at 4172 keV. Intensities of γ rays belonging to the cascades were, unfortunately, not strong enough to determine their order by using prompt to delayed ratio values. However, by considering that shell-model calculations predict several $41/2^+$ states in the energy range of 6.7-7.0 MeV, the 2674-, 2637-, 2604-, and 2539-keV γ rays could be interpreted as $E3$ transitions feeding the 4172-keV level.

The state at 7140 keV was found to decay by 11 branches. One of the strongest is a 2443-keV γ ray leading to the state with $J^\pi = 37/2^-$ established in previous studies [39]. As this level is not an isomer, the highest multipole which can be assigned to the 2443-keV transition is $E3$. This limits the spin-parity for the 7140-keV excitation to $J^\pi = 43/2^+$, although the $41/2^+$ or $41/2^-$ values cannot be rigorously excluded.

Similarly, the deexcitation of a level at 7063 keV proceeds through 9 branches one of which, the 2368-keV γ ray, leads to the $37/2^-$ state. Also here, by assuming $E3$ multipolarity to this 2368-keV transition the 7063-keV level was associated with the $43/2^+$ excitation calculated to be at 7010 keV.

The ordering of the cascades 1411-717 and 1814-1076 keV was not certain because the intensities are too weak to calculate reliable prompt to delayed ratios. Again, it was adopted as suggested by the comparison with theory.

Only very tentative spin-parity assignments are possible for the levels in the range of 7140-7975 keV. As the state at 7063 keV was assigned to be of $43/2^+$ spin-parity, and as the γ ray feeding it – 151 keV – is probably a $M1$ transition, as inferred from its conversion coefficient, the possible J^π values for the 7214-keV excitation are $43/2^+$ or $45/2^+$. In the calculations, the closest available $43/2_7^+$ state is at 7188 keV, while $45/2_2^+$ and $45/2_3^+$ levels are at 7009 and 7310 keV, respectively. A spin-parity of $43/2_7^+$ was finally proposed, but $45/2_3^+$ is also possible. Next, the cascade of two transitions, 195 and 181 keV (also of $M1$ character), located states at 7409 and 7590 keV, whose spins may take values $45/2^+$ and $47/2^+$. The yrast state $47/2^+$ calculated at 7494 keV was assigned to the 7590-keV level, whereas for the experimental 7409-keV excitation, the $45/_3^+$ 7310-keV theoretical counterpart was chosen. The line of 385 keV, deexciting the long-lived isomer at 7975 keV may then be an $M2$ transition from the yrast $51/2^-$ state calculated at 8134 keV.

The parallel cascade, 482-295 keV, must be connected with the highest excitation at 7975 keV by a low-energy, unobserved transition, which makes it harder to establish the energies of the levels. The 482-keV γ ray feeds the 7140-keV, $43/2^+$ state from 7622-keV excitation for which a J^π=$45/2^-$ value was assigned. Then, the 7916-keV excitation may correspond to the yrast $49/2^-$ state decaying by an $M1$ 295-keV line to the 7622-keV level. The assumed 59-keV γ ray deexciting the isomeric 7975-keV level would have to be of $M1$ character.

The level at 7364 keV decaying by the 2668-keV transition to the $37/2^-$ state may have the $43/2_8^+$ J^π value, assuming that this γ ray is of the $E3$ type, because it does not have a measurable lifetime. Thus, the higher J^π values are not likely. The energies of two lines, 263 and 99 keV located above, do not sum to give the energy of the isomer at 7975 keV, therefore the low-energy transitions probably exist but it is not possible to exactly place them. Due to this fact, the location of the levels should be treated as very tentative and firm spin-parity assignments cannot be proposed.

For all those states, tentative spin-parity assignments have been proposed, based on their decay pattern and the results of shell-model calculations. The states with maximal J^π values, of $53/2^+$ and $53/2^-$, arising from the maximum couplings of $\pi i_{13/2}\nu i_{13/2}^{-4}$ and $\pi i_{13/2}\nu f_{7/2}^{-1} i_{13/2}^{-3}$ configurations of the valence proton particle and four neutron holes predicted by the calculations at 9457 and 10258 keV were not observed. The proposed spin-parity assignments to the levels located in ^{205}Bi are given in Fig. 4.7 and are listed in Table 5.2.

5.2.2 Valence particles excitations $1p - 4h$

As discussed in the previous section and as can be seen from Fig. 4.7, the lower part of the ^{205}Bi level scheme up to the $35/2^+$ level at 5.2 MeV, where spin-parity assignments are firm, is described well by the calculations, inspiring confidence in their ability to account for the higher excitations. Indeed, the experimental ground-state binding energy of 25.683(5) MeV, relative to ^{208}Pb is calculated to be 25.766 MeV reproducing it to within 83 keV.

In the 5.2- to 8.0-MeV range, the yrast and near-yrast structures are rather complex with a large number of states and a multitude of decay paths. Despite this apparent complexity, the agreement between the newly-established data and the calculations in this range is rather satisfactory.

The following general features of excited structures in ^{205}Bi can be highlighted from comparisons between experiment and calculations. As seen in Table 5.2, the levels immediately above the $9/2^-$ ground state are characterized by a negative parity. They are understood as arising from excitations involving negative parity orbitals: the proton particle occupies the $h_{9/2}$ state and the four neutron holes are are associated with the $f_{5/2}$ and $p_{1/2}$ ($p_{3/2}$ in case of $15/2_2^-$) orbitals. For the 200- and 100-ns isomers at 2139 and 2064 keV, a parity change occurs and low-energy $E2$ transitions (between the states $25/2_1^+ \rightarrow 21/2_1^+ \rightarrow 17/2_1^+$, with assigned $\pi h_{9/2} \nu f_{5/2}^{-1} p_{1/2}^{-2} i_{13/2}^{-1}$ dominant component in their wave functions) are responsible for the observed lifetimes. The positive parity configurations describe also the excitations below the $29/2^-$, 2.5-ns isomer at 3379 keV.

The higher lying states are of both positive and negative parities. The computed $31/2^-$, $33/2^-$, $35/2^-$, $31/2^+$, $37/2^-$, $33/2^+$, $35/2^+$, $37/2^+$, $39/2^-$, $39/2^+$ yrast levels have been associated with the experimental states. The calculations indicate that for higher lying states starting from the $37/2_1^+$, 5358-keV excitation a change may occur: the $h_{9/2}$ proton particle is replaced by the $i_{13/2}$ one. In the energy range 5.7 to 7.6 MeV, the located states are of positive parity. The first $41/2^+$ state computed at 5885 keV corresponds to the 5942-keV level in the data. Moreover, the six non-yrast $41/2^+$ states predicted by theory have their experimental counterparts. Further, the $43/2_1^+$ state predicted by the calculations at 6340 keV was associated with the 6453-keV experimental level. Also, the experimental levels at 7063, 7140, 7214, and 7364 keV were assigned as $43/2^+$ states. The highest three extitations are of negative parity, $45/2_2^-$, $49/2_1^-$, $51/2_1^-$, and result from the configuration $\pi i_{13/2} \nu f_{5/2}^{-1} i_{13/2}^{-3}$.

There is no experimental evidence regarding the valence particle-holes yrast excitations $53/2^+$ and $53/2^-$ that are expected to occur above the isomeric state at 7975-keV level. The main reason is that γ rays from those states could not be observed in the present experiments due to the long lifetime of the isomer.

5.3 ^{210}Bi – yrast states

5.3.1 Spin-parity assignments

The level structure of ^{210}Bi calculated within the shell model was compared to the experimental results. The yrast and near-yrast states in the spin range 9-14 arising from excitations of one proton and one neutron are presented in Fig. 4.9 and Table 5.3. All of these energies agree very well with the experimental data; e.g. within 8 keV. The level scheme is rather simple in this region, however for the higher-lying states, which must involve core excitations, the density of levels increases.

The results on conversion coefficients and angular distributions described in section 4.3.1 confirm the previous J^π assignments to the levels above the long-lived 9^- isomer. The 653-398-keV cascade, consisting of pure $E1$ and mixed $M1{+}E2$ transitions, locates 10^- and 11^+ excitations, while the decay of a 2725-keV level through a 1403-keV $E3$ branch establishes the quantum numbers of this state as 14^-. The multipolarities of the 151- and 1252-keV transitions, $M1{+}E2$ and $M2{+}E3$, respectively, are in agreement with this assignment, supporting also the 12^+ assignment to the excitation at 1473 keV. It is worthwhile to note that the 14^- state at 2734 keV is an excitation with the highest spin predicted by the present calculations – it arises from a maximally-aligned spin coupling of the $i_{13/2}$ proton and $j_{15/2}$ neutron.

The higher lying states must involve core excitations, so the spin-parity assignments for the levels above 3 MeV were done based only on experimental information. The angular distribution of the 744-keV transition uniquely points to its pure $\Delta J{=}1$ character, thus an $E1$ multipolarity may be assigned to it. This establishes $J^\pi{=}15^+$ for the 3469-keV state.

The second branch deexciting the level at 3469 keV, i.e., the 175-keV branch, with a conversion coefficient α(175 keV)=0.7(1) indicates a $E2$ multipolarity, and, as a result a 3294-keV excitation, fed by this transition, may have spin-parity assignment 13^+. The existence of the 1821-keV $M1 + E2$ branch from the 3294-keV level provides additional support for this interpretation.

The spin of the state at 4085 keV could be deduced by analyzing the multipolarity of the 2613-keV γ ray. Initially, this state was expected to arise from a coupling of the collective 3^- ^{208}Pb core excitation to the 12^+ state, and thus an octupole character was expected for the 2613-keV transition. However, the results of the angular distribution analysis suggest rather a ΔJ=2 character for this γ ray. Since in this case one cannot exclude the possibility of mixing with an higher order multipole, the $M2(+E3)$ multipolarity was finally assigned to the 2613-keV transition. This determines the 14^- spin-parity value for the 4085-keV state. Consequently, an $M1$ multipolarity was established for a very weak 1361-keV line. The 153-keV transition, feeding the 14^- state is probably of $M1$ character, thus a J^π=15^- value was associated with the 4239-keV excitation. The parallel branch, e.g. the 1514-keV γ ray, connects this level with the 2725-keV, 14^- state and has $M1$+$E2$ multipolarity. Assuming this scenario and taking into account the extracted conversion coefficients, the 224- and 131-keV transitions, which both are of $M1$ character, locate 16^- and 17^-states at 4239 and 4594 keV, respectively. The parallel cascade consisting of 561- and 564-keV γ rays, connects this 4594-keV level with the 15^+ isomer at 3469 keV. However, a reliable angular distribution for those lines could not be obtained due to the small difference in energy between them – the suggestion is that they are probably of ΔJ=1 character (561 may be of $M1$+$E2$ and 564 of $E1$ multipolarity). Thus, a very tentative assignment of J^π=16^+ was was proposed for the 4030-keV intermediate level.

An analysis of conversion coefficients for the higher-lying transitions could not be performed due to their weak intensities and problems with the probable no observation of some low-energy decay branches. The angular distributions were obtained only for the 371- and 783-keV lines. The coefficient A_2=0.23(6) (and A_4 equal to 0 within the error) indicates an $E2$ multipolarity for the 371-keV transition. Since the transition feeds the 17^- state at 4594 keV, 19^- quantum numbers were assigned to the 4965-keV level. For the 783-keV line, $M1$+$E2$ multipolarity was deduced. Assuming then that this transition directly feeds the 19^- state, a spin of 20^- can be assigned to the 5748-keV level.

5.3.2 One-proton one-neutron excitations

The shell-model calculations performed for the valence-particles excitations in the ^{210}Bi nucleus reproduce its lower-lying yrast structure very well (within 9 keV). The configurations of those five states are very pure, involving over 90% of one configuration. The ground state, with spin-parity 9^-_1 is of $\pi h_{9/2} \nu g_{9/2}$ character, and higher excitations involve also a proton occupying the $i_{13/2}$ orbital and a neutron in the $i_{11/2}$ and $j_{15/2}$ states. The calculations predict the state 13^-_1 at 3606 keV, but the corresponding experimental level was not observed, probably because of the presence of states arising from core excitations, which apparently

Table 5.3. List of yrast states up to spin J=14 in ^{210}Bi. Spin-parity values, main configurations, and calculated energies are given in the first three columns and compared with experimental energies in the fourth column. The last column provides the probability of the main configuration.

J^π	Main configuration	Calc. energy (keV)	Exp. energy (keV)	Probability of the main configuration (%)
9_1^-	$\pi h_{9/2}\nu g_{9/2}$	272	271	99.11
10_1^-	$\pi h_{9/2}\nu i_{11/2}$	670	669	99.94
11_1^+	$\pi i_{13/2}\nu g_{9/2}$	1316	1322	92.18
12_1^+	$\pi h_{9/2}\nu j_{15/2}$	1469	1473	93.25
14_1^-	$\pi i_{13/2}\nu j_{15/2}$	2734	2725	100.00
13_1^-	$\pi i_{13/2}\nu j_{15/2}$	3606	—	100.00

become yrast in this region.

5.3.3 Core excitations

It is certain that yrast excitations located above spin 14$^-$ in ^{210}Bi have to involve excitations across the shell gaps at N=126 and/or Z=82. The lowest of them, the level at 3294 keV with an assigned spin-parity value of 13$^+$, probably involves the neutron excited through the energy gap from the $p_{1/2}$ single particle state to the $g_{9/2}$ orbital (forming a neutron hole in the $p_{1/2}$ state). In this case, the maximally-aligned spin coupling of the three valence particles and one hole, e.g. the $\pi h_{9/2}\nu g_{9/2}^2 p_{1/2}^{-1}$ configuration, results indeed in J^π=13$^+$. There is, however, no obvious guidance which would help establish the configurations corresponding to remaining newly identified high-lying states in ^{210}Bi. Such configurations on the one hand involve one-proton- and one-neutron-particle configurations and, on the other, neutron or proton particle-hole excitations which are too complex for evaluating their excitation energies from simple considerations. In order to describe these states, the appropriate shell-model calculations would have to be carried out. Thus, the levels located in ^{210}Bi above spin 14$^-$ can serve as a suitable testing ground for future large shell-model calculations that involve particle-particle and particle-hole excitations near doubly-magic ^{208}Pb.

5.4 ^{210}Bi – low-spin structure

The results of shell-model calculations regarding ^{210}Bi low-spin levels, performed with the KHPE interaction, were compared with the findings from the neutron-capture data analysis. We found that 61 states were populated in the decay following neutron capture; 24 of them were not reported in the literature previously. They arise mainly from the excitations of one proton- and one neutron- valence particles, although some of them might be influenced by the 3$^-$ octupole excitation which in ^{208}Pb nucleus lies at 2615 keV. This low-lying octupole vibration of the ^{208}Pb core contributes significantly to the structure of states in neigbouring nuclei.

The agreement between experiment and theory in the lower part of the scheme is striking. All spin-parity values up to ∼2 MeV that were firmly established in the previous studies, are reproduced within 3 keV. Also, for the states with only tentative spin-parity assignments the calculations seem to reproduce the data well. We expect thus that also at higher excitation energy the calculations should do well. With this assumption in mind, for the higher-lying levels we performed tentative spin-parity assignments based on the comparison with calculations and taking into account the selection rules for γ decay. In the course of this analysis, new J^π assignments for previously known levels at 2765 and 3244 keV were proposed as (4^-) and (5^-), respectively. The state at 2765 keV was previously associated with J^π values of (3^-), but the present calculations suggest rather that its counterpart is a 4^- state which lies at 2760 keV. In turn, the 3244-keV level, decaying to the states with spin-parity of 5^-, 6^- and 7^-, was previously assigned as (7^-). Since now the theory predicts the closest 7^- excitation at 3145 keV (i.e., rather far from the experimental value), we prefer to associate this excitation with the 5^- state calculated at 3254 keV, although the 7^- possibility cannot be rigorously excluded.

All together, J^π values have been assigned to the newly found states at 2147, 2556, 2581, 2696, 2780, 2807, 2850, 2883, 2962, 2979, 3120, 3236, 3326, 3394, 3444, and 3662 keV. The results of all the assignments are summarized in Table 5.4. The spins of those states are in the range of 3 to 6, with both positive and negative parity. In particular, for the 2556-, 2696-, 2962-, 3662-keV levels firm spin-parity assignments were proposed, due to clear correspondence between the possible spin value resulting from the deserved decay paths and the indications from theoretical calculations.

Some of the levels which have been located in ^{210}Bi do not have their theoretical counterparts. These are: the previously known excitations at 2007, 2034, and 2315 keV and newly found states at 1904, 2607, 2726, 2731, 3879, 3900, 4094, and 4221 keV.

The present status of the proton-neutron multiplets identification is as follows: all of the 10 states from the $\pi h_{9/2}\nu g_{9/2}$ multiplet with spins 0-9 and negative parity were observed in the present experiment. At higher excitation energy, states arising from the excitation of a neutron to the $i_{11/2}$ orbital or proton to the $f_{7/2}$ orbital should appear. Indeed, the multiplet $\pi h_{9/2}\nu i_{11/2}$ is represented by 563-, 1175-, 1336-, 1390-, 1981-keV states, while the configuration $\pi f_{7/2}\nu g_{9/2}$ is associated with the 916-, 972-, 1209-, 1248-, 1464-keV levels. The members of the three multiplets mentioned above are of negative parity, but the higher-lying part of the ^{210}Bi level scheme includes also the positive parity states. In general, the rest of populated states involves protons on $i_{13/2}$ and $f_{5/2}$ orbitals and neutrons on $j_{15/2}$, $d_{5/2}$, $s_{1/2}$, $g_{7/2}$, and $d_{3/2}$ single-particle states. Thus, the states identified in this work have configurations which arise from neutron and proton promotions to almost all orbitals available above the ^{208}Pb core allowed by the Kuo-Herling model space.

After the capture of a cold neutron with energy of ∼5 meV, the ^{210}Bi excitation energy is well defined (B_n=4604.63 keV) and one expects population of excited states available at this energy. As the average spacing between states at around 4.6 MeV is of the order of 1 eV and their width of the order of a fraction of eV, one might expect population of more than one state in this case. We have performed an analysis aimed at establishing the spin-parity value(s) of the state/states populated in the 5 meV neutron capture on ^{209}Bi. As shown in Sec. 4.3.2, the spin-parity of those states in ^{210}Bi was determined from the angular correlation analysis of strong γ rays to be 4^- or 5^-. Additionally, taking into account the selection rules, which exclude decay by $M3$ transitions, the primary γ rays (originating from states after the capture) feeding 2^- levels must come from a 4^- initial state and be of $E2$ character. Similarly, decay to the 7^- states can proceed only via $E2$ transitions from a 5^- excitation. This leads to the conclusion that after the capture of a 5 meV neutron by the ^{209}Bi nucleus, two resonances, with J^π=4^- and 5^-, may be populated in ^{210}Bi.

Table 5.4. List of shell-model states populated in ^{210}Bi after the neutron-capture reaction. Spin-parity values, main configurations, and calculated energies are given in the first three columns and compared with experimental energies in the fourth column. The last column provides the probability of the main configuration.

J^π	Main configuration	Calc. energy (keV)	Exp. energy (keV)	Probability of the main configuration (%)
1^-_1	$\pi h_{9/2}\nu g_{9/2}$	0	0	95.93
0^-_1	$\pi h_{9/2}\nu g_{9/2}$	48	46	97.92
9^-_1	$\pi h_{9/2}\nu g_{9/2}$	272	271	99.11
2^-_1	$\pi h_{9/2}\nu g_{9/2}$	319	320	95.73
3^-_1	$\pi h_{9/2}\nu g_{9/2}$	347	348	97.25
7^-_1	$\pi h_{9/2}\nu g_{9/2}$	434	434	97.52
5^-_1	$\pi h_{9/2}\nu g_{9/2}$	441	439	97.78
4^-_1	$\pi h_{9/2}\nu g_{9/2}$	504	503	98.10
6^-_1	$\pi h_{9/2}\nu g_{9/2}$	550	551	98.64
1^-_2	$\pi h_{9/2}\nu i_{11/2}$	565	563	49.36
8^-_1	$\pi h_{9/2}\nu g_{9/2}$	584	583	97.39
8^-_2	$\pi f_{7/2}\nu g_{9/2}$	916	916	92.47
2^-_2	$\pi f_{7/2}\nu g_{9/2}$	974	972	43.85
3^+_1	$\pi h_{9/2}\nu j_{15/2}$	993	993	94.03
2^-_3	$\pi h_{9/2}\nu i_{11/2}$	1173	1175	52.00
6^-_2	$\pi f_{7/2}\nu g_{9/2}$	1206	1209	93.79
4^-_2	$\pi f_{7/2}\nu g_{9/2}$	1248	1248	92.19
5^-_2	$\pi h_{9/2}\nu i_{11/2}$	1335	1336	74.83
3^-_2	$\pi h_{9/2}\nu d_{5/2}$	1375	1374	93.70
4^-_3	$\pi h_{9/2}\nu i_{11/2}$	1389	1390	96.12
5^-_3	$\pi f_{7/2}\nu g_{9/2}$	1464	1464	74.63
4^+_1	$\pi h_{9/2}\nu j_{15/2}$	1524	1524	91.72
5^+_1	$\pi h_{9/2}\nu j_{15/2}$	1708	1707	93.21
6^+_1	$\pi h_{9/2}\nu j_{15/2}$	1776	1777	94.08
7^-_4	$\pi h_{9/2}\nu i_{11/2}$	1981	1981	94.15

Table 5.4 – continued from previous page

J^π	Main configuration	Calc. energy (keV)	Exp. energy (keV)	Probability of the main configuration (%)
4^-_4	$\pi h_{9/2}\nu d_{5/2}$	2021	2081	60.98
5^-_4	$\pi h_{9/2}\nu d_{3/2}$	2090	2100	87.23
6^-_4	$\pi h_{9/2}\nu d_{5/2}$	2168	2109	80.93
5^-_5	$\pi f_{7/2}\nu i_{11/2}$	2192	2147	97.06
4^-_5	$\pi f_{7/2}\nu i_{11/2}$	2199	2177	75.78
4^-_6	$\pi h_{9/2}\nu s_{1/2}$	2548	2525	75.63
4^+_3	$\pi i_{13/2}\nu i_{11/2}$	2580	2556	56.44
6^-_6	$\pi f_{7/2}\nu d_{5/2}$	2633	2581	88.83
3^+_3	$\pi i_{13/2}\nu g_{9/2}$	2709	2696	98.24
4^-_7	$\pi f_{7/2}\nu d_{5/2}$	2760	2765	56.63
5^+_3	$\pi i_{13/2}\nu i_{11/2}$	2815	2780	53.16
4^+_4	$\pi f_{7/2}\nu j_{15/2}$	2845	2807	59.92
3^-_6	$\pi f_{7/2}\nu d_{5/2}$	2903	2850	23.54
6^-_7	$\pi h_{9/2}\nu d_{3/2}$	2873	2883	61.23
6^+_4	$\pi i_{13/2}\nu s_{1/2}$	2978	2910	79.25
3^-_7	$\pi f_{7/2}\nu d_{5/2}$	2980	2962	43.32
5^+_4	$\pi f_{7/2}\nu j_{15/2}$	2958	2979	52.01
4^-_8	$\pi h_{9/2}\nu g_{7/2}$	3078	3120	63.84
6^-_8	$\pi h_{9/2}\nu g_{7/2}$	3188	3140	66.62
4^-_9	$\pi h_{9/2}\nu d_{3/2}$	3236	3182	72.33
5^-_9	$\pi f_{5/2}\nu g_{9/2}$	3169	3236	66.52
5^-_{10}	$\pi h_{9/2}\nu d_{3/2}$	3254	3244	79.62
4^-_{10}	$\pi f_{5/2}\nu g_{9/2}$	3243	3326	60.27
6^-_9	$\pi f_{5/2}\nu g_{9/2}$	3335	3394	66.52
3^-_{10}	$\pi f_{7/2}\nu s_{1/2}$	3408	3444	65.29
4^+_5	$\pi i_{13/2}\nu d_{5/2}$	3648	3662	97.10

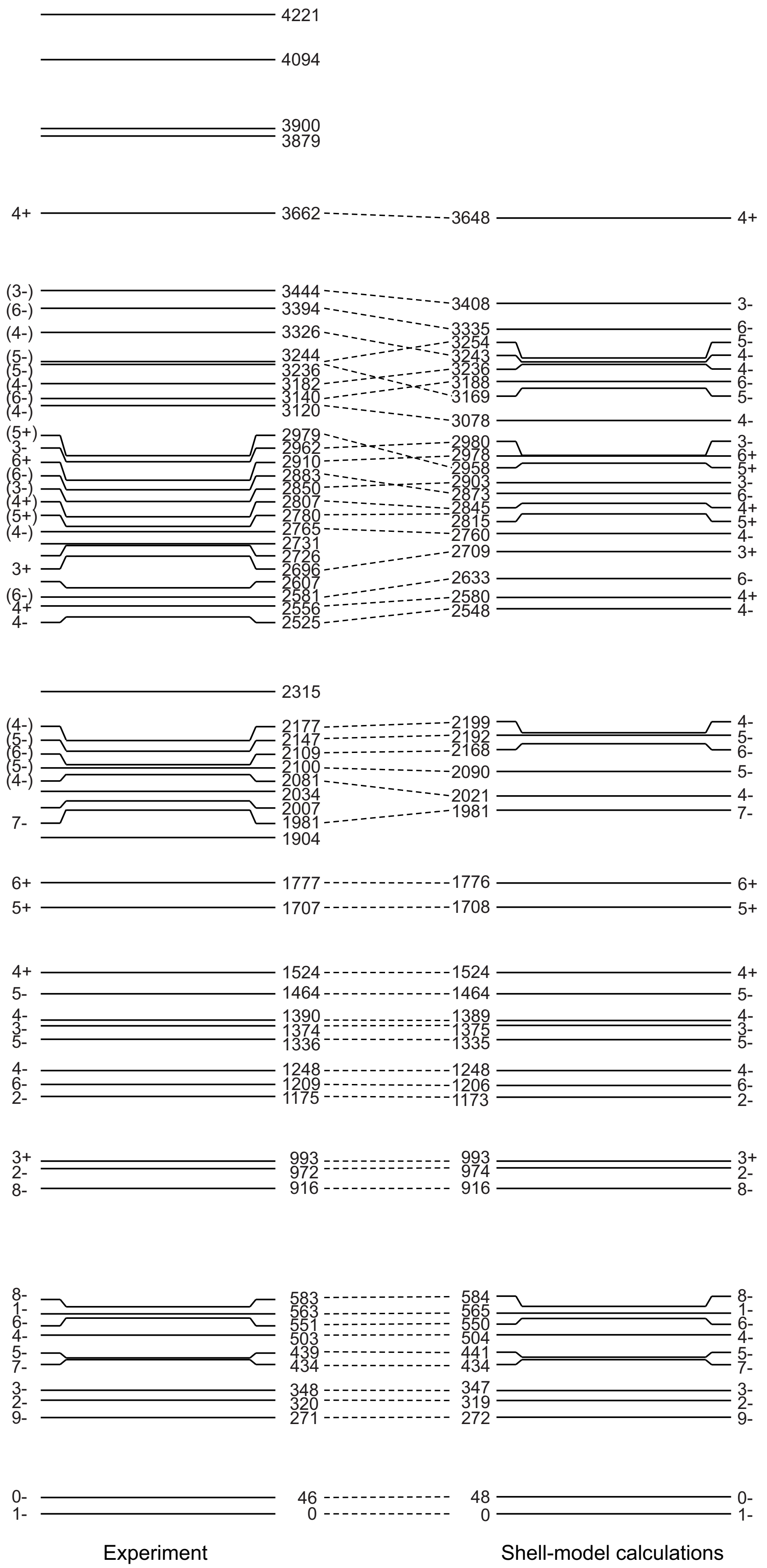

Figure 5.1. Comparison between theory and experimental results.

5.5 Discussion

As was previously mentioned, the doubly-magic ^{208}Pb nucleus is known to be one of the best closed-shell cores in nature, due to the large energy gaps separating both proton and neutron shells at Z=82 and N=126. This implies that in nuclides lying close to ^{208}Pb, excitations arising from configurations involving valence particle or hole couplings are usually described well by the shell model. However, to fully describe the structures of nuclei in the vicinity of ^{208}Pb, one has to take into account also excitations involving the promotion of protons or neutrons through the energy gaps. Therefore, in the region of ^{208}Pb, the configuration space must involve 6 proton orbitals and 7 neutron orbitals for particles above the core and 5 proton orbitals and 6 neutron orbitals for holes below the core, i.e., between the magic numbers 50 and 126 for protons and 82 and 184 for neutrons. The Bi nuclei that are the objects of interest of the presented studies are from this category: they all have 1 valence proton-particle and three (^{206}Bi) or four (^{205}Bi) neutron holes or 1 neutron particle (^{210}Bi).

The new states identified in the ^{206}Bi nucleus involve both valence and core couplings. The states in the 4-7 MeV energy range arise from valence proton-particle and three neutron-hole excitations. In spite of a relatively high number of valence holes/particles and the complexity of the wave functions ofthe states, those excitations are described very well by the shell-model calculations with the modified Kuo-Herling interaction. This demonstrates the high predictive power of the shell model in nuclei around the ^{208}Pb core. The highest valence excitation – the 23^+ state computed at 7118 keV – has been associated with the 7202-keV experimental level. It is quite obvious that the yrast excitations located in ^{206}Bi above this level must arise from excitations of the ^{208}Pb core. The highest levels established in the present studies are two isomers at 9233 (with the half-life $T_{1/2}$=155 ns) and 10170 keV ($T_{1/2}$>2µs) with probable spin-parity 28^- and 31^+. The second of these belongs to a very restricted group of states with lifetimes of one microsecond or longer that have such a high spin. To describe such excitations, one has to perform the appropriate shell-model calculations, but presently these are difficult because of the limitations caused by the large model space. The states whose couplings give rise to those high-lying isomers involve one-proton-particle and three-neutron-holes configurations as well as neutron or proton particle-hole excitations, so they are too complex to enable an estimate of excitation energies from first principles.

In case of the ^{205}Bi nucleus, only the states arising from valence proton particle and neutron holes excitations could be observed. According to the theoretical calculations, they should be present up to ~10 MeV, but experimentally it was possible to trace the level scheme up only to a 7975-keV excitation energy. While in the lower parts of the scheme, mainly yrast states are populated, at higher excitation energy one can observe an increasing density of levels - this is related to the increasing number of non-yrast states participating in the decay. For example, for excitations with $J^\pi = 41/2^+$ the non-yrast 5th, 6th, 7th, 8th, 9th, and 10th states have been located. Also the 1st, 5th, 6th, 7th, and 8th states of $43/2^+$ character have been observed. The highest excitation identified in the present work in ^{205}Bi is the 7975-keV isomeric level with an half-life estimated as $T_{1/2}$>2μs. This state arises also from the valence particles excitation and may be interpreted as an yrast level with spin-parity $51/2^-$ resulting from the $\pi i_{13/2} \nu f_{5/2}^{-1} i_{13/2}^{-3}$ configuration. It is deexcited by a 385-keV transition which may be of $M2$ character.

The yrast structure of the ^{210}Bi nucleus delineated in the present work includes both valence particles- and core excitations. The shell-model calculations describe the lower-lying part of the level scheme with great accuracy. The states located in this region, i.e., up to 2.7 MeV, result from couplings of the proton-particle being in the orbitals $h_{9/2}$, $f_{7/2}$, $i_{13/2}$, $f_{5/2}$, $p_{3/2}$, and $p_{1/2}$ with the neutron-particle residing in the $g_{9/2}$, $i_{11/2}$, $j_{15/2}$, $d_{5/2}$, $s_{1/2}$, $g_{7/2}$, and $d_{3/2}$ single-particle states. The highest spin which is available from those couplings is 14^- – it has been associated with a level located at 2725 keV. It is obvious that the higher-lying yrast or near-yrast states must come from excitations involving the ^{208}Pb core. For example, a level at 3294 keV with assigned spin-parity of 13^+, probably involves a $p_{1/2}$ neutron excited through the energy gap to the $g_{9/2}$ orbital, thus creating a neutron hole in the $p_{1/2}$ state. The maximally-aligned spin coupling of the three valence particles and one hole, the $\pi h_{9/2} \nu g_{9/2}^2 p_{1/2}^{-1}$ configuration, results indeed in J^π=13^+. For the other states identified at higher excitation energy in ^{210}Bi such simple reasoning does not work and it is not possible to determine their dominant configurations only by considering couplings between low-lying states in ^{210}Bi and core excitations in ^{208}Pb. There are two isomers among higher lying states in ^{210}Bi: one is the 16-ns isomer decaying by 175-keV $E2$ and 744-keV $E1$ γ rays, known from previous studies, and a second long-lived state which is present somewhere in the higher part of the level scheme. The investigation of delayed γ rays from the decay of this higher-lying isomer allowed to estimate its excitation energy to be ~10 MeV, but it was not possible to build the complete decay scheme, probably because many low-energy transitions are highly converted, thus escaping identification. The half life of the high-lying isomer was estimated to be of 10÷100 ns. Its spin is unknown, but one can suspect that it can be as high as 30 $\hbar$. This estimate is based on the fact that a state with the highest spin value of J^π=20^- was identified in ^{210}Bi at 5748 keV and that at an excitation energy higher by ~4 MeV one may expect to gain of about 10 units of spin.

In the three Bi isotopes investigated here, high-spin isomers are present. They are typical spin isomers arising mostly from the energy lowering of a high-spin state with respect to the yrast neighboring states (i.e., with spins $J-1$ and $J-2$).

The complementary investigation of the low-lying, low-spin structure of ^{210}Bi via the neutron capture technique yielded new results on the level scheme resulting from the decay of the neutron-capture state(s) at 4.6 MeV. From comparisons with shell-model calculations one can notice the following features. The members of the multiplet arising from the $\pi h_{9/2} \nu g_{9/2}$ configuration, i.e., 10 states with spins 0-9, were observed. Moving up with the excitation energy, the states involving the neutron in the $i_{11/2}$ state or the proton in the $f_{7/2}$ orbital (e.g., the $\pi h_{9/2} \nu i_{11/2}$ and $\pi f_{7/2} \nu g_{9/2}$ configurations) are present. The states with positive parity are observed in the higher-lying parts of the decay scheme as well. Comparisons with theoretical calculations with the Kuo-Herling interaction indicate that the observed states involve the promotion of a proton and neutron to almost all the orbitals from the used model space above the ^{208}Pb core. There are several states which do not have their theoretical counterparts in the calculations. One can suppose that they arise from the ^{208}Pb core excitations, but to describe them, the calculations ivolving such excitations must be performed. The neutron capture of a very cold neutron (5 meV) by ^{209}Bi probably populates two resonances with spin-parity values allowed in this reaction; i.e., 4^- and 5^-. Although in this energy range the level spacing should be larger than the widths of particular resonances, the scenario with two resonant states lying very close to each other and giving rise to the neutron-capture state in ^{210}Bi apparently seems to be realized.

The measured energies of the states resulting from valence particles/holes excitations in ^{205,206,210}Bi isotopes are reproduced by the shell-model calculations with satisfactory agreement. The average energy difference between computed and experimental values is 105 keV for ^{205}Bi, 67 keV for ^{206}Bi, and 29 keV for ^{210}Bi. This agreement, especially for ^{210}Bi, provides additional confidence in the tentative spin-parity assignments.

From a broader perspective, the newly identified excitations in ^{205,206,210}Bi nuclei form an excellent testing ground for realistic shell-model interactions involving nucleons occupying different major shells. This is because yrast excitations very often arise from the maximum spin coupling of the valence particles/holes and are associated with very pure configurations; e.g. their wave functions involve mostly a single, well defined configuration. On the other hand, the decay from the neutron-capture state populates a very large number of levels. They all may serve as a test of various realistic interactions which have recently been developed. In particular, one will be able to check the quality of calculations with the use of the so-called low momentum nucleon-nucleon potential V_{low-k}. This interaction has been derived from a free nucleon-nucleon potential without any additional parameters and, in principle, should be applicable to shell model nuclei such as the Bi nuclei investigated here.

Summary

In the present work, the structures of the ^{205,206,210}Bi isotopes, lying close to the doubly-magic ^{208}Pb core, were investigated. High-spin states in ^{205,206,210}Bi were populated in deep-inelastic collisions induced by ^{76}Ge and ^{208}Pb beams on a thick ^{208}Pb target. These heavy-ion reactions lead to the population of the yrast and near yrast excitations. An extensive γ-ray coincidence measurement was carried out with the Gammasphere multi-detector array. Also, an investigation of the structure of ^{210}Bi was performed with a cold-neutron capture reaction on a ^{209}Bi target (^{209}Bi(n,γ)^{210}Bi). This type of reaction permits the study of states with low spins. Slow (and cold) neutron capture results in the population of low-spin states up to a few MeV while, in deep-inelastic reactions (DIC), mostly yrast states in a broad excitation energy region are excited and can be studied up to excitation energies of the order of 10 MeV. Thus, neutron capture and DIC yield complementary sets of data which enable a more comprehensive study of nuclear structure.

The analysis of the spectra of delayed γ rays obtained by requiring coincidences with the known ^{205}Bi yrast transitions resulted in finding in this nucleus a series of higher-lying γ rays deexciting a previously unknown isomer. Inspection of the double gates set on these newly discovered transitions allowed to extend the ^{205}Bi level scheme up to an isomeric level located at approximately 8 MeV. Spin and parity assignments for the new states have been proposed, based on their decay pattern, and on comparisons with shell-model calculations, with additional help from the extracted conversion coefficients. The newly identified yrast excitations are described in terms of $1p$-$4h$ couplings. The new isomeric level at 7975 keV probably corresponds to an excitation arising from the coupling to J^{π}=51/2^{-} of valence particle and holes in the configuration $\pi i_{13/2}\nu f_{5/2}^{-1} i_{13/2}^{-3}$.

Similarly, yrast and near-yrast levels in ^{206}Bi have been established extending up to about 10 MeV. Two new isomeric states were located: one at about 9 MeV and the second, long-lived, lying at an excitation energy of ∼10 MeV. An interpretation of the ^{206}Bi level structure above the 10^{-} isomer has been presented. For the levels arising from couplings of the valence proton particle and three neutron holes, the ^{206}Bi nucleus also offers the potential of instructive comparisons with shell-model calculations. Spin-parity assignments to the newly identified states up to J^{π}=23^{+} have been presented, based on their decay pattern and comparisons with theory. For the levels resulting from core excitations, angular distributions of γ rays together with extracted conversion coefficients provided information about transition multipolarities as well as firm, relative spin and parity assignments.

The yrast structure of the ^{210}Bi nucleus was traced up to the 5996-keV excitation. The presence of an high-lying isomer was deduced from delayed γ-ray investigations. The half-life of this isomer was estimated to be in the range of 10÷100 ns, and its energy determined to be about 10 MeV. Unfortunately, it was not possible to build the complete level scheme for the decay of this isomer. The conversion coefficients and angular distributrions of γ rays were used to confirm and assign the spins and parity to the previously known and newly found levels. The structure arising from the excitations of valence protons and neutrons was compared to the shell-model calculations. The states above the 2725-keV level must be interpreted as arising from ^{208}Pb core excitations and, therefore, may be used for comparisons with future shell-model calculations using a large model space.

During the present work, the method of determining the multipolarities of the transitions using angular distributions of γ rays was elaborated. It was shown that the spins of deep-inelastic reactions products exhibit sufficient alignment to perform such an analysis. Additionally, the triple γ-coincidences were used to clean the spectra and obtain more precisely the angular distribution functions for the investigated transitions.

The low-spin excitations in ^{210}Bi were studied with use of the ^{209}Bi(n,γ)^{210}Bi reaction. The decay scheme was established and the experimental results were compared to the shell-model calculations. The energy of the state produced in the capture was estimated as 4605.2(1) keV. The decay pattern and the results of angular correlations obtained for the strong γ rays indicated that the binding-energy state is not a single level but rather a state consisting of two resonances with J^{π} values of 4^{-} and 5^{-}.

The present comparisons with theoretical calculations provided guidance for spin-parity assignments and for the interpretation of the states resulting from valence particles an holes excitations in the Bi isotopes studied. The experimental results obtained in the present study may serve as an excellent testing ground for future shell-model calculations using realistic interactions that are currently under development. Future theoretical works involving the excitations of the ^{208}Pb core may be compared to the established experimental structures of ^{205,206,210}Bi isotopes, but will require computational tools beyond those available presently.

This work is supported by the National Science Centre under Contract No. DEC-2011/01/N/ST2/04612

Acknowledgments

I would like to express my very great appreciation to Prof. Bogdan Fornal, my supervisor, for many fruitful discussions and enthusiastic encouragement during this research work. It is thanks to his patient guidance and many constructive suggestions that this work could be completed.

I wish to offer my grateful thanks to Prof. Robert Janssens, for his valuable advice and support, which have been a great help during the work on this project.

I am particularly grateful for the assistance and help in performing the shell-model calculations provided by Dr. Bartłomiej Szpak and Dr. Hugo Maier.

Special thanks should be given to Prof. Silvia Leoni for the valuable and constructive consultations concerning the $^{209}Bi(n,\gamma)^{210}Bi$ *experiment and interpretation of the results. Many thanks to Giovanni Bocchi and Patrizia Merlotti for the helpful discussions during neutron-capture data analysis.*

I would like to thank Prof. Agnieszka Kulińska who offered the help to produce the Bi target used in the neutron-capture experiment and Antoni Szperłak for the technical assistance during this task.

My special thanks are extended to the staff and PhD students of the Department of the Structure of Atomic Nucleus (NZ22) for creating a friendly atmosphere during my PhD studies.

Chcę również z całego serca podziękować Rodzicom, z ich strony zawsze mogłam liczyć na zrozumienie i wsparcie podczas nauki oraz pisania pracy. Szczególne podziękowania kieruję w stronę mojego narzeczonego Grzegorza za żywe zainteresowanie moją pracą, szczerą radość z sukcesów i cierpliwość na co dzień oraz za to, że zawsze w trudnych momentach umiał przekonać mnie, że warto iść dalej.

APPENDIX A

Level scheme of ^{210}Bi produced in neutron capture reaction

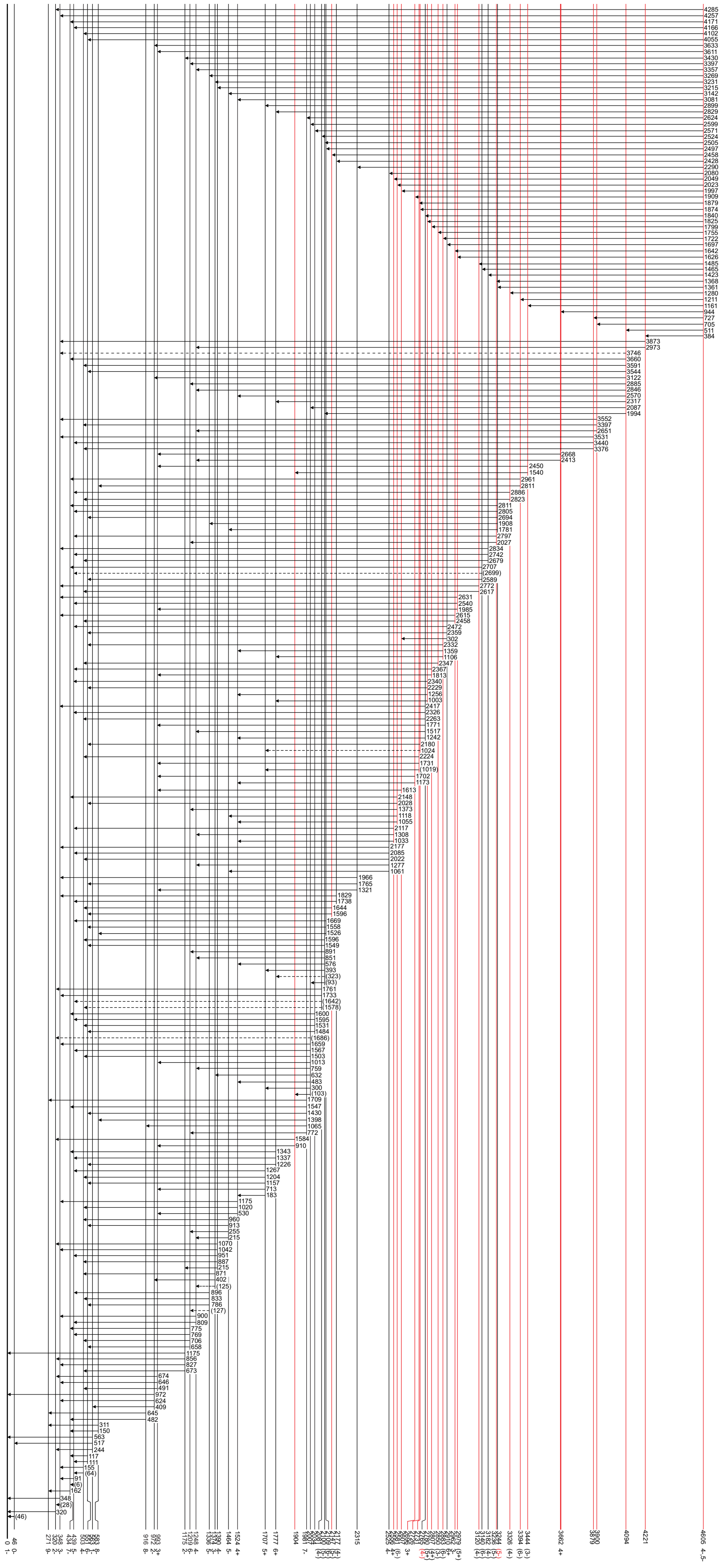

Figure A.1. Level scheme of ^{210}Bi, produced in the neutron capture reaction, established in the present work. The newly found levels are marked in red.

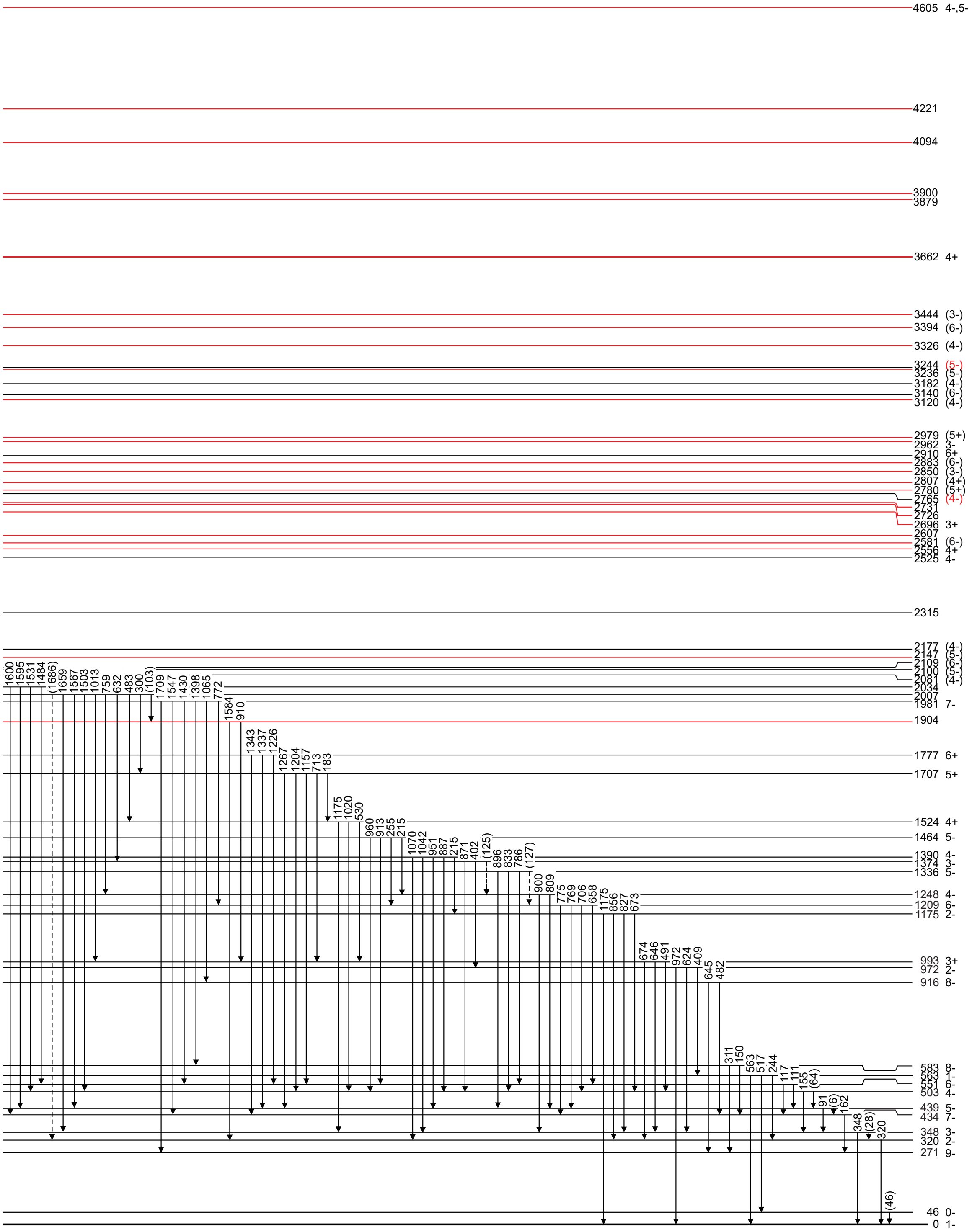

Figure A.2. Partial level scheme of ^{210}Bi, produced in the neutron capture reaction, established in the present work. The newly found levels are marked in red.

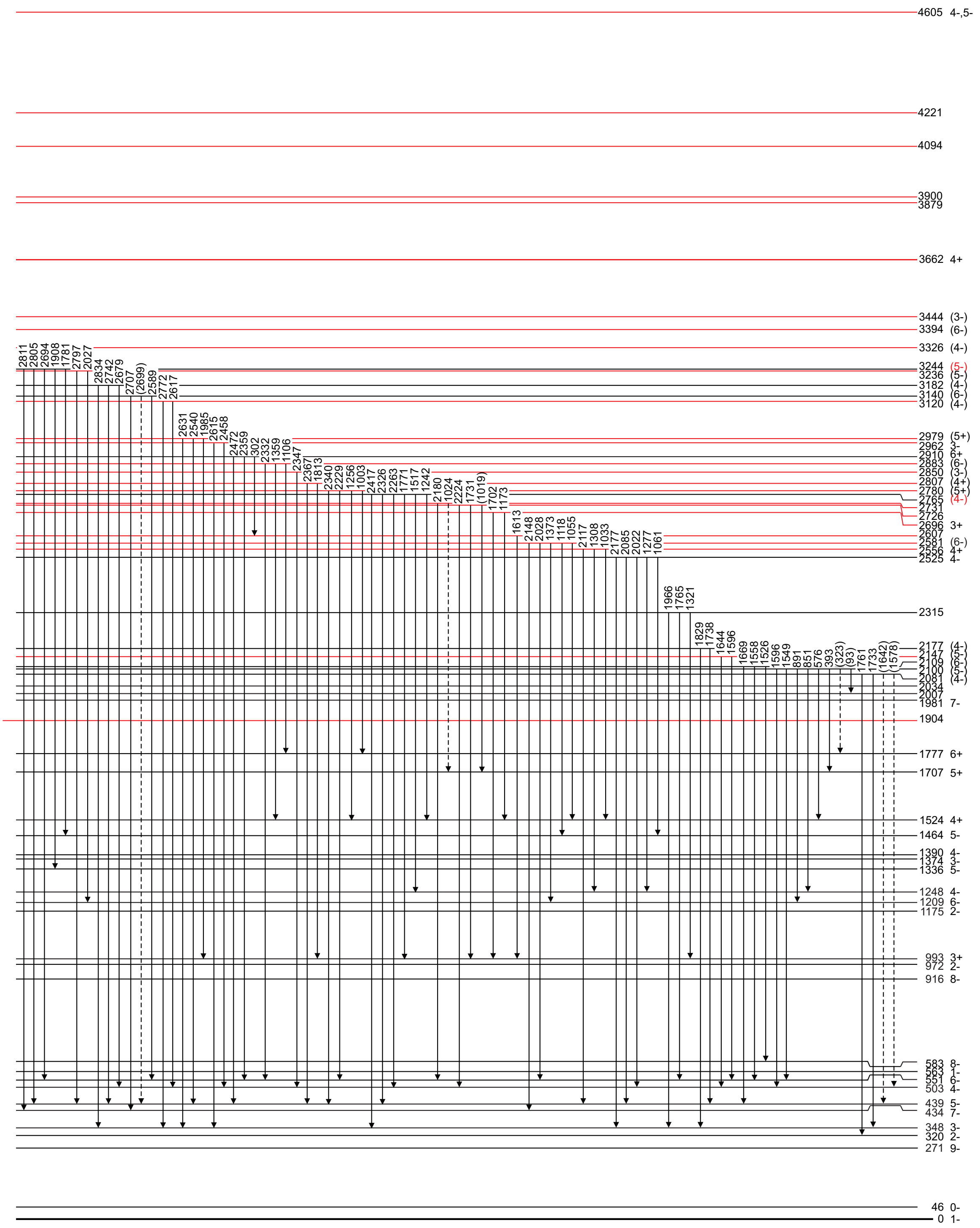

Figure A.3. Partial level scheme of ^{210}Bi, produced in the neutron capture reaction, established in the present work. The newly found levels are marked in red.

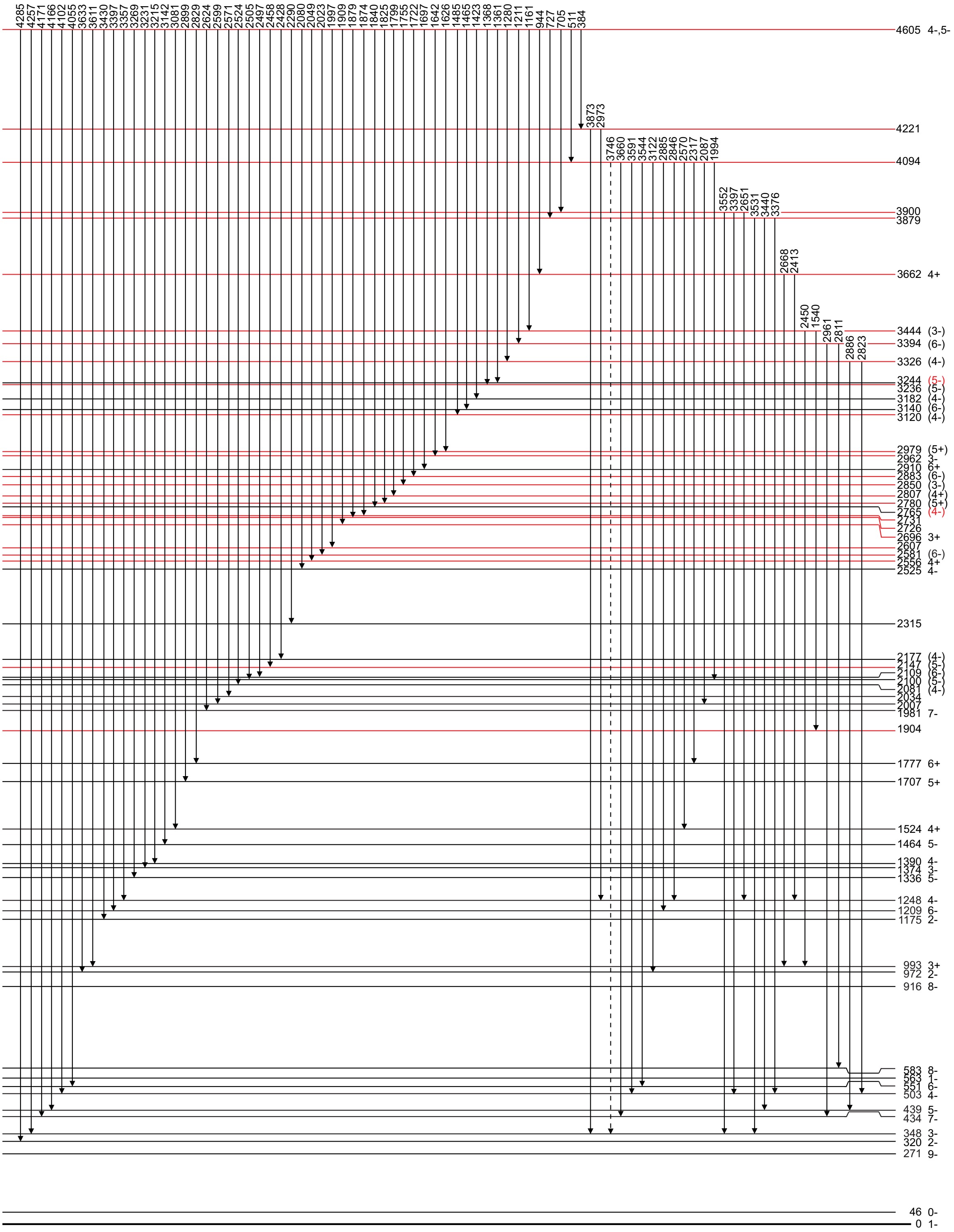

Figure A.4. Partial level scheme of ^{210}Bi, produced in the neutron capture reaction, established in the present work. The newly found levels are marked in red.

List of Figures

List of Tables

Bibliography

[1] N. Ishii, S. Aoki, T. Hatsuda, Phys. Rev. Lett. **99**, 022001 (2007).

[2] T. Hamada, I. Johnston, Nucl. Phys. **34**, 382 (1962).

[3] M. Lacombe, B. Loiseau, J. M. Richard, R. Vinh Mau, J. Côté, P. Pirès, R. de Tourreil, Phys. Rev. C **21**, 861 (1980).

[4] R. Machleidt, Adv. Nucl. Phys. **19**, 1189 (1989).

[5] R. B. Wirginia, V. G. J. Stoks, R. Schiavilla, Phys. Rev. C **51**, 51 (1995).

[6] S. R. Beane, P. F. Bedaque, K. Orginos, M. J. Savage, Phys. Rev. Lett. **97**, 012001 (2006).

[7] S. Aoki, Eur. Phys. J. A **49**, 81(2013).

[8] R. D. Woods, D. S. Saxon, Phys. Rev. **95**, 577 (1954).

[9] J. Suhonen, "From Nucleons to Nucleus", Springer (2007).

[10] M. Göppert-Mayer, Phys. Rev. **75**, 1969 (1949).

[11] O. Haxel, J. Jensen, H. Suess, Phys. Rev. **75**, 1766 (1949).

[12] E. Caurier, G. Martínez-Pinedo, F. Nowacki, A. Poves, A. P. Zuker, Rev. Mod. Phys. **77**, 427 (2005).

[13] M. Hjorth-Jensen, T. T. S. Kuo, E. Osnes, Physics Reports **261**, 125 (1995).

[14] D. J. Dean, T. Engeland, M. Hjorth-Jensen, M. P. Kartamyshev, E. Osnes, Progress in Particle and Nuclear Physics **53**, 419 (2004).

[15] B. H. Wildenthal, Prog. Part. Nucl. Phys. **11**, 5 (1984).

[16] K. H. Maier, T. Kibédi, G. D. Dracoulis, P. Boutachkov, A. Aprahamian, A. P. Byrne, P. M. Davidson, G. J. Lane, M. Marie-Jeanne, P. Nieminen, H. Watanabe, Phys. Rev. C **76**, 064304 (2007).

[17] G. E. Brown, T. T. S. Kuo, Nucl.Phys **92**, 481 (1967).

[18] K. A. Brueckner, Phys. Rev. **97**, 1353 (1995).

[19] S. K. Bogner, R. J. Furnstahl, A. Schwenk, Prog. Part. Nucl. Phys. **65**, 94 (2010).

[20] T. T. S. Kuo and G. Herling, U.S. Naval Research Laboratory Report No. 2258, 1971 (unpublished); G. Herling and T. T. S. Kuo, Nucl. Phys. A **181**, 113 (1972).

[21] B. A. Brown, Phys. Rev. Lett. **85**, 5300 (2000).

[22] B. A. Brown, A. Etchegoyen, N. S. Godwin, W. D. M. Rae, W. A. Richter, W. E. Ormand, E. K. Warburton, J. S. Winfield, L. Zhao and C. H. Zimmerman, MSU-NSCL report number 1289 (unpublished).

[23] M. Rejmund, M. Schramm, K. H. Maier, Phys. Rev. C **59**, 2520 (1999).

[24] J. B. McGrory, T. T. S. Kuo, Nucl. Phys. A **247**, 283 (1975).

[25] L. Rydström, J. Blomqvist, R.J. Liotta, C. Pomar, Nucl. Phys. A **512**, 217 (1990).

[26] E. K. Warburton, B. A. Brown, Phys. Rev. C **43**, 602 (1991).

[27] A. Hosaka, K.-I. Kubo, H. Toki, Nucl. Phys. A **444**, 76 (1985).

[28] B. Fornal, B. Szpak, R. V. F. Janssens, R. Broda, M. P. Carpenter, G. D. Dracoulis, K. H. Maier, G. J. Lane, J. Wrzesiński, S Zhu, Journal of Physics: Conference Series **267**, 012035 (2011).

[29] B. Szpak, K. H. Maier, A. S. Smółkowska, B. Fornal, R. Broda, M. P. Carpenter, N. Cieplicka, R. V. F. Janssens, W. Królas, T. Pawłat, J. Wrzesiński, S. Zhu, Phys. Rev. C **83**, 064315 (2011).

[30] B. Fornal, R. Broda, K. H. Maier, P. J. Daly, P. Bhattacharyya, Z. W. Grabowski, W. Królas, T. Pawlat, J. Wrzesiński, M. P. Carpenter, R. V. F. Janssens, F. G. Kondev, T. Lauritsen, D. Seweryniak, I. Wiedenhöver, S. Lunardi, C. A. Ur, G. Viesti, M. Cinausero, N. Marginean, M. Rejmund, Phys. Rev. C **67**, 034318 (2003).

[31] H. Grawe, Lect. Notes Phys. **651**, 33 (2004).

[32] K. Langanke, J. A. Maruhn, S E. Koonin, “Computational Nuclear Physics 1”, Springer (1991).

[33] E. Caurier, F. Nowacki, Acta Phys. Pol. B **30**, 705 (1999).

[34] W. D. M. Rae, “NuShell for Windows, Solaris and Linux”, http://knollhouse.org , unpublished (2007).

[35] W. D. M. Rae, “NuShellX for Windows and Linux”, http://www.garsington.eclipse.co.uk/, unpublished (2008).

[36] M. Alpsten, G. Astner, Phys. Scr. **5**, 41 (1972).

[37] T. Lönnroth, Z. Phys. A **307**, 175 (1982).

[38] H. Hübel, M. Guttormsen, K. P. Blume, J. Recht, A. von Grumbkow, K. Hardt, P. Schüler, Y. K. Agarwal, A. Maj, Z Phys. A **314**, 89 (1983).

[39] A. P. Byrne, U. Birkental, H. Hübel, K. P. Blume, M. Murzel, S. Heppner, K. Theine, Z. Phys. A **334**, 247 (1989).

[40] E. Arbman, Nucl. Phys. **3**, 625 (1957).

[41] T. Lönnroth, L. Végh, K. Wikström, and B. Fant, Z. Phys. A **287**, 307 (1978).

[42] J. R. Erskine, W. W. Buechner, H. A. Enge, Phys. Rev. **128**, 720 (1962).

[43] C. V. K. Baba, T. Faestermann, D. B. Fossan, D. Proetel, Phys. Rev. Lett. **29**, 496 (1972).

[44] R. K. Sheline, R. L. Ponting, A. K. Jain, J. Kvasil, B. bu Nianga, L. Nkwambiaya, Czech. J. Phys. B **39**, 22 (1989).

[45] B. Fornal, “Study of the structure of neutron-rich nuclei produced in deep-inelastic heavy ion collisions”, Habilitation thesis, Institute of Nuclear Physics PAN, Raport No. 1939/PL (2004).

[46] W. W. Daehnick, M. J. Spisak, J. R. Comfort, Phys. Rev. C **23**, 1906 (1981).

[47] C. K. Cline, W. P. Alford, H. E. Gove Nucl. Phys. A **186**, 273 (1972).

[48] J. J. Kolata, W. W. Daehnick, Phys. Rev. C **5**, 568 (1972).

[49] D. Proetel, F. Riess, E. Grosse, R. Ley, M. R. Maier, P. von Brentano, Phys. Rev. C **7**, 2137 (1973).

[50] J. S. Tsai, T. J. Kennett, W. V. Prestwich, Phys. Rev. C **27**, 2397 (1983).

[51] A. Borella, T. Belgya, S. Kopecky, F. Gunsing, M. Moxon, M. Rejmund, P. Schillebeeckx, L. Szentmiklési, Nucl. Phys. A **850**, 1 (2011).

[52] G. Audi, A. H. Wapstra, C. Thibault, Nucl. Phys. A **729**, 337 (2003).

[53] C. Domingo-Pardo *et al.* (n_TOF Collaboration), Phys. Rev. C **74**, 025807 (2006).

[54] R. Kaufmann, R. Wolfgang, Phys. Rev. **121**, 192 (1961).

[55] J. Wilczyński, Phys. Lett. B **47**, 484 (1973).

[56] W. U. Schröder and J. R. Huizenga, “Damped nuclear reactions”, Plenum Press, New York, (1984).

[57] M. N. Namboodiri, J. B. Natowitz, P. Kasiraj, R. Eggers, L. Adler, P. Gonthier, C. Cerruti, S. Simon, Phys. Rev. C **20**, 982 (1979).

[58] R. Broda, J. Phys. G **32**, R151 (2006).

[59] R. Broda, R. H. Mayer, I. G. Bearden, Ph. Benet, P. J. Daly, Z. W. Grabowski, M. P. Carpenter, R. V. F. Janssens, T. L. Khoo, T. Lauritsen, E. F. Moore, S. Lunardi, J. Blomqvist , Phys. Rev. Lett. **68**, 1671 (1992).

[60] B. Fornal, R. Broda, W. Królas, T. Pawłat, P. J. Daly, I. G. Bearden, Z. W. Grabowski, R. H. Mayer, D. Nisius, L. Richter, M. Sperrazza, M. Carpenter, R. V. F. Janssens, T. L. Khoo, T. Lauritsen, D. Bazzacco, S. Lunardi, C. Rossi-Alvarez, G. de Angelis, P. Bednarczyk, H. Grawe, K. H. Maier, R. Schubart, Acta Phys. Pol. B **26**, 357 (1995).

[61] K. S. Krane, “Introductory nuclear physics”, John Wiley & Sons Inc., New York (1988).

[62] T. Mayer-Kuckuk, “Fizyka jadrowa”, PWN, Warszawa (1983).

[63] I.-Y. Lee, Nucl. Phys. A **520**, 641c (1990).

[64] http: //nucalf.physics.fsu.edu/∼riley/gamma/

[65] G. J. Wozniak, R. J. McDonald, A. J. Pacheco, C. C. Hsu, D. J. Morrissey, L. G. Sobotka, L. G. Moretto, S. Shih, C. Schück, R. M. Diamond, H. Kluge, F.S. Stephens, Phys. Rev. Lett. **45**, 1081 (1980).

[66] G. Mouchaty, D. R. Haenni, S. Nath, U. Garg, R. P. Schmitt, Z. Phys. A **316**, 285 (1984).

[67] K. Krishan, S. K. Samaddart, J. N. Dei, J. Phys. G **14**, 1423 (1988).

[68] N. Cieplicka, K. H. Maier, B. Fornal, B. Szpak, R. V. F. Janssens, M. Alcorta, R. Broda, M. P. Carpenter, C. J. Chiara, C. R. Hoffman, B. P. Kay, F. G. Kondev, W. Królas, T. Lauritsen, C. J. Lister, E. A. McCutchan, T. Pawłat, A. M. Rogers, D. Seweryniak, N. Sharp, W. B. Walters, J. Wrzesiński, and S. Zhu , Phys. Rev. C **86**, 054322 (2012).

[69] T. Yamazaki, Nucl. Data A **3**, 1 (1967).

[70] H. Morinaga and T. Yamazaki, “In-beam gamma-ray spectroscopy”, North-Holland Publ. Co, Amsterdam (1976).

[71] F. G. Kondev, Nuclear Data Sheets **109**, 1527 (2008).

[72] J. Simpson, F. Azaiez, G. de France, J. Fouan, J. Gerl, R. Julin, W. Korten, P. J. Nolan, B. M. Nyako, G. Sletten, P. M. Walker and the EXOGAM Collaboration, Acta Phys. Hung. NS **11**, 159 (2000).

[73] http://gasp.lnl.infn.it/

[74] http://lpsc.in2p3.fr/index.php/en/activites-scientifiques/structure-nucleaire/lohengrin

[75] ILL materials.

[76] P. Merlotti, "Study of the ^{209}Bi(n,γ)^{210}Bi Reaction with Spectroscopy Techniques at High Energy Resolution", Master thesis, University of Milan (2013).

[77] A. J. Ferguson, "Angular correlation methods in gamma-ray spectroscopy", North-Holland Publ. Co, Amsterdam (1965).

[78] Giovanni Bocchi, private communication.

[79] E. der Mateosian and A. W. Sunyar, At. Data and Nucl. Data Tables **13**, 391 (1974).

[80] F. G. Kondev, Nuclear Data Sheets **101**, 521 (2004).

[81] C. J. Chiara, F. G. Kondev, Nuclear Data Sheets **111**, 141 (2010).

[82] R. Broda, K. H. Maier, B. Fornal, J. Wrzesiński, B. Szpak, M. P. Carpenter, R. V. F. Janssens, W. Królas, T. Pawłat, S. Zhu, Phys. Rev. C **84**, 014330, (2011).